UNIVERSITY OF CALIFORNIA
Santa Barbara

Search for supersymmetry in proton-proton collisions at 8 TeV in events with a single lepton, large jet multiplicity, and multiple b jets

A Dissertation submitted in partial satisfaction
of the requirements for the degree of

Doctor of Philosophy

in

Physics

by

Paul B. Geffert

Committee in Charge:

Professor David Stuart, Chair

Professor Jeffrey Richman

Professor Steven Giddings

September 2014

The Dissertation of
Paul B. Geffert is approved:

Professor Jeffrey Richman

Professor Steven Giddings

Professor David Stuart, Committee Chairperson

July 2014

Search for supersymmetry in proton-proton collisions at 8 TeV in events with a single lepton, large jet multiplicity, and multiple b jets

Copyright © 2014

by

Paul B. Geffert

Acknowledgements

I would like to express my deepest appreciation to all of those who helped make this thesis possible. My success as a graduate student is due largely to the constant source of support and advice I had in my advisor, David Stuart. His confidence in my abilities inspired me to persevere though difficult times and accomplish more than I thought possible.

The members of the UCSB experimental high energy physics group fostered a positive and productive environment which was truly a pleasure to work in. Furthermore, many of them made invaluable contributions to my thesis. Chiefly sharing the burden of the analysis work with me was Christopher West, against whom I could bounce my not always well-formed ideas. Jeffrey Richman, who acted as a second advisor to me, helped make sure our work never veered too far off track. Tom Danielson provided his much needed b-tagging expertise and heroic effort in the latter stages of the analysis. Wing To, Christopher Justus, Victor Pavlunin, and Finn Rebassoo all shared critical insights from their prior involvement on similar projects.

My first mentor, Dave Toback, also deserves credit for being a guiding hand during my undergraduate career. I am thankful for his continued encouragement and advice.

In the end, none of this would have been worthwhile without my family to share in my joy. Without the lifelong love and support of my parents, James and Susan, I would certainly not have made it this far. Their unwavering encouragement to pursue my interests gave me the courage to start this process. Finally, I would like to express gratitude to my beloved wife Sarah, who was right beside me every step of the way, selflessly crossing countries and continents, keeping me sane no matter how stressful my work.

Curriculum Vitæ

Paul B. Geffert

Education

2014	Doctor of Philosophy in Physics, University of California, Santa Barbara.
2011	Masters in Physics, University of California, Santa Barbara.
2009	Bachelor of Science in Physics and Bachelor of Science in Mathematics, Texas A&M University

Experience

2009 – 2014	Graduate Research Assistant, High Energy Experiment, University of California, Santa Barbara.
2008	Undergraduate Research Fellow, High Energy Experiment, Texas A&M University.

Selected Publications

CMS Collaboration: "Search for supersymmetry in events with b jets and missing transverse momentum at the LHC," In *J. High Energy Phys. 07 (2011) 113, arXiv:1106.3272.*

CMS Collaboration: "Search for supersymmetry in pp collisions at $\sqrt{s} = 8$ TeV in events with a single lepton, large jet multiplicity, and multiple b jets" In *Phys. Lett. B 733 (2014) 328, arXiv:1311.4937.*

Abstract

Search for supersymmetry in proton-proton collisions at 8 TeV in events with a single lepton, large jet multiplicity, and multiple b jets

Paul B. Geffert

This thesis describes a search for supersymmetry in events with a single lepton, large jet multiplicity, multiple b jets, and significant transverse momentum imbalance in 19.3 fb^{-1} of pp collisions at $\sqrt{s} = 8$ TeV recorded in 2012 by the Compact Muon Solenoid experiment at the Large Hadron Collider. This signature targets strongly produced massive gluinos which decay through top squarks. The observed yields in the signal regions, spanning a broad range of event kinematics, agree with the Standard Model background predictions, which are obtained with a heavy reliance on data control samples. The results of this search are interpreted as cross section limits in the context of simplified supersymmetric scenarios in which gluinos are pair produced and cascade decay to a four top quark, two lightest neutralino final state. By comparing these limits with gluino pair production cross sections, gluinos with mass less than 1 TeV are excluded for low lightest neutralino masses, largely independent of top squark mass.

Contents

List of Figures

List of Tables

Chapter 1

Introduction

The primary goal of physics is to explain the universe around us. To this end, the field of particle physics strives to identify and describe the fundamental particles of nature and their interactions with one another. Beginning with the discovery of atoms in the 19th century, particle physics has continued to probe smaller and smaller distance scales while discovering a plethora of particles. These findings are encapsulated in the Standard Model of particle physics, a theory describing all the known fundamental particles and forces, with the exception of gravity. First developed roughly half a century ago, it is an extremely well-tested theory.

Despite its great success, the Standard Model is not without its issues. For instance, it has no explanation of the dark matter inferred from astronomical observations or the extreme disparity in strength between gravity and the other fundamental forces, known as the Hierarchy Problem. These problems, along with

the theory of Supersymmetry (SUSY) which could provide a solution to them, are discussed in Ch. 2. Various theoretical considerations dictate that current particle physics experiments may be able to probe the existence of Supersymmetry.

To probe physics at small scales, experiments utilize extremely large particle accelerators which collide particles at high energy. The higher the energy, the shorter the distance scale that can be probed. The world's highest energy particle collider is the Large Hadron Collider (LHC) located at the European Organization for Nuclear Research (CERN) near Geneva, Switzerland. When protons collide at the LHC, much of the energy of the collision is converted into matter, resulting in the production of many particles. To effectively exploit these collisions for physics, a detector is positioned next to and surrounding the collision point to measure the particles that are produced. One such detector is the Compact Muon Solenoid (CMS), and is located along the LHC ring near the small town of Cessy, France. Together, the LHC and CMS, which are described in Ch. 3, provide data in which a broad range of SUSY models can be tested. However, before this can be done, the raw signals from the CMS detector must be reconstructed into meaningful objects for physics analysis, as described in Ch. 4.

In order to avoid excessive fine-tuning of the SM parameters, as discussed in Sec. 2.3.3, it is likely that the production of SUSY particles at the LHC would result in multiple top quarks in the final state. As described in Ch. 5, this thesis

targets that signature by searching a sample of events with a single lepton (electron or muon), multiple b quarks, and large transverse momentum imbalance ($\not\!\!E_{\mathrm{T}}$). The paper describing this analysis can be found in [1]. Similar but earlier searches are documented in [2, 3]. Other recent published SUSY searches using a single-lepton signature can be found in Refs. [4, 5, 6, 7, 8, 9].

The background estimation in this search is described in Ch. 6. The dominant background comes from events with exactly one promptly produced lepton in the final state and is estimated using the momentum spectrum of charged leptons with the procedure first described in Ref. [10]. The next-largest background comes from events with tau-leptons, which is estimated by using simulation-derived templates to emulate tau decays in various control samples. The combined results of the background estimates are shown alongside the observed yields in data in Ch. 7.

The results of this analysis are interpreted in the context of a set of simplified SUSY scenarios in Ch. 8. Based on the compatibility of the background predictions with observations, upper limits are placed on the masses of the relevant SUSY particles in these scenarios. Finally, Ch. 9 concludes the discussion.

Chapter 2

Theory

2.1 Standard Model of Particle Physics

The Standard Model (SM) of particle physics describes the fundamental particles of nature and their interactions via the strong, weak, and electromagnetic forces. It is a quantum field theory with gauge symmetry given by the group $SU(3)_C \times SU(2)_L \times U(1)_Y$. The local preservation of these gauge symmetries is what gives rise to these forces. The $SU(3)_C$ group, where C represents color charge, corresponds to the strong force, modelled by the theory of Quantum Chromodynamics (QCD) [11, 12, 13]. The $SU(2)_L \times U(1)_Y$ group, where L represents weak isospin which only couples to left-handed fermions and Y represents weak hypercharge, corresponds to the electroweak (EW) force. The EW force is described by the unification of the weak and electromagnetic (EM) forces by Glashow, Weinberg, and Salam [14, 15, 16]. Each of the fundamental forces contained in the SM,

whose interactions with the constituents of matter are briefly described in this section, plays a critical role in the measurement detailed herein. A more complete description of the standard model can be found in [17, 18]. The gravitational force, which is too weak to be relevant in fundamental particle interactions at the scales currently accessible to experiment, is not included in the SM.

The Lagrangian describing the standard model is

$$\begin{aligned}
\mathcal{L}_{\mathrm{SM}} = &-\frac{1}{4}\boldsymbol{G_{\mu\nu}}\cdot\boldsymbol{G^{\mu\nu}} - \frac{1}{4}\boldsymbol{W_{\mu\nu}}\cdot\boldsymbol{W^{\mu\nu}} - \frac{1}{4}B_{\mu\nu}B^{\mu\nu} \\
&+ \overline{L}\gamma^{\mu}\left(i\partial_{\mu} - g\frac{1}{2}\boldsymbol{\tau}\cdot\boldsymbol{W_{\mu}} - g'\frac{Y}{2}B_{\mu}\right)L \\
&+ \overline{E}\gamma^{\mu}\left(i\partial_{\mu} - g'\frac{Y}{2}B_{\mu}\right)E \\
&+ \overline{Q}\gamma^{\mu}\left(i\partial_{\mu} - g\frac{1}{2}\boldsymbol{\tau}\cdot\boldsymbol{W_{\mu}} - g'\frac{Y}{2}B_{\mu} - g_s\frac{1}{2}\boldsymbol{\lambda}\cdot\boldsymbol{G_{\mu}}\right)Q \\
&+ \overline{U}\gamma^{\mu}\left(i\partial_{\mu} - g'\frac{Y}{2}B_{\mu} - g_s\frac{1}{2}\boldsymbol{\lambda}\cdot\boldsymbol{G_{\mu}}\right)U \\
&+ \overline{D}\gamma^{\mu}\left(i\partial_{\mu} - g'\frac{Y}{2}B_{\mu} - g_s\frac{1}{2}\boldsymbol{\lambda}\cdot\boldsymbol{G_{\mu}}\right)D \\
&+ \left|\left(i\partial_{\mu} - g\frac{1}{2}\boldsymbol{\tau}\cdot\boldsymbol{W_{\mu}} - g'\frac{Y}{2}B_{\mu}\right)\phi\right|^2 - V(\phi) \\
&- \left(y_L\overline{L}\phi E - y_U\overline{Q}i\tau_2\phi^{*}U + y_D\overline{Q}\phi D + \text{hermitian conjugate}\right),
\end{aligned} \tag{2.1}$$

where the τ matrices are the generators of $SU(2)_L$ and the λ matrices are the generators of $SU(3)_C$. The gauge and matter field content of the SM is summarized in Tables 2.1 and 2.2, respectively. These tables show the representations of these fields in the $SU(3)_C$ and $SU(2)_L$ groups, as well as the weak-hypercharge quantum number in the $U(1)_Y$ group.

Table 2.1: The gauge field content of the SM. The Group column indicates which gauge group is responsible for the field. The representations of these fields in the $SU(3)_C$ and $SU(2)_L$ groups, as well as the weak-hypercharge quantum number in the $U(1)_Y$ group are also shown.

Field	Group	$(SU(3)_C, SU(2)_L, U(1)_Y)$
B boson	$U(1)_Y$	$(\mathbf{1}, \mathbf{1}, 0)$
W bosons ($\boldsymbol{W}$)	$SU(2)_L$	$(\mathbf{1}, \mathbf{3}, 0)$
Gluons ($\boldsymbol{G}$)	$SU(3)_C$	$(\mathbf{8}, \mathbf{1}, 0)$

Table 2.2: The matter field content of the SM. The representations of these fields in the $SU(3)_C$ and $SU(2)_L$ groups, as well as the weak-hypercharge quantum number in the $U(1)_Y$ group are shown. The quark and lepton fields each have three generations, of which only the first generation is shown. A subscript L (R) means the particle is left(right)-handed.

Field	Symbol	$(SU(3)_C, SU(2)_L, U(1)_Y)$
Leptons	$L = (\nu_{e,L} \quad e_L)$	$(\mathbf{1}, \mathbf{2}, -1/2)$
	$E = e_R$	$(\mathbf{1}, \mathbf{1}, -1)$
Quarks	$Q = (u_L \quad d_L)$	$(\mathbf{3}, \mathbf{2}, 1/6)$
	$U = u_R$	$(\mathbf{3}, \mathbf{1}, 2/3)$
	$D = d_R$	$(\mathbf{3}, \mathbf{1}, -1/3)$
Higgs	$\phi = (\phi^+ \quad \phi^0)$	$(\mathbf{1}, \mathbf{2}, 1/2)$

The Standard Model is one of the most thoroughly tested scientific theories, and is in agreement with nearly all experimental data. For example, a description of electroweak precision tests can be found in Ref. [19], strong interaction tests in Ref. [20], and incredible agreement between experiment and EM theory for the electron anomalous magnetic moment to seven orders of magnitude in Ref. [21]. The standard model has also successfully predicted the existence of multiple par-

ticles, such as the Z boson and top quark, before their discovery [22, 23]. More recently, the observation of a new boson with mass of roughly 125 GeV [24, 25] appears to be consistent with the predicted SM Higgs boson.

2.1.1 Fundamental Particles

The fundamental particles of the SM have no known sub-structure and comprise all of the visible matter in the universe. Figure 2.1 shows the fundamental particles of the SM separated into distinct categories. The gauge bosons are the force carrying particles. Gluons (g) mediate the strong force, photons (γ) mediate the electromagnetic force, and W and Z bosons mediate the weak force. Quarks, of which there are 6 flavors, interact via all three of these forces, and are bound together by the strong force to form hadrons. Leptons come in electromagnetically charged and neutral varieties, of which the former can interact via the electromagnetic and weak forces, while the latter, called neutrinos (ν), can only interact via the weak force.

Both leptons and quarks come in 3 generations, or equivalently families, separated into columns in Fig. 2.1. There is no theoretical reason why there should only be three generations; rather, this is dictated by experimental observations. The vast majority of visible matter in the universe contains only particles from the first generation. For example, an atom consists of an electron cloud surrounding

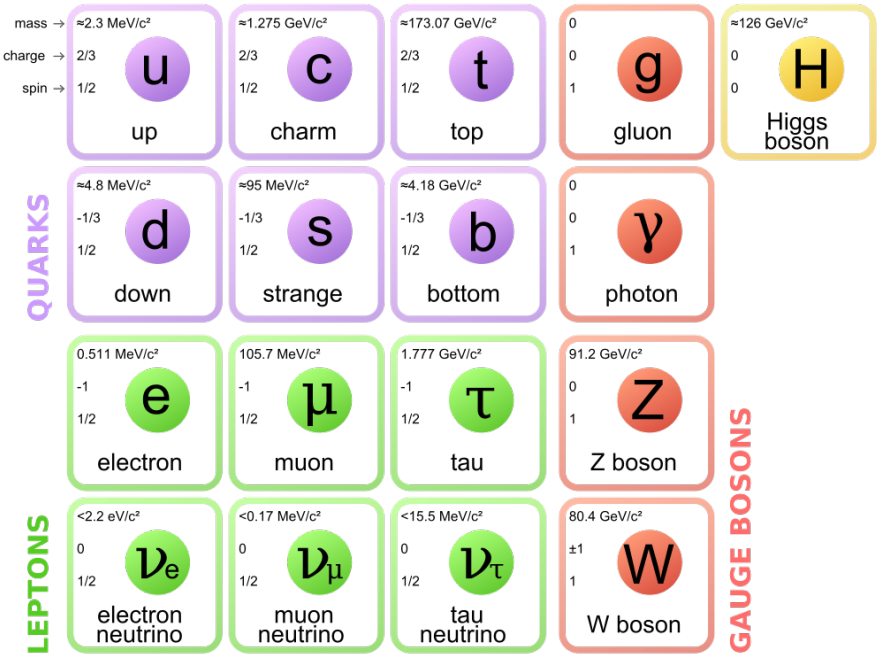

Figure 2.1: The fundamental particles described by the Standard Model, color coded by leptons, quarks, gauge bosons and the Higgs boson. The mass, charge and spin of each particle is also shown. Figure taken from Ref. [26].

a nucleus consisting of protons (p) and neutrons, which are bound states of two up quarks and a down quark and two down quarks and an up quark, respectively. The dominance of the first generation in everyday matter arises from the fact that matter containing higher generations of quarks and charged leptons tends to decay such that only lighter first generation particles remain. The higher generations only become relevant at larger energy scales, which are more than achieved in collisions at the LHC.

Finally, it is easy to see that the fundamental particles in Fig. 2.1 are the same as the fields which appear in the SM Lagrangian in Eq. 2.1, with the notable exception that Higgs, W, and B fields do not correspond exactly. This is due to electroweak symmetry breaking, which generates the mass of W and Z bosons [27, 28, 29, 30, 31, 32]. These particles would otherwise be massless in the SM. The mechanism for this involves the Higgs scalar field, ϕ, which is a complex doublet in $SU(2)_L \times U(1)_Y$ space with potential, $V(\phi)$ from Eq. 2.1, of the form

$$V(\phi) = \mu^2 \phi^\dagger \phi + \lambda (\phi^\dagger \phi)^2, \tag{2.2}$$

where $\mu^2 < 0$ and $\lambda > 0$. The set of points at which the minimum of the Higgs field is obtained is invariant under $SU(2)_L \times U(1)_Y$, but the particular minimum point chosen by nature spontaneously breaks the symmetry. This symmetry breaking mixes the W and B boson fields to obtain the $W^\pm$, Z, and γ boson particles observed in nature. Three of the four degrees of freedom of the Higgs field are

used to bestow mass to the W and Z bosons. The Higgs field is, however, invariant under $U(1)_{\mathrm{EM}}$, the gauge group corresponding to the electromagnetic force, which leaves the photon massless. The final degree of freedom from the Higgs field accounts for the massive Higgs boson. The symmetry breaking of the Higgs field is also responsible for the generation of the charged-lepton and quark masses through their Yukawa couplings to the Higgs boson, i.e., the last line of Eq. 2.1.

2.1.2 Fundamental Forces

Electromagnetic Force

The electromagnetic force is mediated by photons and only affects particles with electric charge. It is described by the group $U(1)_{\mathrm{EM}}$, which has charge defined in terms of the $SU(2)_L$ and $U(1)_Y$ EW quantum numbers. The EM charge is given by $Q = T^3 + Y$, where T^3 is the third component of weak-isospin and Y is the weak hypercharge. The relativistic field theory that explains EM is known as Quantum Electrodynamics (QED). Particles with oppositely signed charge attract and particles with charge of the same sign repel one another. Because the photon is massless and not self-interacting, this force has infinite range and potential roughly proportional to $1/r$, where r is the distance between the two particles.

The reason the potential is not identically proportional to $1/r$ is that there are quantum mechanical corrections which depend on r. These corrections arise

because the vacuum can give rise to an electron-positron pair for a brief time limited by the uncertainty principle. For the case of an electron, the nearby temporary electron-positron pairs align such that the positrons are closer to the electron. This effect causes the charge of the original electron to be screened. However, as one approaches the original electron, the effect of this charge screening is reduced and the apparent charge of the electron, and thereby relative strength of the electromagnetic force, increases. This effect is equivalently described as a running of the electromagnetic coupling constant, α.

Strong Force

The strong force is mediated by gluons and only couples to quarks and gluons. Like the photon, the gluon is also massless. The strong force is based on the quantity of color charge, and is described by the theory of Quantum Chromodynamics. There are 3 fundamental color charges (red, green, blue) and their corresponding anti-color charges (anti-red, anti-green, anti-blue). Each quark has a color and each anti-quark has an anti-color charge. The exchange of a gluon changes the color state of each participating quark or anti-quark. One widely believed but not rigorously proven consequence of QCD is confinement, which states that particles must be color neutral, meaning lone quarks cannot be observed. This effect results in the following color-neutral bound states of quarks, generally

called hadrons: (a) baryons, which have 3 quarks with color red, green, and blue and (b) mesons, which have a quark and anti-quark, not necessarily of the same flavor, with a color and its anti-color.

The group formed under these color charges is $SU(3)_C$, whose fundamental representation is the set of 3×3 unitary matrices with determinant 1. $SU(3)_C$ has 8 independent generators, resulting in 8 different gluons. Since gluons carry color, they can interact with themselves and the gauge group is non-Abelian, which is a key difference with electromagnetism. More generally, gauge bosons will be self-interacting if and only if the corresponding gauge group is non-Abelian.

As in QED, the strong coupling constant, α_s, runs with distance, or equivalently energy, but in the opposite direction. If gluons did not self-interact, the strong coupling constant would instead increase with increasing energy. At extremely small distance scales, much less than the size of a proton, α_s is small enough such that quarks behave as essentially free particles. This effect is known as asymptotic freedom, and thankfully allows for perturbative QCD calculations at high energy.

On the other hand, as the distance between quarks increases, the increased potential between them eventually makes it more energetically favorable to pull a $q\bar{q}$ pair from the vacuum to shield the color charge of the original quarks and thereby reduce the strong force potential energy. This is called hadronization

and is an extremely important process in high energy particle collisions at the LHC, in which bare quarks would otherwise be frequently produced. The result of this hadronization for a high momentum quark or gluon is a collimated spray of particles, known as a jet.

Weak Force

The weak force is mediated by the massive W and Z vector bosons and couples to all particles except for gluons. The massive force carriers limit the weak interaction to short distance scales via the uncertainty principle. However, for distances below around 10^{-18} m, corresponding to energies above the W and Z boson masses, the weak force is comparable in strength to the EM force. If we define the weak mixing angle, θ_W, as $\tan(\theta_W) = \frac{g'}{g}$, with g and g' from Eq. 2.1, then the ratio of EM to W boson coupling constants is $\sin(\theta_W)$ and the ratio of EM to Z boson coupling constants is $\cos(\theta_W)\sin(\theta_W)$. The measured value of $\sin^2(\theta_W)$ is 0.23150 ± 0.00016 [19], meaning the weak and EM coupling strengths are all the same order of magnitude.

As with EM, the weak force does not couple different lepton generations together. However, unlike QED or QCD, W bosons couple different quark generations. For example, a charm quark, which is 2nd generation, can change into a down quark, which is 1st generation, with the aid of a W. The mixing of the

quark flavor eigenstates by the weak force is described by the Cabibbo-Kobayashi-Maskawa (CKM) matrix.

Another feature that is unique to the weak force is that interactions depend on the chirality of the interacting fermions. W bosons only couple to left-handed fermions and right-handed anti-fermions. This arises from the vector minus axial vector (V-A) nature of the W interactions. Fermion interactions with Z bosons are only partially V-A, meaning that right-handed fermions, except for neutrinos, can participate but couple with different strength than left-handed fermions.

2.2 Motivation for Physics Beyond the Standard Model

Despite the fact that the Standard Model agrees extremely well with virtually all current experimental data, there are a few reasons why it may not be a complete description of all particle physics. This section explains some of the motivations for physics beyond the standard model. Section 2.3 describes the class of extensions of the standard model with the potential to address these issues, which are targeted by this search.

2.2.1 Unification of the Forces

Given the successful unification of the electromagnetic and weak forces in the SM, it seems natural that all three of the electromagnetic, weak, and strong forces should similarly be unified. If such unification is correct, one of the implications would be that the coupling constants of the 3 different forces become identical at some high energy, m_{GUT}. Here GUT stands for grand unified theory. Above m_{GUT}, the 3 forces would share the same coupling constant, and below m_{GUT}, due to some form of symmetry breaking, the forces would have distinct coupling constants. However, in the SM the gauge couplings of the forces do not come close to unifying at any energy. This result can be seen in Fig. 2.2, which shows the running of the inverse coupling constants versus energy. From this figure, it is clear that the couplings, and hence the 3 forces, cannot be unified within the framework of the SM. If unification is to occur, there must be additional physics beyond the standard model.

2.2.2 Dark Matter

Dark matter is the name given to mass inferred from astronomical observations that does not interact electromagnetically. The first evidence for dark matter came from the excess of mass in the Coma cluster, as determined from application of the virial theorem, compared to its luminosity [34]. This observation was not given

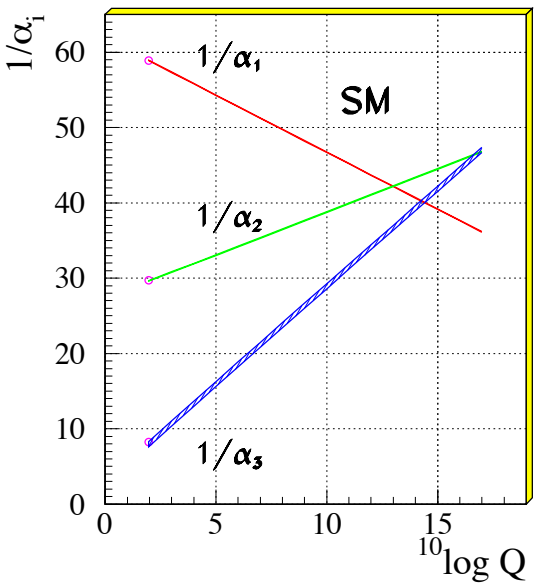

Figure 2.2: The running of the inverse SM coupling constants versus energy, with GeV units. α_1 corresponds to the electromagnetic force, α_2 corresponds to the weak force, and α_3 corresponds to the strong force. Figure taken from Ref. [33].

significant attention, but subsequent studies have provided a plethora of support for the existence of dark matter.

The first seriously considered evidence came from the anomalous behavior of the rotation curves of galaxies. A rotation curve shows the rotational velocity of the visible matter about a galaxy's center. If there is no dark matter, the majority of the mass in a galaxy is situated close to its center, leading to decreasing rotational velocities with increasing distance away from the galactic center. Observations, starting with [35], have found that the rotational velocities do not, however, decrease with distance, but instead remain rather flat. This is illustrated in Fig 2.3, which shows the difference between a typical observed and expected rotation curve. The relative flatness of the observed rotation curve indicates that the total amount of matter in the galaxy is distributed more uniformly than just the visible matter. This discrepancy can be accounted for if there is an additional source of weakly interacting matter, i.e., dark matter.

Another method to infer the presence of dark matter is through gravitational lensing. Because large amounts of matter will bend the path of light according to the principles of general relativity, astronomers can examine the distortion of background galaxies caused by matter in the foreground. An excess of matter inferred from the gravitational lensing compared to the amount of visible matter can indicate the presence of dark matter.

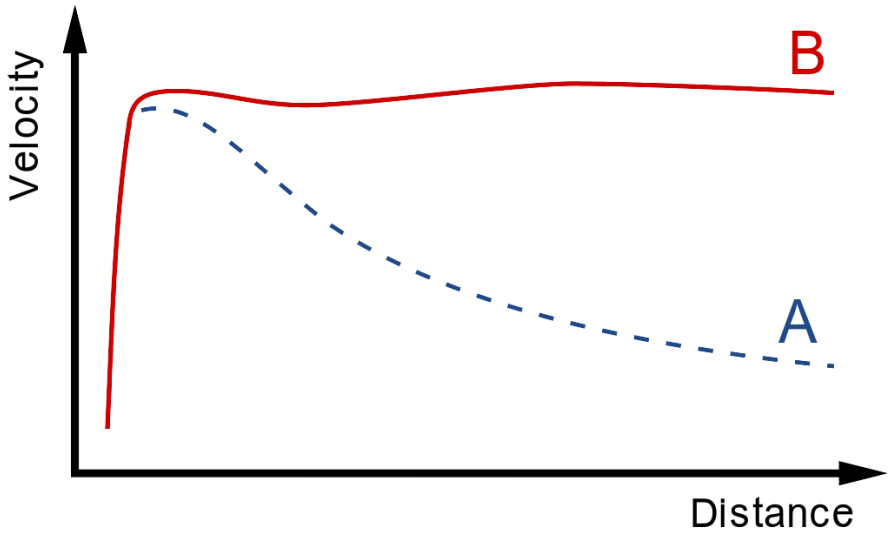

Figure 2.3: Typical rotational velocity versus distance from the center in a spiral galaxy as predicted (dashed blue line labeled A) and observed (solid red line labeled B). The drastic difference between these curves is evidence for the presence of dark matter. Figure taken from Ref. [36].

One striking piece of evidence involving gravitational lensing comes in the form of the Bullet Cluster. The Bullet Cluster consists of two galaxy clusters which collided in a direction transverse to the Earth's line of sight. The baryonic gas of each cluster, which comprises the majority of the visible mass, was significantly slowed due to electromagnetic interactions. Because dark matter interacts too weakly to be slowed significantly during the collision, the dark matter in each cluster would have passed through the other cluster, resulting in a large amount of mass away from the baryonic center of the collision. Such a shift of the mass in the Bullet Cluster is illustrated in Fig. 2.4. In this figure, the baryonic matter

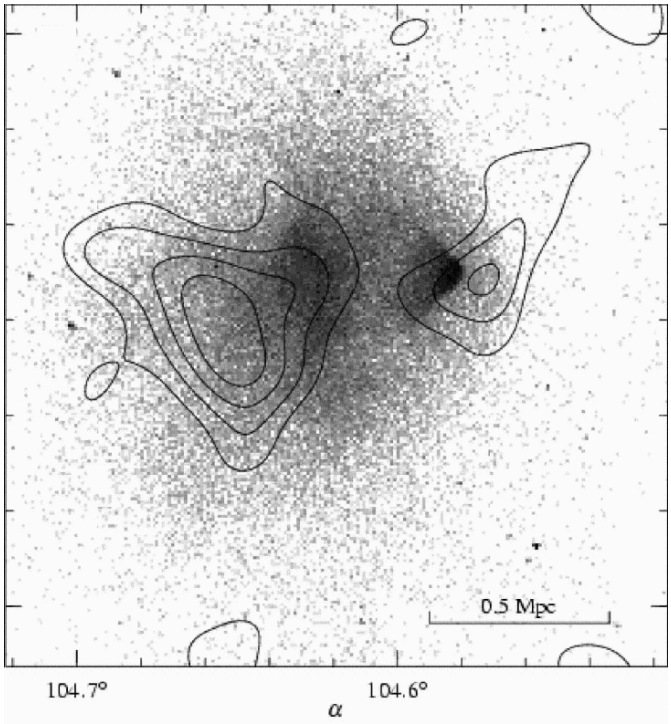

Figure 2.4: Image of the Bullet Cluster showing the baryonic matter distribution in gray-scale and the mass contours from gravitational lensing as black contours. The shift of the centers of mass away form the visible matter is evidence for the existence of dark matter. Figure taken from Ref. [37].

distribution is shown in gray-scale, while the mass contours from gravitational lensing are shown as black contours. The shift of the centers of mass away form the visible matter is direct evidence for the existence of dark matter.

Anisotropies in the cosmic microwave background (CMB), the radiation present at the time of recombination in the early universe, can be used not only as further evidence for dark matter, but also as a measurement of its energy density in the universe. These anisotropies arise from acoustic oscillations of baryons and pho-

tons in the early universe. The presence of dark matter would have a significant impact on these oscillations and hence alter the multipole power spectrum of the CMB. This was measured most recently and precisely by the Planck satellite [38], which found the ratio of dark matter and baryonic matter densities to be 5.4 ± 0.2.

If the dark matter is a particle, then it must be stable and weakly interacting. The only SM particles that satisfy this are the neutrinos. Neutrinos, however, are not good candidates for dark matter for a couple of reasons. If neutrinos were the dark matter, their relativistic velocities would result in galaxy formation in the early universe that disagrees significantly with observations. Additionally, the density of neutrinos is too small to account for the amount of dark matter in the universe. Thus, there are no candidates for dark matter in the standard model.

2.2.3 Hierarchy Problem

Another issue that makes the standard model much less appealing as a complete theory are the extremely large quantum corrections to the Higgs boson mass. These corrections stem from the extreme disparity of the strength of the gravitational interaction with the other three fundamental forces, known as the Hierarchy problem. To get an idea of the relative strength of the electromagnetic and gravitational forces, the force between two protons due to each can be compared. Using the classical force definitions, $F_{\text{gravity}} = Gm_p^2/r^2$ and $F_{\text{EM}} = ke^2/r^2$ where G is the

gravitational constant, m_p is the proton mass, k is Coulomb's constant, and e is the charge of the proton. This gives the extremely small ratio $F_{\text{gravity}}/F_{\text{EM}} \sim 10^{-36}$! However, if the mass of the particles in this comparison were instead 10^{18} GeV, the strengths of the two forces would be similar. This mass scale is known as the Planck Mass, $M_{\text{P}} \sim 10^{18}$ GeV, and is the scale at which the gravitational force becomes comparable in strength to the other fundamental forces.

The vastly different scale of the gravitational force affects the mass of the Higgs boson through loop diagrams. A few relevant one loop Feynman diagrams are shown in Fig. 2.5. In each diagram, there is an undetermined momentum in the loop that is integrated over. In performing these integrals, it is necessary to introduce an upper limit on the momentum, call it Λ, at which new physics becomes relevant and the current theory is no longer valid. For fermionic loops, the correction to the Higgs mass is $\Delta m_H^2 = -\frac{|\lambda_f|^2}{8\pi^2}\Lambda^2 + \ldots$, taken from Ref. [39], where $\lambda_f \propto m_f$ is the Higgs coupling to the fermion. The additional omitted terms in the sum are proportional to $\log \Lambda$ and hence much smaller than the first term. The massive bosons also contribute terms proportional to Λ^2. Because the coupling strength of the Higgs increases with mass, the dominant loop correction to the Higgs mass comes from top quark loops.

If there is no new physics beyond the standard model besides gravity, then $\Lambda \sim M_{\text{P}}$. However, the mass of the Higgs boson is $\mathcal{O}(100 \text{ GeV})$. This comes from

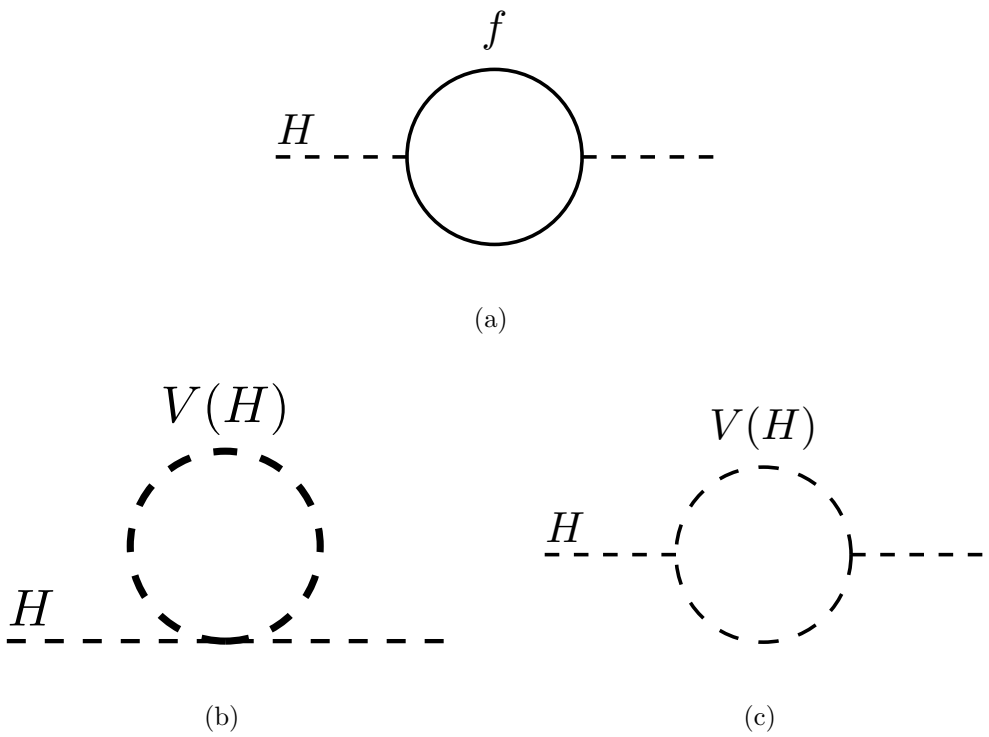

Figure 2.5: Single loop Feynman diagrams contributing to the Higgs boson mass. (a) shows a fermionic loop, while (b) and (c) show loops with bosons. In (a), any fermion other than a neutrino can contribute. In (b) and (c), the massive vector bosons and Higgs can contribute. The V represents either a W or Z vector boson.

the fact that fits of the SM parameters prefer a Higgs in this mass range [19]. And if the recently discovered particle, which is consistent with the Higgs boson [24, 25], turns out to actually be the Higgs boson, its mass is about 125 GeV. In order to reconcile the $\mathcal{O}(10^{18}$ GeV) loop diagram corrections to the Higgs mass with the actual Higgs mass, the bare mass in the theory would need to be fine tuned to 16 orders of magnitude. While such fine tuning is in principle possible, it is a very un-natural feature of the SM. Theories that are able to mitigate this fine tuning are therefore appealing.

2.3 Supersymmetry

2.3.1 Basics of SUSY

One class of models of physics beyond the standard model that has the potential to address the issues in the previous section are those utilizing Supersymmetry (SUSY) [40, 41, 42, 43, 44, 45]. Supersymmetry is a spacetime symmetry relating fermions and bosons. Every boson or fermion has a corresponding fermionic or bosonic, respectively, supersymmetric partner, also known as a superpartner. Groupings of such partners are referred to as supermultiplets. For reasons that will be explained, no particle in the SM can be the superpartner of another par-

ticle in the SM and hence the particle content of the standard model is at least doubled in supersymmetric extensions.

The following naming conventions will be used to refer to the SUSY partners of SM particles. In general, such a SUSY partner is called a *sparticle*. Superpartners of SM fermions are generally called *sfermions* and more specifically named by simply adding an "s" in front of the corresponding SM fermion name. Superpartners of SM bosons are generally called *gauginos* and more specifically named by changing the corresponding SM boson name to end in "ino", e.g., *gluino*. The symbol denoting a superpartner of a standard model particle is just the standard model symbol with a tilde ($\sim$) over it, e.g., a stop is denoted $\tilde{t}$.

The generators of supersymmetric transformations, Q and $Q^\dagger$, can be used in some linear combination to transform a particle into its superpartner, up to a spacetime translation or rotation. The properties of these generators determine many of the important features of supersymmetry. Because the generators commute with the squared-mass operator, P^2, particles in a supermultiplet have the same mass. Additional properties of Q and $Q^\dagger$ can be used to show that the number of fermionic and bosonic degrees of freedom in a supermultiplet are equal. Finally, the SUSY generators commute with the gauge transformation generators, so superpartners behave the same under all forces as their corresponding SM partners, i.e., have the same charges.

There are three fundamental types of supermultiplets, out of which the entire SUSY particle content can be built.

1. A chiral supermultiplet consists of a spin 1/2 particle, which has two fermionic degrees of freedom from its two possible spin states, and a complex scalar field, which has two bosonic degrees of freedom from its real and complex parts.

2. A gauge supermultiplet consistes of a spin 1 vector boson and a spin 1/2 fermion. Just as in the SM, the vector boson is a massless gauge boson before spontaneous gauge symmetry breaking, and therefore the fermion must also have no mass before this symmetry breaking. Since they are each massless, each has 2 degrees of freedom due to possible spin states.

3. A graviton supermultiplet consists of a spin 2 massless graviton, the particle that would mediate gravitational interactions, and its superpartner with spin of 3/2, the gravitino.

In the SM, all vector bosons belong to a gauge supermultiplet as no other supermultiplet contains spin 1 particles. Because right and left handed gauge bosons must have the same interactions via the weak force, so too must their superpartners in the gauge supermultiplet. This means that all the SM fermions, which behave differently under the weak force depending on their handedness,

must be in chiral supermultiplets. The SM Higgs boson corresponds to a superposition of the neutral scalar components of two chiral supermultiplets. Two Higgs supermultiplets are necessary to give mass to the up-type and down-type quarks.

In order to cancel the quadratic divergences to m_H^2, described in Sec. 2.2.3, SUSY utilizes the fact that loops with bosons and fermions have contributions with different signs. Together with the fact that the couplings of the particles in a supermultiplet to the Higgs boson are related, this leads to the cancellation of the quadratic divergences. Figures 2.5(a) and 2.6 show the relevant one-loop diagrams from a chiral supermultiplet. The total contribution from these diagrams is given by

$$\Delta m_H^2 = \frac{1}{8\pi^2}(\lambda_{\tilde{f}} - |\lambda_f|^2)\Lambda^2 + \ldots, \tag{2.3}$$

taken from Ref. [39], where λ_f and $\lambda_{\tilde{f}}$ are the Higgs couplings to the fermion and scalar superpartners, respectively. The additional omitted terms in the sum are proportional to $\log \Lambda$ and hence much smaller than the first term. Because $\lambda_{\tilde{f}} = |\lambda_f|^2$ in a chiral supermultiplet, the quadratic divergence in 2.3 cancels. In fact, supersymmetry causes the quadratic divergences due to both SM fermions and bosons to cancel for all numbers of loops.

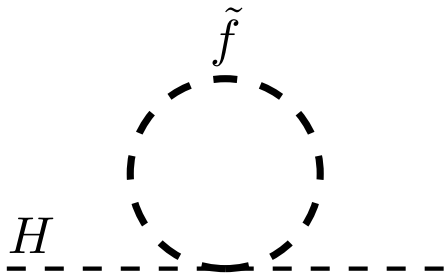

Figure 2.6: Feynman diagram of a one-loop contribution to the Higgs boson mass from a scalar in a chiral supermultiplet. This diagram cancels the quadratic divergence from the corresponding fermionic superpartner, which has its one-loop diagram shown in Fig. 2.5(a).

2.3.2 Supersymmetry is Broken

The major problem with the existence of supersymmetry, as described thus far, is that if it is an exact symmetry, then the superpartners for many, particularly the lightest, of the SM particles would have already been observed. Therefore, if SUSY exists, it must be a broken symmetry so that superpartners can be massive enough to thus far escape detection. However, to guarantee that the quadratic divergences in m_H^2 cancel, only certain types of supersymmetry breaking are possible. In particular, the couplings arising from the SUSY breaking must have positive mass dimension, known as soft supersymmetry breaking.

The Lagrangian for soft supersymmetry breaking is

$$\begin{aligned}\mathcal{L}_{\text{soft}} = &-\frac{1}{2}\left(M_3\tilde{\mathbf{G}}\tilde{\mathbf{G}} + M_2\tilde{\mathbf{W}}\tilde{\mathbf{W}} + M_1\tilde{B}\tilde{B} + \text{h.c.}\right) \\ &-\left(\tilde{U}^\dagger\,\mathbf{a_u}\,\tilde{Q}H_u - \tilde{D}^\dagger\,\mathbf{a_d}\,\tilde{Q}H_d - \tilde{E}^\dagger\,\mathbf{a_e}\,\tilde{L}H_d + \text{h.c.}\right) \\ &-\tilde{Q}^\dagger\,\mathbf{m_Q^2}\,\tilde{Q} - \tilde{U}^\dagger\,\mathbf{m_u^2}\,\tilde{U} - \tilde{D}^\dagger\,\mathbf{m_d^2}\,\tilde{D} - \tilde{L}^\dagger\,\mathbf{m_L^2}\,\tilde{L} - \tilde{E}^\dagger\,\mathbf{m_e^2}\,\tilde{E} \\ &-\ m_{H_u}^2\,|H_u|^2 - m_{H_d}^2\,|H_d|^2 - (bH_uH_d + \text{h.c.})\,,\end{aligned} \tag{2.4}$$

where h.c. stands for hermitian conjugate. The fields in this Lagrangian are just the supersymmetrized versions of those in Tables 2.1 and 2.2, with the exception of the two Higgs fields, H_u and H_d. The $\mathbf{a_u}$, $\mathbf{a_d}$, and $\mathbf{a_e}$ are complex matrices in family space, i.e., 3×3, with mass dimension one. The $\mathbf{m_Q^2}$, $\mathbf{m_u^2}$, $\mathbf{m_d^2}$, $\mathbf{m_L^2}$, and $\mathbf{m_e^2}$ are hermitian matrices in family space with mass dimension two. Each of $m_{H_u}^2$, $m_{H_d}^2$, and b have mass dimension two and contribute to the Higgs potential.

One important consequence of soft SUSY breaking is the mixing of the sfermions. The third line of Eq. 2.4 mixes the different generations of sfermions of the same type and handedness. For example, the left-handed down-type squark mass eigenstates can be linear combinations of the left-handed flavor eigenstates $\tilde{d}$, $\tilde{s}$, and $\tilde{b}$. Additional mixing between the right and left-handed sfermion states is possible due to the second line of Eq. 2.4, e.g., the bottom squark mass eigenstates can be a superposition of $\tilde{b}_L$ and $\tilde{b}_R$ as well as the left and right-handed components of the other down-type squarks.

These mixings can have significant effects in terms of flavor changing neutral currents (FCNC) and CP violation, each of which is small in the standard model. Therefore, related experimental tests can place meaningful constraints on the parameters of soft SUSY breaking. The most stringent constraint on $\tilde{e} - \tilde{\mu}$ mixing is the upper limit on BR($\mu \to e\gamma$). Another important FCNC constraint on SUSY breaking comes from $K_L - K_S$ mixing, specifically the value of the mass difference between K_L and K_S, which constrains $\tilde{s} - \tilde{d}$ mixing. Upper limits on the electric dipole moment of electrons and neutrons constrain CP violating phases in the SUSY breaking Lagrangian. A summary of FCNC and CP violation constraints on the SM can be found in Refs. [46, 47]. In general, mixing in the first two generations is more constrained than in the third generation.

Electroweak symmetry breaking, along with the soft SUSY breaking terms with M_1 and M_2 in Eq. 2.4, provides the mixing of the gauginos and higgsinos. The resulting mass states are referred to as neutralinos ($\tilde{\chi}_i^0$, where $i = 1, 2, 3, 4$ in order of increasing mass) if they are neutral or chaginos ($\tilde{\chi}_i^{\pm}$, where $i = 1, 2$ in order of increasing mass) if they are charged. Neutralinos result from the mixing of the neutral higgsinos with the bino and neutral wino while charginos result from the mixing of the charged higgsinos with the charged winos. Gluinos are not included in the gaugino mixing because they are in a color octet and hence cannot mix with the other color-neutral gauginos.

In writing Eq. 2.4, terms that are otherwise allowed by Lorentz and gauge invariance, but which violate lepton and baryon number conservation, have been omitted. These types of interactions have not been experimentally observed, severely constraining such SUSY breaking couplings; see Ref. [48] for a review. One such constraint comes from the non-observation of proton decay into a lepton and meson, e.g., $p \to e\pi^0$, which alters both lepton and baryon number by one.

Given these strong experimental constraints, it is necessary to theoretically explain why the otherwise allowed lepton and baryon number violating couplings have not produced any observable effects. One possible explanation is via a symmetry called R-parity, which is a multiplicative quantum number with value $P_R = 1$ for SM particles and $P_R = -1$ for sparticles. Each vertex must have an overall R-parity value of 1, and hence must contain an even number of sparticles. This implies that sparticles are produced in pairs and the lightest supersymmetric particle (LSP) cannot decay. In many SUSY models, the lightest neutralino, $\tilde{\chi}_1^0$, is the LSP. Neutral charge combined with stability due to R-parity make the $\tilde{\chi}_1^0$ a strong dark matter candidate [49]. For this reason, this document will assume the LSP is the $\tilde{\chi}_1^0$ from here on.

While there are other possibilities to circumvent experiment constraints, Ref. [50] for example, this analysis assumes R-Parity conservation. With this assumption, the Minimal Supersymmetric Standard Model (MSSM) describes the minimum

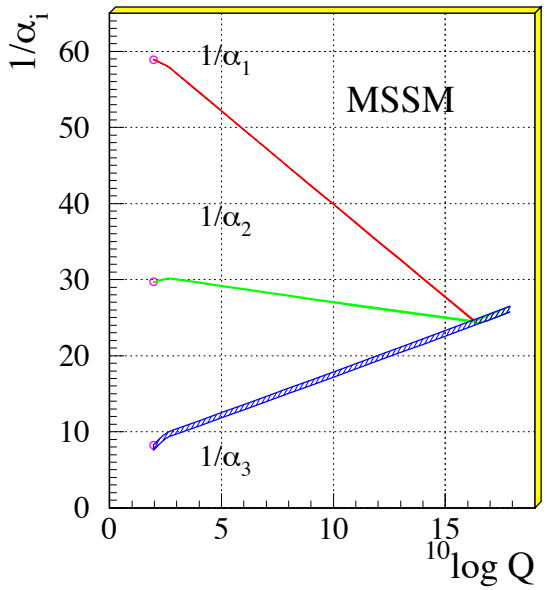

Figure 2.7: The running of the inverse coupling constants in the MSSM versus energy, with GeV units. α_1 corresponds to the electromagnetic force, α_2 corresponds to the weak force, and α_3 corresponds to the strong force. Figure taken from Ref. [33].

particle content needed for supersymmetry along with all of the corresponding soft supersymmetry breaking interactions. Unlike in the standard model, the strong, weak, and electromagnetic gauge couplings unify at high energies within the MSSM framework. This is illustrated in Fig. 2.7, which shows the unification at the $m_{\mathrm{GUT}} \approx 10^{16}$ GeV scale.

2.3.3 Naturalness

If soft SUSY breaking is enforced, then the square of the Higgs mass will have contributions from each sparticle i proportional to $m_i^2 \lambda_i^{(2)} \log \Lambda$, where λ_i is the coupling constant of the sparticle to the Higgs. The fine tuning of a SUSY model can be defined as the ratio of the corrections to the Higgs mass squared divided by the Higgs mass squared, $\Delta m_H^2 / m_H^2$. Ultimately there is no strict upper limit on the amount of fine tuning, but *natural* models [51, 52, 53, 54] typically have fine tuning of $\mathcal{O}(100)$ or less.

Depending on the acceptable level of fine tuning, one can set rough upper limits on the sparticle masses. Since top squarks have the strongest coupling to the Higgs, their mass is most stringently constrained for a given amount of fine tuning. For models with fine tuning by a factor of 100, the stop mass must be roughly 1 TeV or less. The upper limit on this mass scales with the square root of the amount of fine tuning. While gluinos do not directly couple to the Higgs, they contribute to the fine tuning via loop corrections to the stop mass. This gives an upper limit on the gluino mass which roughly a factor of two greater than that on the stop mass. Due to its 8 TeV center-of-mass energy, much of the parameter space with stop and gluino masses $\lesssim$ 1 TeV is accessible at the LHC, making searches for these particles quite interesting.

Because gluinos have a much greater production cross section than stops and should not be too much heavier due to naturalness arguments, searches specifically targeting gluino pair production are well motivated. Additionally, because stops are likely the lightest squarks, it is probable that the gluinos will decay through stops, i.e $\tilde{g} \to t\tilde{t}^{(*)}$, with the subsequent stop decay $\tilde{t} \to t\tilde{\chi}_1^0$. This would result in a spectacular four top quark and two neutralino final state, which is the primary target of this search.

2.3.4 Production of Sparticles at the LHC

At the LHC, production of squarks and gluinos has the advantage of being mediated by the strong force. This results in significantly larger cross sections, for the same mass, than electroweak production of charginos, neutralinos, and sleptons. Figure 2.8 shows the tree-level production diagrams at the LHC for gluino pairs.

The cross section at next to leading order (NLO) with next to leading logarithmic (NLL) contributions [55, 56, 57, 58, 59], denoted $\sigma^{\text{NLO+NLL}}$, for various sparticles at the LHC are shown in Fig. 2.9. For simplicity, each cross section is computed with all other SUSY particles decoupled by setting their masses arbitrarily high. Because it is mediated weakly, the chargino-neutralino production cross section is the lowest shown in this figure. Stop and gluino pairs are produced

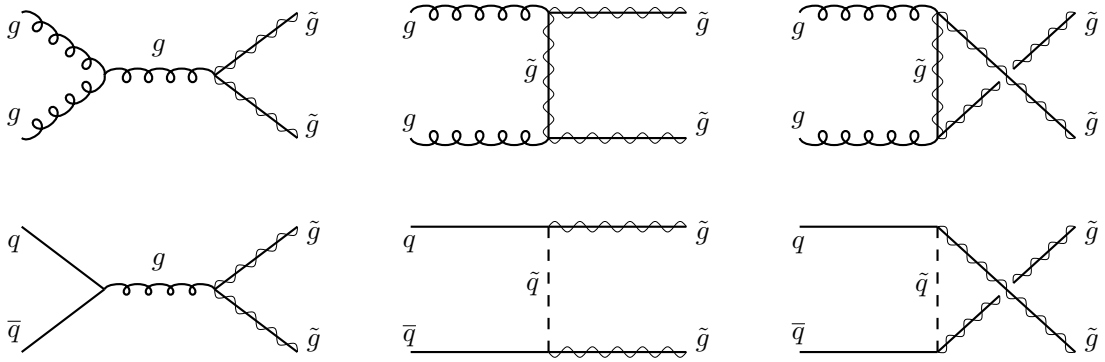

Figure 2.8: Tree-level gluino pair production diagrams at the LHC. Both gluon-gluon fusion (top row) and quark anti-quark pairs (bottom row) contribute. Figure taken from Ref. [39].

via the strong force and therefore have higher production cross sections. Factors contributing to gluinos having a higher production cross section than stops are that there are more color states of the gluinos than for stops, 8 vs 3, and the spin 1/2 gluinos can be produced by a larger number of initial spin states than the scalar stops.

2.3.5 Simplified Models

Results cannot be efficiently interpreted in the context of the MSSM due to its large number, over 100, of degrees of freedom. Assumptions about the mechanism by which SUSY is broken lead to various constrained SUSY models, which have just a handful of parameters, and hence can be used as a context in which to interpret search results. However, this is not ideal as the constraints on these

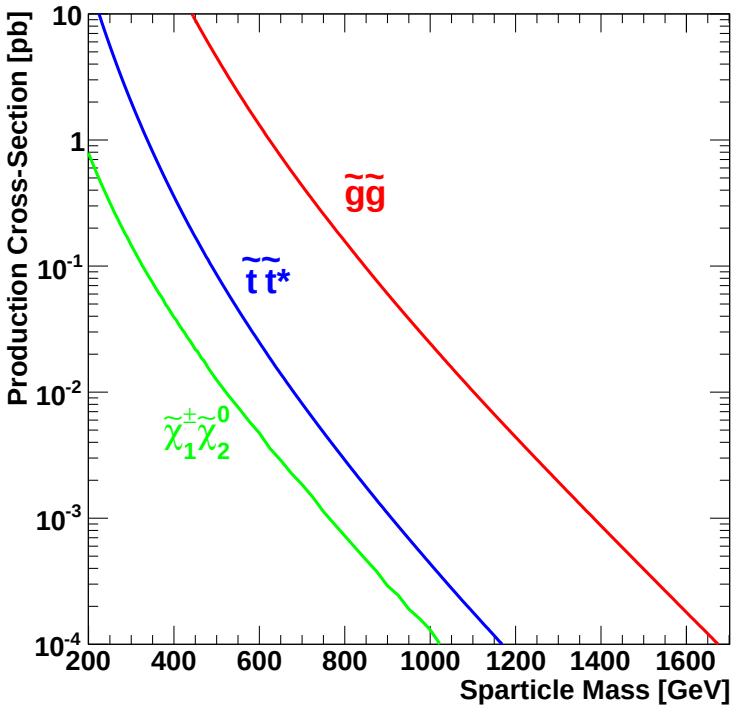

Figure 2.9: $\sigma^{\text{NLO+NLL}}$ for some sparticles at the LHC at a center of mass energy of 8 TeV. For simplicity, each cross section is computed with all other SUSY particles decoupled. For chargino-neutralino production, the $\tilde{\chi}_1^{\pm}$ and $\tilde{\chi}_2^0$ are assumed to have the same mass. The uncertainties on each of these cross sections are not shown but are small compared to the differences between the curves.

models can be somewhat arbitrary, and the plethora of different modes of sparticle production and decay make re-interpreting the results in the context of another model highly non-trivial.

An approach that alleviates these problems is to interpret a search in terms of a Simplified Model Spectra (SMS) framework [60, 61, 62]. As their name suggests, simplified models have a very limited sparticle content, typically just two or three different sparticles. The same sparticles are produced and decay through the same channels in each event. For example, one of the most utilized SMS corresponds to top squark pair production, where each top squark decays to a top quark and the LSP $\tilde{\chi}_1^0$. The models are parametrized solely in terms of the sparticle masses, which generally leads to a physically intuitive picture of the sensitivity of the analysis. The simplicity of these models allows for a more convenient re-interpretation of the result in the context of additional models. For these reasons, it has become common practice to use simplified models to interpret SUSY searches at CMS. A wide range of such results are shown in [63].

The SMSs used in this analysis correspond to gluino pair production leading to a final state with four top quarks, which is motivated by naturalness arguments in Sec. 2.3.3. The simplest of these models is T1tttt, which ignores stops and has the gluino undergo a 3-body decay to $t\bar{t}\tilde{\chi}_1^0$. The free parameters of this model are the gluino and neutralino masses. The other simplified models used are T5tttt

and T1t1t, in which the gluino decays via a stop, intermediate in mass between the gluino and neutralino. To reduce the number of free parameters from 3 to 2, the neutralino mass is fixed to 50 GeV in T5tttt and the gluino mass is fixed to 1 TeV in T1t1t. This means the free parameters are the stop and gluino masses in T5tttt, and the stop and neutralino masses in T1t1t. Figure 2.10 illustrates the gluino decay in each of these SMS.

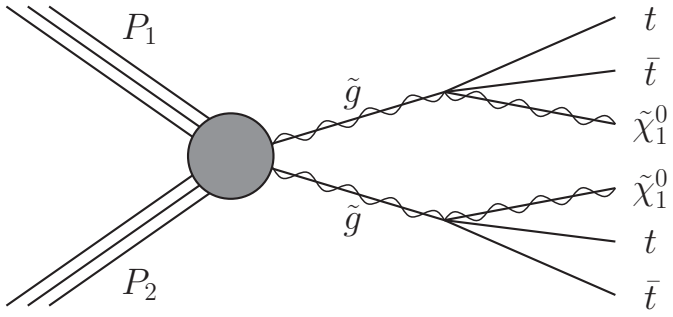

(a)

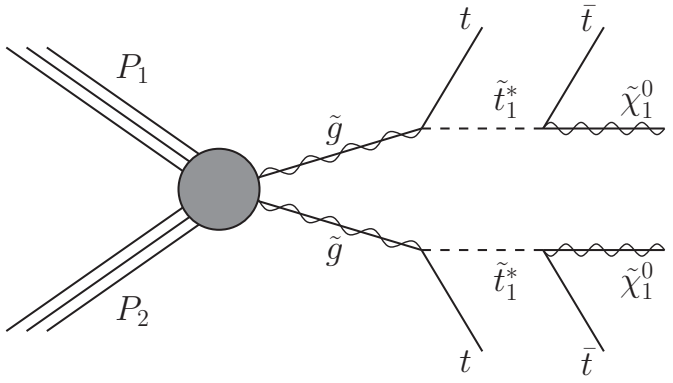

(b)

Figure 2.10: Feynman diagrams corresponding to simplified models of gluino production with a four top and two LSP final state. (a) corresponds to the T1tttt SMS, in which gluinos 3-body decay via $\tilde{g} \to t\bar{t}\tilde{\chi}_1^0$. (b) illustrates the T5tttt and T1t1t SMSs, in which gluinos decay via an intermediate mass stop, i.e., $\tilde{g} \to t\tilde{t}^{(*)} \to t\bar{t}\tilde{\chi}_1^0$.

Chapter 3

Experimental Apparatus

This analysis utilizes data from proton-proton collisions at center of mass energy of 8 TeV from the Large Hadron Collider (LHC) recorded with the Compact Muon Solenoid (CMS) detector. The LHC produces the highest energy proton-proton collisions in the world and allows higher energy scales to be probed for new physics beyond the standard model than ever before. Such experimental probes would, however, not be possible without the ability to observe with high precision the results of these collisions, as is done by CMS. This chapter briefly describes the basic features of the LHC and CMS.

3.1 The Large Hadron Collider

The LHC [64] is located at the European Organization for Nuclear Research (CERN) near Geneva, Switzerland. The LHC ring, which runs underneath the French-Swiss border, is 26.7 km long and consists of two side-by-side proton

beams circulating in opposite directions. The LHC design provides for a maximum collision energy of 14 TeV and maximum instantaneous luminosity of $L = 10^{34}$ cm^{-2}s^{-1}. The LHC also has the ability to accelerate and collide lead ion beams, but such data is not included in this analysis.

Protons are fed into the LHC ring by an injector complex, as shown in Fig. 3.1, consisting of the Linac2 linear accelerator, Proton Synchrotron Booster (PSB), Proton Synchrotron (PS), and finally Super Proton Synchrotron (SPS). Each successive accelerator increases the kinetic energy of the protons by about an order of magnitude. Around the LHC ring are four points at which the collisions occur and are observed by an experimental installation. Figure 3.1 also shows these four main experiments around the LHC ring, consisting of LHC-B, which is primarily used for B-hadron physics; ALICE, which is primarily used for physics with lead ion collisions; and ATLAS and CMS, which are each general-purpose detectors designed to provide data for a wide variety of physics analyses.

In order to manipulate the proton beams, the LHC employs over nine thousand magnets. The beams are bent by 1232 superconducting dipole magnets made from NbTi wire filament and cooled with superfluid helium to a temperature of less than 2 K. These dipoles are designed to provide a maximum field of 8.33 T and collectively store roughly 11 GJ of energy. The beams are focused and corrected with higher multipole magnets, most of which are the 392 quadrupoles. The

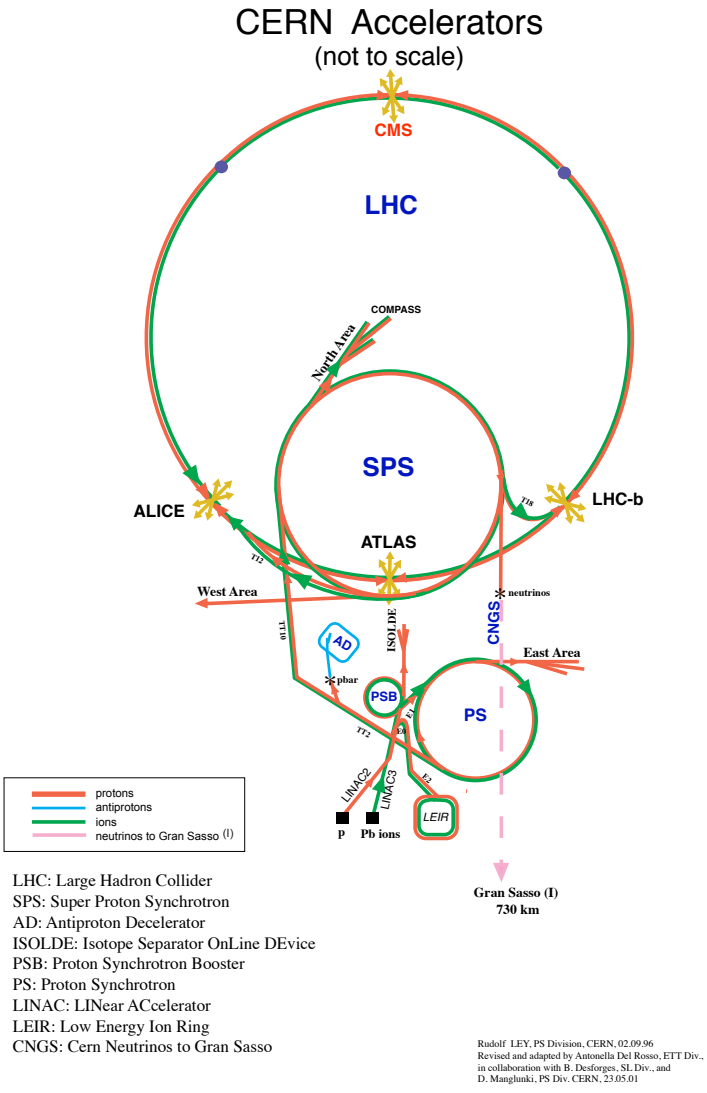

Figure 3.1: Diagram of the accelerator complex at CERN. Figure taken from Ref. [65].

tremendous amount of energy stored in the LHC magnets makes it imperative that protections are put in place to safely dissipate this energy in the event of a quench.

Protons circulate in the LHC in bunches of $\mathcal{O}(10^{11})$ protons with 50 ns spacing, although the nominal design of the LHC allows for minimum spacing of 25 ns. These bunches are formed with the correct spacing in the PS. In order for the large energy in each beam, 360 MJ at the nominal LHC design, to be safely and effectively dumped from the LHC, there is a 3 μs section of each beam with no bunches, called the abort gap. This length of time is matched to the LHC beam extraction kicker magnet rise time, so that the beams can be re-directed to an external absorber without causing damage.

The data used in this analysis come from the 2012 running period of the LHC. The 8 TeV center-of-mass energy of the *pp* collisions during this time was an increase over the 7 TeV collisions in previous years. Furthermore, the peak instantaneous luminosity achieved in 2012 was 7.7×10^{33} cm^{-2}s^{-1}, and the total integrated luminosity collected was roughly four times more than had been accumulated previously. These increases in luminosity and energy make searches for new physics in the 2012 dataset promising.

Beginning in 2013, the LHC has entered a roughly two year shutdown period in which upgrades and renovations will be made to the LHC and other components

of the CERN accelerator complex as well as to the experiments positioned around the ring. This means the 2012 LHC data is likely to provide the definitive word on collider-based searches for new physics until the LHC restarts at the conclusion of the current shutdown. The LHC is scheduled to recommence operations in 2015 with the goal of providing higher energy *pp* collisions at roughly 13 TeV, beginning another period of exciting potential for discovery.

3.2 The Compact Muon Solenoid

The Compact Muon Solenoid detector is a multi-purpose device, optimized to measure the particles produced in collisions at the LHC. CMS is situated roughly 100 m underground near the small town of Cessy, France. Despite its name, the CMS detector is quite large compared to previous generations of collider detectors, with a 21.6 m length, 14.6 m diameter, and 12500 t weight. The primary goals for the experiment are to study the Higgs boson and search for new physics, such as Supersymmetry, at the TeV scale.

CMS comprises multiple sub-detectors, shown in Fig. 3.2, nested in concentric cylinders about the LHC beam axis and centered on the collision point. Closest to the collision point, is the tracking system, which measures the trajectories of charged particles. The next closest sub-system is the electromagnetic calorimeter,

which measures the energy of electrons and photons, followed by the hadronic calorimeter, which measures the energy of hadrons. These are all enclosed by the superconducting solenoid, whose magnetic field bends the trajectories of charged particles and allows for their momentum to be measured by the tracker. Finally, the muon system is outside the solenoid but within its return field. CMS has additional specialized calorimetry located very near the beam line but far away from the collision point which is not utilized in the measurement described herein. Figure 3.3 indicates the behavior of particles produced in a collision as they traverse the different sub-detectors. Because each sub-detector measures a different aspect of the particles produced in the collision (also called an event), a full description is achieved only by combining the measurements from all of the sub-detectors.

Because each saved event requires a significant amount of bandwidth and disk space to transmit and store as well as computing power to reconstruct, it is not feasible to save events anywhere near the nominal 40 MHz LHC collision rate. To reduce the rate by the nearly 5 orders of magnitude while still saving the most interesting events, CMS employs a dual stage trigger system. The first stage is known as the Level-1 (L1) trigger and reduces the rate to less than 100 kHz while the second stage is known as the High Level Trigger (HLT) and reduces the rate to less than 1000 Hz.

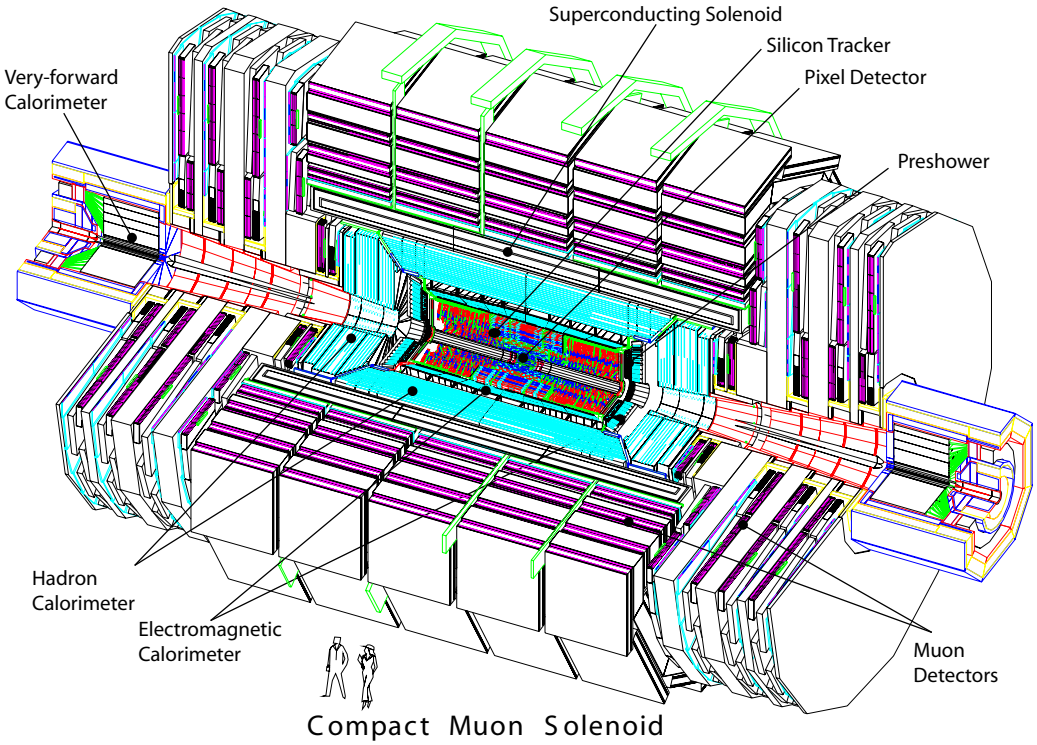

Figure 3.2: A perspective view of the CMS detector, indicating the location and orientation of the different sub-detectors. Figure taken from Ref. [66].

CMS uses a right-handed coordinate system centered at the nominal collision point. The x-axis points toward the center of the LHC ring while the y-axis points vertically upward. The z-axis, therefore, points along the direction of the counter-clockwise circulating beam. The pseudorapidity η is defined as $\eta = -\ln[\tan(\theta/2)]$, where θ is the polar angle with respect to the z-axis. Within the xy plane, the azimuthal angle ϕ is measured counter-clockwise from the x-axis, and the radial coordinate r is the distance from the z-axis. The xy plane is

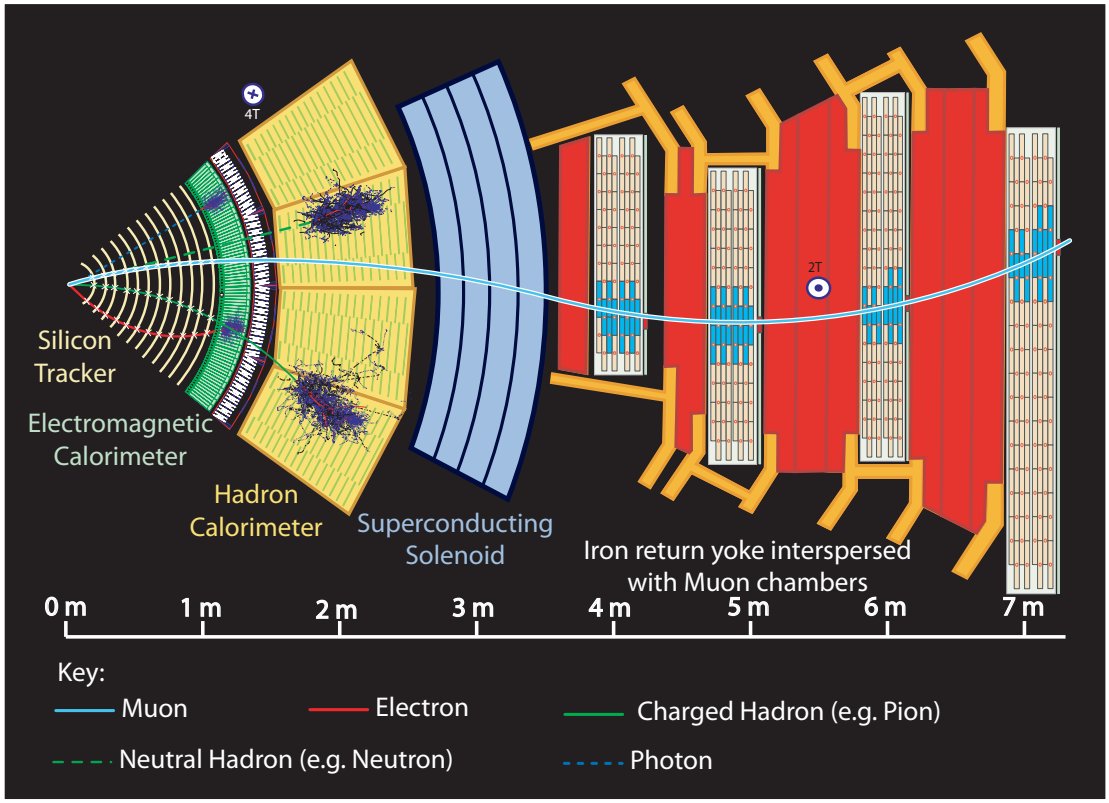

Figure 3.3: A transverse slice of the CMS detector, indicating the behavior of various particles in the different sub-detectors. The scale indicates the distance from the collision point. Figure taken from Ref. [67].

referred to as the transverse plane. The transverse momentum (p_T) of a particle refers to its momentum within this plane.

In order to accomplish its physics goals while coping with the extreme LHC environment, great care was taken in the CMS design to satisfy the following general constraints. First, the detector should be as hermetic as possible such that missing transverse momentum, due to the presence of a neutrino or some

as yet undiscovered weakly interacting particle, can be reliably inferred. Due to the composite nature of protons, the net momentum of a collision along the beam axis is not constrained to be zero, and thus only the transverse component of the net momentum is expected to balance. Next, the detector components must be able to withstand large doses of radiation, due to the high LHC collision rate, before significantly degrading in functionality. A related constraint is that the detector must have enough spatial granularity so that the large number of particles produced in the collisions can generally be distinctly resolved. Finally, the detector channels should have read-out and synchronization compatible with the nominal 25 ns collision rate.

The remainder of this section is devoted to giving an overview of the various sub-detector systems that comprise CMS. A more detailed description can be found in Ref. [66].

3.2.1 Solenoid

CMS employs a large, cylindrical, superconducting solenoid to provide a magnetic field which curves the trajectories of charged particles via the Lorentz force. The magnetic field of the solenoid is parallel to the beam axis, which causes the trajectories of charged particles to curve in the transverse plane. The measured curvature allows a determination of the momentum. The larger the magnetic

field, the greater the curvature of the track and precision of the momentum measurement. This curvature is measured for charged particles by the tracker, which is inside the solenoid, and for muons by the muon system, which is outside the solenoid and relies on its return field.

The 15.5 m long, 6.3 m diameter, 220 t solenoid is housed in an iron yoke and provides a nearly uniform 3.8 T magnetic field inside the tracker. The extremely high magnetic field requires that the solenoid be superconducting. So that the magnet is not damaged by the force placed on its coils due to its own magnetic field, the coils are incorporated into the structural material of the magnet. This feature also helps make the solenoid as thin as possible to reduce the potential for disrupting the path of particles traversing the detector.

The large energy stored in the solenoid, 2.3 GJ at 3.8 T, combined with its superconducting nature, result in significant difficulties that must be overcome to ensure safe operation. Of primary concern, is the case of a superconductive-to-resistive transition, or quench. When this occurs, the tremendous current, 18 kA at 3.8 T, causes the resistive section of the coil to heat very quickly. To avoid damaging the resistive section of the coil through extreme thermal stress, a quench detection system disconnects the power source and triggers a fast discharge of the magnet. In a fast discharge, eddy currents are induced in the external mandrel of the solenoid, which evenly heats the entire coil above the critical temperature.

So much energy is released during a fast quench that it can take up to three days to cool the magnet back below the critical temperature.

3.2.2 Tracker

The innermost sub-detector of CMS is the tracking system, which measures the trajectory of charged particles. The tracker system consists of two main components: a pixel detector immediately surrounding the beam pipe, and a silicon strip detector which surrounds the pixel detector. In the presence of the magnetic field from the superconducting solenoid, the curvature of a track allows for the determination of its momentum. Centered around the collision point, the tracker has diameter of 2.5 m and length of 5.8 m, so that its coverage extends to $|\eta| < 2.5$. The exceptional granularity of the tracker allows for resolution of better than 1% on p_T and roughly 10 μm on the transverse impact parameter across a wide range of track p_T values. The efficient and accurate particle trajectory measurements provided by the tracker are essential to the physics program of CMS.

The tracker sensors are silicon-based and constitute the largest ever silicon tracker, with 200 m^2 of active sensing area. When a charged particle traverses one of the sensors, it ionizes atoms in the depletion region, causing current to flow. The locations of the sensors which exhibit such ionization current allow the

paths of charged particles to be inferred. Such inferences, however, can be biased or entirely wrong if there are multiple charged particles which traverse the same sensor. To reduce this potential, and keep the occupancy per sensor at or below the percent level, the tracker sensors exhibit a high degree of granularity, with the smallest sensors nearest the collision point where the density of particles per unit area is largest. This is achieved by subdividing the tracker into an inner pixel detector and an outer strip tracker, which together have 75 million readout channels.

Besides the challenge of operating and monitoring such a large number of sensors, the biggest challenge facing the tracker is reducing and coping with the effects of radiation damage. The on-detector read-out chips used by the tracker are quite radiation hard, meaning that the radiation damage to the sensors is the limiting factor. The main effect of radiation damage on the silicon is damage to the crystal lattice structure which reduces the signal, necessitates higher operational bias voltages, and significantly increases the leakage current. To avoid further damage from reverse annealing, the sensors must be operated at well below 0°C. Furthermore, such low operating temperatures are beneficial because they reduce the leakage currents. This is important because the leakage currents, which warm the silicon, have an exponential dependence on temperature and therefore cause positive feedback and potential thermal runaway.

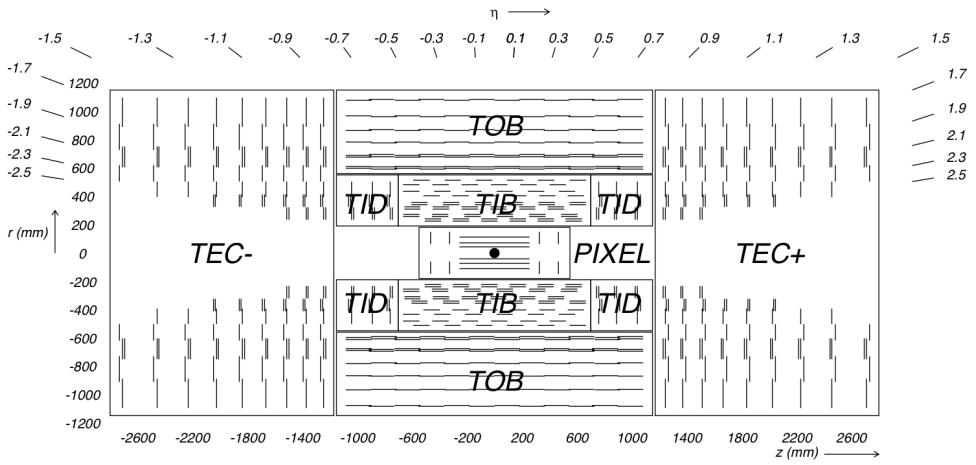

Figure 3.4: Cross-section view of the tracker in the rz plane with labels to denote the different sections of the sub-detector. Lines represent detector modules. Figure taken from Ref. [66].

Pixel Tracker

The inner pixel portion of the tracker consists of three cylindrical barrel layers at 4.4, 7.3, and 10.2 cm from the beam axis and two endcap disks spanning $r = 6 - 15$ cm on either side at $z = \pm 34.5, \pm 46.5$ cm. The arrangement of the pixel tracker can be seen at the center of Fig. 3.4. The silicon pixel size is 100×150 μm^2, so that the pixel tracker covers an area of around 1 m^2 with 66 million pixels. The sensing silicon is constructed with an n-on-n design, which allows for functionality even after very high radiation doses.

Read-out chips amplify and buffer the charge from the sensors to which they are attached. Due to the tremendously large number of pixel channels, their read-

out is zero-suppressed with adjustable thresholds in order to reduce the amount of data to a manageable level. In the case of a trigger, the zero-suppressed analog pixel charges are transferred to digitization modules in the service cavern via optical link. The analog readout aids in separating signal and noise as well as identifying pixels hit by multiple charged particles. Once the analog optical signal has been digitized, it is passed on to the central data acquisition (DAQ) system.

Strip Tracker

The silicon strip portion of the detector surrounds the pixels and consequently must have a much large active area, 198 m^2, of silicon to ensure the same coverage in η and ϕ. Long silicon strips are used to keep the number of readout channels, 9.3 million, at a reasonable level. The width of the strips increases with radius from 80 to 180 μm in the transverse plane while the length increases from 10 to 25 cm. The narrow dimension of the strips is chosen to be primarily in the transverse plane to maximize the precision with which the radius of curvature, and hence momentum, can be measured.

The strip tracker consists of 4 sub-systems, which fit together to provide multiple measurement points of particle trajectories with $|\eta| < 2.5$. For nearly this entire η range, there are at least 9 potential measurement points. The full extent of the strip tracker is $|z| < 282$ cm and $20 < r < 116$ cm. The Tracker Inner Barrel

(TIB) and Tracker Inner Disks (TID) are the sub-systems at the lowest radius and consist of 4 cylindrical barrel layers flanked at each end by 3 disks. The Tracker Outer Barrel (TOB) surrounds the TIB/TID and consists of 6 cylindrical layers. Finally, the Tracker EndCaps (TEC), which consist of 9 disks, are positioned just outside the other sub-systems in z and cover particle trajectories up to η of 2.5. This arrangement of the sub-systems can be seen in Fig. 3.4.

The silicon strips are arranged in groups of a few hundred to form modules. Because of the varied geometry of the sub-systems used to fill the tracking volume, modules come in several shapes and sizes. The first two layers or rings of each sub-system as well as the fifth rings of the TEC have a second strip detector module mounted to the back of each module at a stereo angle of 100 mrad. This provides a more precise measurement of z in the barrel and r in the disks.

Read-out chips amplify, shape, and buffer the charge from the strips to which they are attached. In the case of a trigger, the analog charge of each strip is transferred out of the detector to Front End Driver (FED) modules via optical link. Unlike in the pixels, there is no zero suppression in this step. After the signals are digitized in the FEDs, pedestal corrections are applied and the common mode noise subtracted. In normal data taking, the FED performs zero suppression by only passing clusters of channels and their corresponding signals to the central DAQ which are potentially relevant for track reconstruction.

3.2.3 Electromagnetic Calorimeter

The electromagnetic calorimeter (ECAL) of CMS is primarily designed to measure the energy of electrons and photons with high precision. It consists of a hermetic arrangement of lead tungstate ($PbWO_4$) crystals with truncated pyramidal shape read out by photo-detectors. The ECAL surrounds the tracker and covers the range $|\eta| < 3.0$.

The use of lead tungstate is motivated by a number of factors. Its relatively short radiation length (0.89 cm) allows for the full energy deposition of electrons and photons in a smaller calorimeter. Its small Molière radius (2.2 cm) contributes to high spatial granularity. Its radiation hardness ensures useful scintillation after 10 years of LHC operation. Finally, the scintillation time of lead tungstate is on the order of the maximum LHC collision rate. There are, however, a couple of challenges that must be addressed when using lead tungstate scintillators. They have relatively low light output compared to many other crystals and the light output varies significantly with temperature. To maintain the desired energy resolution, the crystal temperature must remain stable to within 0.05°C.

The ECAL is separated into the barrel (EB) and endcap (EE) regions, which cover $|\eta| < 1.479$ and $1.479 < |\eta| < 3.0$, respectively. In the barrel, the crystals begin at $r = 1.29$ m, while in endcaps the crystals begin at $z = \pm 3.15$ m. To maximize spatial resolution due to energy sharing, the crystal faces have size sim-

ilar to the Molière radius. This sizing leads to 61200 crystals in the EB and 7324 crystals in each endcap. The crystals project approximately to the interaction point and are 22 to 23 cm long, corresponding to roughly 25 radiation lengths.

The light from each crystal is read out by one or two photodetectors attached to its back face. To cope with the extreme LHC conditions, these photodetectors are both fast and radiation hard. Additionally, they must function in the high magnetic field of the solenoid. The differing magnetic field and particle fluxes in the EB and EE necessitates the use of distinct photodetector technology in each. A pair of avalanche photodiodes (APDs) reads out each EB crystal, while one vacuum phototriode (VPT), which is a single gain-stage photomultiplier, reads out each EE crystal.

Every 25 ns, the signals from the photodetectors are shaped and amplified before being digitized by an ADC. In the case of EB, the signals from the two APDs per crystal are summed. The total transverse energy from 5×5 groups of crystals, called trigger towers, are sent to the Level-1 trigger system for each bunch crossing. When a Level-1 trigger is received, ten 25 ns samples for each channel are sent to the electronics in the service cavern and then passed to the central DAQ after a suppression algorithm is applied to reduce the data volume.

The expected energy resolution of the ECAL versus electron energy is shown in Fig. 3.5. Above 500 GeV, the resolution begins to degrade due to not all

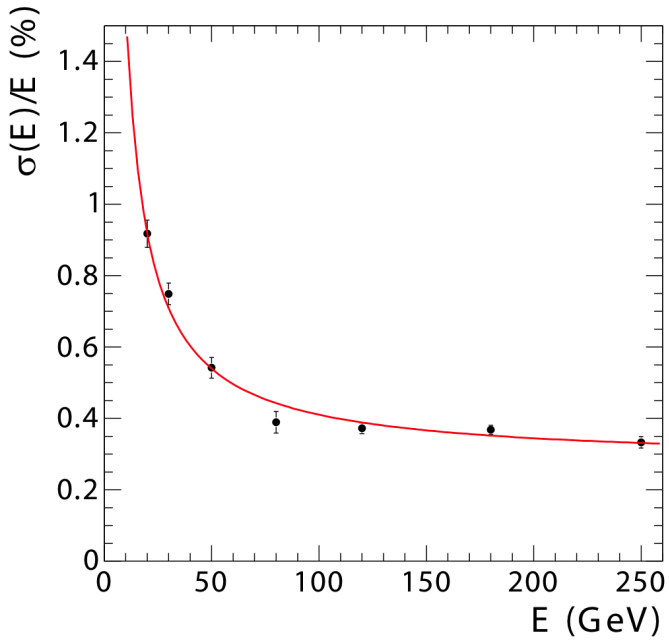

Figure 3.5: ECAL energy resolution as a function of electron energy as measured in test beam. Figure taken from Ref. [66].

of the energy being deposited before the shower exits the crystal. To maintain the resolution shown in this figure, the ECAL must be carefully calibrated to better than the percent level. One important and dynamic effect that must be calibrated is the dose-rate dependent loss of optical transmission during irradiation experienced by the crystals. This is monitored using the ECAL laser calibration system, which provides calibration data many times a second.

3.2.4 Hadronic Calorimeter

The hadronic calorimeter (HCAL) of CMS is designed to measure the energy of particles produced in the LHC collisions that interact through the strong force. This is done through a sampling technique utilizing alternating layers of absorber and scintilator. The HCAL and ECAL are quite complementary, because together they are able to measure the energy of the vast majority of the particles which emerge from LHC collisions. This ability is crucial to accurately infer the presence of neutrinos or other weakly interacting particles via momentum imbalance.

The HCAL is composed of 4 distinct sub-systems which enclose the ECAL and combine to give coverage up to $|\eta| = 5$. The 4 designs are necessary to accomodate the varying functions of the sub-systems as well as the differing amounts of radiation to which they are subjected. The majority of the volume of the HCAL is taken up by the hadronic barrel (HB) and hadronic endcap (HE) sub-systems. These are the two closest sub-systems to the collision point and are both contained within the solenoid. The furthest extent of coverage in $|\eta|$ is provided by the forward hadronic calorimeter (HF), which is considerably offset from the collision point along the beam axis compared to the rest of the HCAL. Finally, the outer hadronic calorimeter (HO) is positioned just outside the solenoid and is designed to collect residual energy from hadronic showers not fully contained in HB. Figure 3.6 shows the locations of the HCAL sub-systems within CMS.

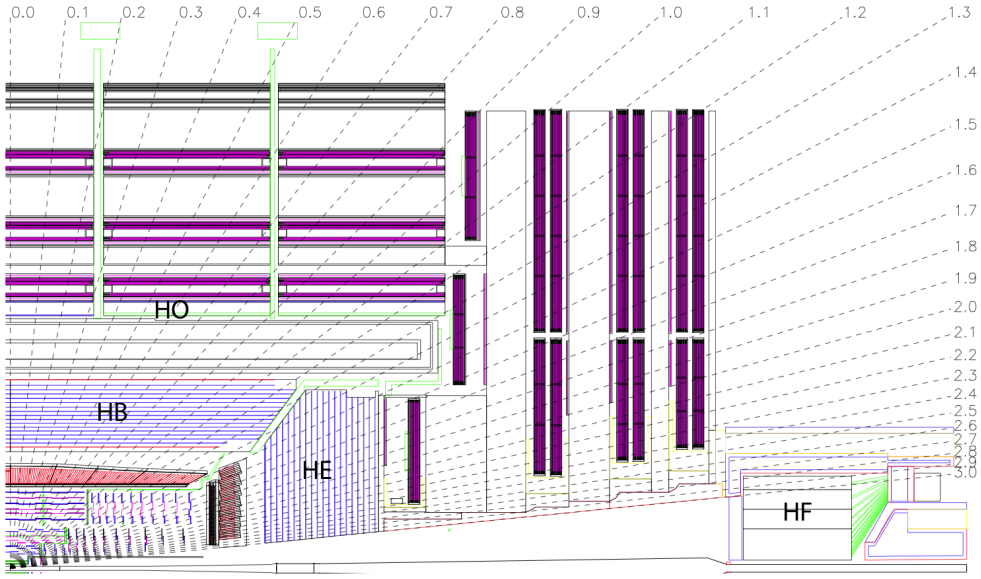

Figure 3.6: Longitudinal view of CMS indicating the positions of HB, HE, HO, and HF. The collision point is at the bottom left corner of the figure. The dashed lines emerging from the collision point correspond to different values of pseudorapidity. Figure taken from Ref. [66].

The HB has cylindrical geometry and covers $|\eta| < 1.3$, while the HE consists of an endcap inserted in each side of the solenoid, covering the pseudorapidity range $1.3 < |\eta| < 3$. The HB and HE are arranged with the aim of minimizing the gap between them in which particles could avoid detection and contribute to artificial momentum imbalance. The HB consists of 16 layers of plastic scintillator separated by steel and brass absorber plates. The HE consists of 17 layers of plastic scintillator separated by brass absorber plates, except near the HB-HE transition region, which has fewer layers. The light from each scintillator tile is collected by a wavelength-shifting (WLS) fiber, which is spliced to a clear fiber outside the

scintillator. The clear fiber brings the light to be read out by a hybrid photodiode (HPD). An HPD consists of multiple 20 mm^2 hexagonal silicon photodiode pixels held at a high voltage difference from a photocathode. HPDs are used in HB and HE due to their insensitivity to magnetic fields and large dynamical range. The HB and HE consist of towers with granularity of $\Delta\eta \times \Delta\phi = 0.087 \times 0.087$ for $|\eta| < 1.6$ and 0.17×0.17 for $|\eta| > 1.6$. The different scintillator layers within a tower are grouped into 1, 2, or 3 depths which are separately read out. The thickness of HB increases with $|\eta|$ from 5.4 nuclear interaction lengths (λ_I) at $\eta = 0$ to around 10 at $|\eta| = 1.3$. The HE has roughly constant thickness of 10 λ_I.

The HO calorimeter is positioned outside the solenoid and innermost iron section of the return yoke, which it effectively uses as an absorber, and covers the pseudorapidity range $|\eta| < 1.3$. Its main purpose is to collect additional energy from hadronic showers that escape HB, which is especially important at low $|\eta|$, where the HB thickness is smallest. The HO consists of only one scintillator layer, except for at the lowest $|\eta|$ range, in which a second scintillator is placed at lower radius between the yoke and solenoid. With the inclusion of HO, the thickness of the HCAL plus ECAL for $|\eta| < 3$ is increased to at least 11.8 λ_I, except in the barrel-endcap transition region. The HO towers match roughly those of the HB in position and coverage in η and ϕ. As in the HB and HE, the scintillator light is collected by WLS fibers and read out by HPDs.

The forward hadronic calorimeter (HF), covers the pseudorapidity region $3 < |\eta| < 5$ and begins 11.2 m from the collision point on either side. Because this region receives significantly higher radiation doses than the rest of the HCAL, HF has a distinct design to survive this harsh environment. Instead of plastic scintillator, much more radiation hard quartz fibers are used, which generate light via Cherenkov radiation. The quartz fibers are embedded in a steel absorber structure with thickness of roughly 10 λ_I and run parallel to the beam axis for either the entire length of the absorber, 165 cm, or the entire length except the first 22 cm closest to the collision point. The light yield in the different length fibers allows for discrimination of electrons and photons from hadrons because the former deposit a larger fraction of their energy in the first 22 cm. The fibers are bundled together to achieve granularity of $\Delta\eta \times \Delta\phi = 0.175 \times 0.175$ for the majority of HF. The light from these bundles is read out by photomultiplier tubes (PMTs), which are useable in the low magnetic field far away from the solenoid.

The electrical charge transduced in either an HPD or PMT in response to light from the scintillators or quartz fibers is integrated and read out by an ADC every 25ns. These readings are sent for every HCAL channel by optical link to HCAL Trigger/Read-out (HTR) boards in the service cavern. HTRs send trigger primitives, which consist of the transverse energy summed over the towers in a given η, ϕ range, to the Level-1 trigger system. In the event of a Level-1 trigger,

the HTRs send zero suppressed data as well as all the trigger primitives toward the central DAQ. In order to monitor the instantaneous luminosity in real-time, occupancy and energy deposit data from HF are sent from the HTRs to the HF luminosity system. Sufficiently small luminosity can be determined by the average fraction of empty towers, while larger luminosity must be extracted from its linear relationship with the average transverse energy deposited in HF towers.

Upgrade of HO

The potential benefits of HO have been limited so far by the significant rate at which its HPDs generate large amounts of noise. This spurious noise can erroneously indicate the presence of large transverse momentum imbalance, which is quite detrimental to many physics analyses. Smaller magnitude but more frequent noise from the HPDs also degrades the energy resolution. The HPDs in HO are significantly noisier than those in HB and HE due to the smaller, less uniform solenoid return field. To alleviate these problems and reach the full potential of the HO, it is necessary to replace the HPDs with some other read-out system. That project was part of this thesis work and is described below.

The low-noise photo-detection technology that will be used to upgrade HO is that of silicon photomultipliers (SiPMs). A SiPM consists of an array of many individual silicon avalanche photodiodes, each operated in Geiger mode with a

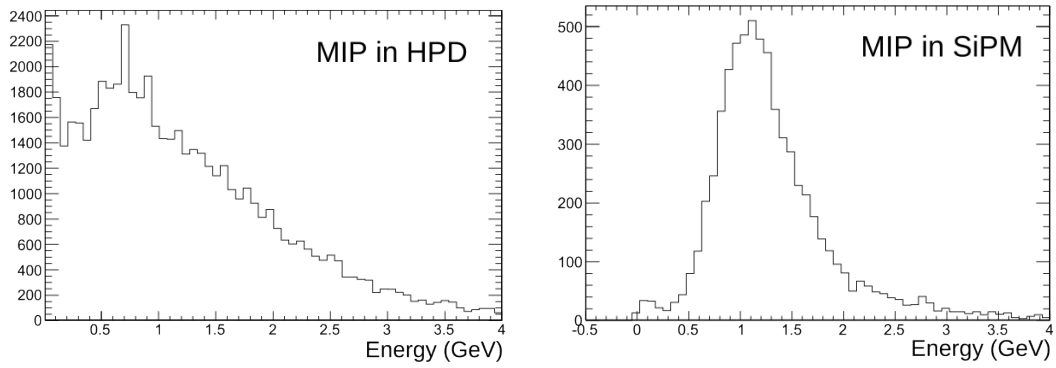

(a) (b)

Figure 3.7: HO MIP signal for an (a) HPD and (b) SiPM. This SiPM can clearly differentiate a MIP from noise due to its much better signal to noise than the HPD. Figure taken from Ref. [68].

gain typically of 10^5 to 10^6. SiPMs have relatively small dark current, on the order of a few tens of nanoamperes for the SiPMs and operating conditions to be used in HO. The breakdown of each pixel is passively quenched via a resistor. SiPMs are practically insensitive to magnetic fields, and should not be affected by the return field of the solenoid. Figure 3.7 shows the signal from a minimum ionizing particle (MIP) that traverses an HO scintillator, as read out by HPDs and SiPMs. Thanks to their much better signal to noise, the SiPMs can clearly distinguish the MIP signal. This feature will give HO the potential to aid in muon identification.

The SiPMs to be installed in HO are 3×3 mm^2 with 3600 square pixels of size 50×50 μm^2. This number of pixels is sufficient to cover the dynamic range of HO,

which is around 2500 photo-electrons. They have sub-nanosecond timing jitter as well as signal decay and recovery time on the order of 10 ns, which is sufficient to handle the occupancies in HO combined with the 25 ns bunch spacing of the LHC. The bias voltages of the SiPMs are around 70 V, which eliminates the need for the high voltage power utilized by the HPDs. For wavelengths of 500 nm, which is what is delivered from the scintillator via WLS fibers, the SiPMs have a quantum efficiency of $25 - 30\%$, which is nearly twice that of HPDs.

One complication with using SiPMs is their non-negligible dependence of gain on temperature. This dependence is a roughly $5 - 10\%$ decrease in the gain per $1°$C increase in temperature. To ensure stability of the SiPM response to the few percent level, the temperature must be regulated to within a fraction of a degree. This is done via a Peltier cooling element attached to the back of the board on which the SiPMs are mounted. A feedback loop utilizing a temperature sensor at the center of the SiPM mounting board will control the temperature by adjusting the voltage to the Peltier.

The total amount of hardware that must be replaced to transition from HPDs to SiPMs in HO has been carefully minimized to reduce the total amount of work and potential for problems. This is achieved by designing the boards on which the SiPMs are mounted to mimic the layout of the HPD boards. Figure 3.8 shows the front and back of the board on which the SiPMs are mounted. The 18 SiPMs

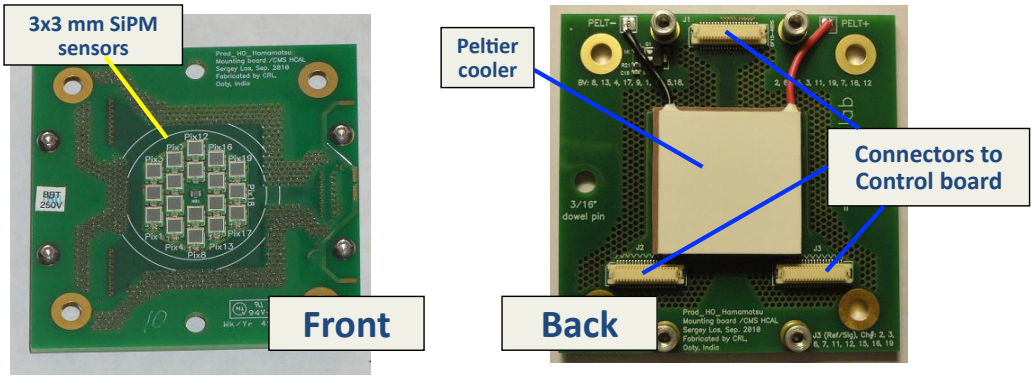

Figure 3.8: Photographs of the front and back of an HO SiPM mounting board. In the center of the 18 SiPMs is a small thermistor used to monitor the operating temperature of the SiPMs. Figure taken from Ref. [69].

on this board are arranged in the same configuration as the HPD pixels. Because of this design, the HPD can simply be replaced by the SiPM mounting board packaged with a control board and a board to generate the bias voltages. The control board attached to the SiPM mounting board is responsible for regulating the SiPM bias voltages, reading out their leakage currents, and supplying the Peltier cooler with power. The bias voltages are generated by a separate board from a 6.5 V low voltage input.

In order to utilize the full dynamic range of a SiPM, the incoming photons must be spread out across its entire active surface. If instead the photons are concentrated over a small area of the SiPM, only the pixels occupying that area will avalanche and the signal will be reduced. To avoid this effect, light mixers are used to spread the light from the scintillators more uniformly across the SiPMs.

Light mixers are only used for the SiPMs in the most central return yoke segment, as this is where the thickness of the calorimeter is lowest and consequently the signals in HO will be largest.

Before a SiPM can be installed in HO, it must undergo a rigorous quality control (QC) assessment to ensure optimal functionality of the detector. Not only must the SiPMs undergo QC, but so too must all of the components that will be installed, most importantly the Peltier cooler, control board, and bias voltage board. The QC is done in a multi-step process, beginning with the measurement of the important properties of each SiPM by the manufacturer and the testing of the different boards at their production sites. For each SiPM mounting board, the final grouping of associated boards is assembled at CERN before undergoing QC in a test stand. Then, when the old HPDs are removed from HO and replaced with SiPMs, the resulting hardware is briefly tested in its final configuration in the test-stand before being installed into CMS. The final step of the QC is to make sure the SiPMs function properly after installation into CMS.

To determine the normal range of the stability and operational parameters of the SiPMs in the final system configuration, the test-stand mentioned above is utilized. One such set of operational parameters comes from the analysis of the SiPM signals in the absence of light, which will be referred to herein as pedestal events. This analysis relies upon the two key properties of SiPMs. First, is the

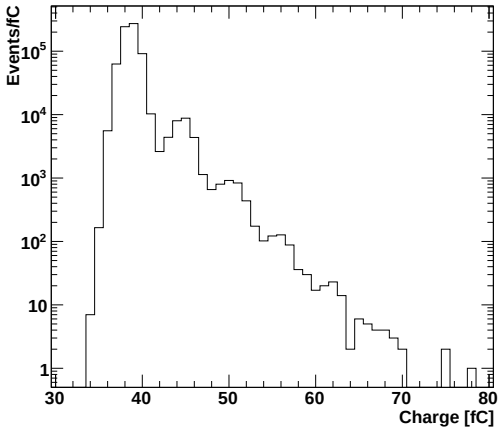

Figure 3.9: Charge distribution in pedestal events for one SiPM. Each pedestal event integrates the charge over a 100 ns window. Note that there is an overall offset of charge introduced by the ADC which is much larger than the SiPM leakage current.

fact that individual SiPM pixels will thermally avalanche with non-negligible rate. Second is that SiPMs can count small numbers of photons, or equivalently, resolve small numbers of pixel avalanches. These features are apparent in Fig. 3.9, which shows the distribution of charge output by a SiPM in many pedestal events. The highest peak comes from events in which no pixels avalanched, while the second highest peak comes from events in which exactly 1 pixel avalanched. Subsequent peaks have larger numbers of pixels which avalanched.

These pedestal charge distributions are fit to extract important operational parameters of the SiPMs. In particular, Gaussian distributions are used to fit the 0, 1 and 2 avalanche peaks, an example of which is shown in Fig. 3.10. For

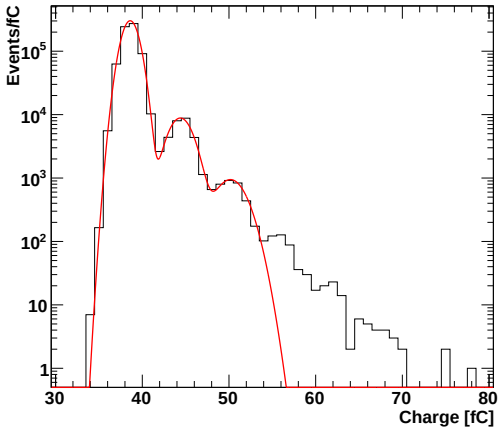

Figure 3.10: Charge distribution in pedestal events for one SiPM with overlaid fit. Only the 0, 1, and 2 avalanche peaks are included in the fit range. From the fit, various operational parameters of the SiPM are extracted.

simplicity and robustness, no higher order peaks are included in the fit range. The distance between consecutive peaks is determined by the fit and gives the gain of the SiPMs. This distance is constrained in the fit to be the same between both sets of consecutive peaks. The relative normalization of the peaks is treated as a Poisson distribution, but the normalization of the 2 avalanche peak is allowed to float for reasons which will be described below. The mean of the Poisson distribution indicates the avalanche rate of the SiPM. If there is no significant light leak in the system, then this is equivalent to the thermal avalanche rate. A thermal avalanche rate of a few hundred kilo-Hertz is typical.

The level of normalization enhancement of the 2 avalanche peak compared to what is expected by the fitted Poisson distribution gives additional interest-

ing information. This enhancement occurs due to optical cross-talk, in which a photon emitted during an avalanche in one pixel triggers an avalanche in a neighboring pixel in the same SiPM, as well as afterpulsing in which charge trapped in the silicon from the original avalanche eventually becomes free and causes another avalanche in the same pixel. Because the test-stand does not have the time resolution to differentiate these effects, their combination will be referred to as cross-talk from here on.

To quantify this effect, the cross-talk rate is defined as the probability that an avalanche in one pixel causes an additional avalanche in the same SiPM in the same event. The following derivation gives an approximate formula for the cross-talk rate using the parameters of the fit to the pedestal charge distribution. For a given pedestal distribution, let N_1^{ideal} be the number of events with exactly 1 avalanche in the idealized situation with no cross-talk. Then $N_1^{\text{ideal}} = N_1^{\text{obs}}/(1 - R_{\text{xtalk}})$, where N_1^{obs} is the observed number of events with exactly 1 avalanche and R_{xtalk} is the cross-talk rate. Assuming that the cross-talk rate is small and ignoring higher order corrections, the observed number of events with exactly 2 avalanches should be $N_2^{\text{obs}} \approx N_1^{\text{ideal}} \left(R_{12}^{\text{ideal}} + R_{\text{xtalk}}\right)$, where R_{12}^{ideal} is the ratio of 2 avalanche to 1 avalanche events, ignoring cross-talk effects. Substituting and solving for the cross-talk rate gives

$$R_{\text{xtalk}} \approx \frac{N_2^{\text{obs}}/N_1^{\text{obs}} - R_{12}^{\text{ideal}}}{1 + N_2^{\text{obs}}/N_1^{\text{obs}}}. \tag{3.1}$$

The value of R_{12}^{ideal} is taken from the fitted mean number of avalanches divided by two. The fitted mean is biased somewhat by the presence of cross-talk, but only by a relative amount equal to the cross-talk rate. The value of $N_2^{\text{obs}}/N_1^{\text{obs}}$ is taken to be R_{12}^{ideal} times the fitted multiplicative enhancement of the normalization of the 2 avalanche peak. The uncertainties, and their correlation, on the fitted parameters are propagated in the calculation of the cross-talk rate.

The gain, cross-talk rate, and avalanche rate as determined by the pedestal fits are shown in Fig. 3.11 for nearly all of the SiPMs that will be installed in HO. These global distribution plots indicate the normal range of these parameters for properly functioning SiPMs. Outliers are scrutinized heavily and potentially rejected from the installation depending on the results of other QC tests.

Additionally, SiPM bias voltage scans are performed so that the gain at each scan point can be determined by fitting the corresponding pedestal charge distribution. The result is a gain vs voltage distribution which is fit with a line, as illustrated in Fig. 3.12. The slope of the fitted line gives the dependence of the gain on the bias voltage and the extrapolation to gain of 0 yields the breakdown voltage of the SiPM. The slope and breakdown voltage for nearly all SiPMs to be used in the HO upgrade is shown in Fig. 3.13. Using SiPM signals in the presence of LED light, different methods are used to measure the breakdown voltage and gain. This complementarity yields valuable information about the systematic bi-

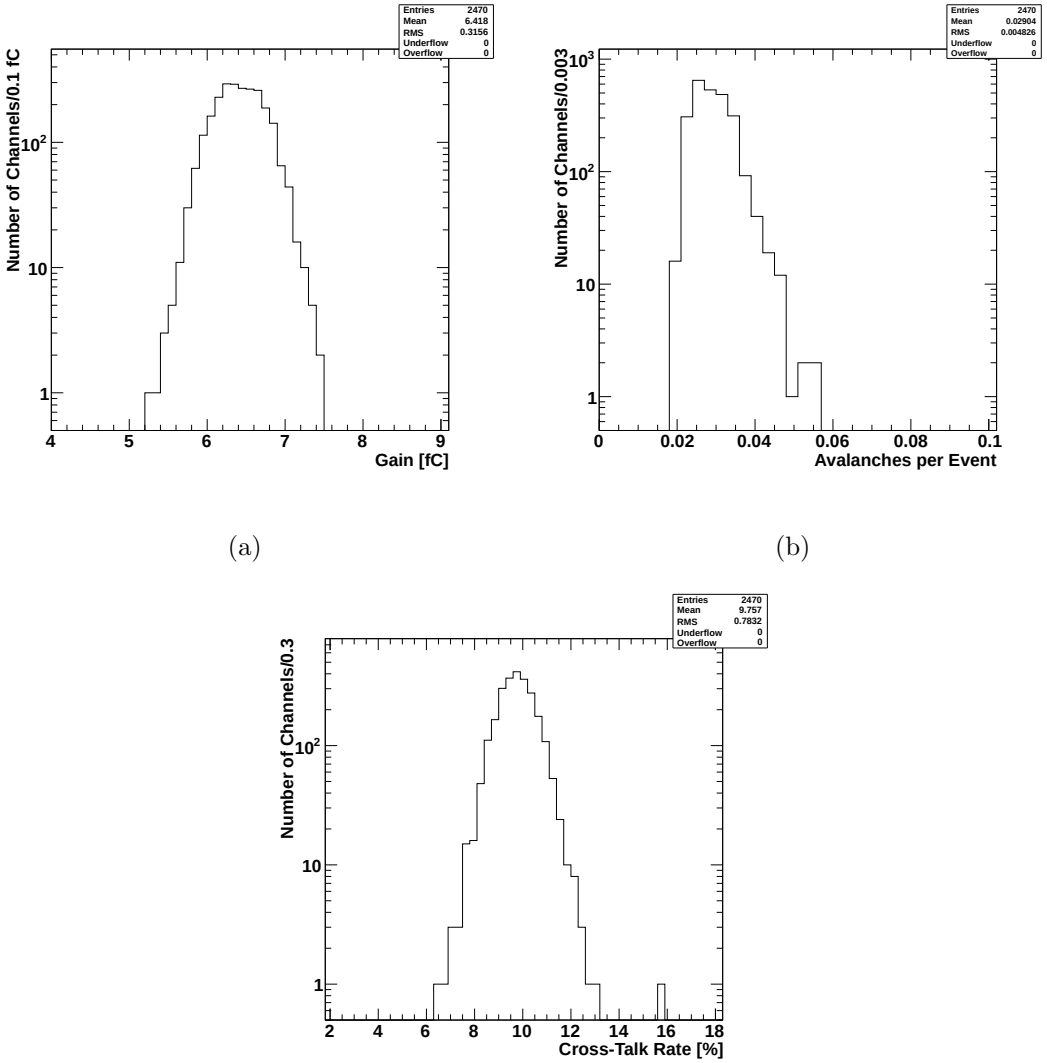

Figure 3.11: Distribution of (a) gain, (b) average number of avalanches per event, and (c) cross-talk rate for nearly all SiPMs to be installed in HO as measured from the pedestal fit analysis.

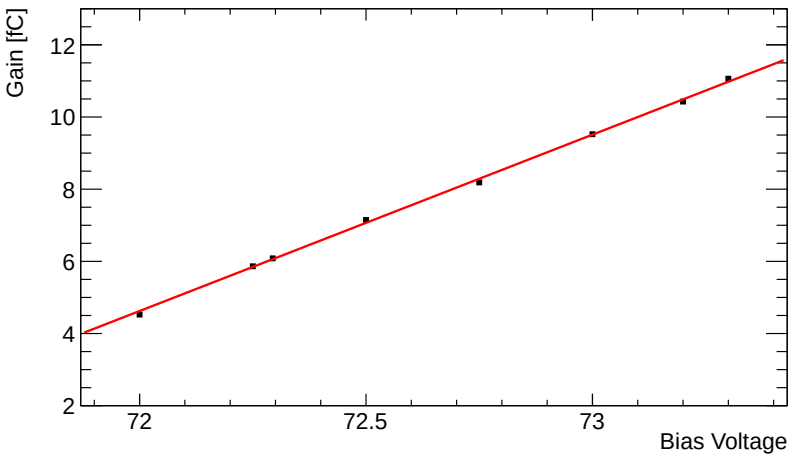

Figure 3.12: Example gain vs bias voltage distribution for one SiPM with overlaid linear fit. The gain at each bias voltage is determined from a fit to the pedestal charge distribution at that bias voltage.

ases of each method as well as greater confidence in the result when the different methods agree.

The analysis of the pedestal charge distributions described here is but one of many QC tests performed on the SiPMs before they can be installed in CMS. Other crucial tests are of the SiPM response stability over time, the rate of significant amounts of spurious noise, and the effectiveness of the Peltier cooling element. The large majority of SiPMs and corresponding electronics exhibited no problematic behavior in the QC tests, and were consequently certified for installation. This installation is now complete, as all of the HPDs in HO have been replaced by SiPMs during the current LHC long shut-down period.

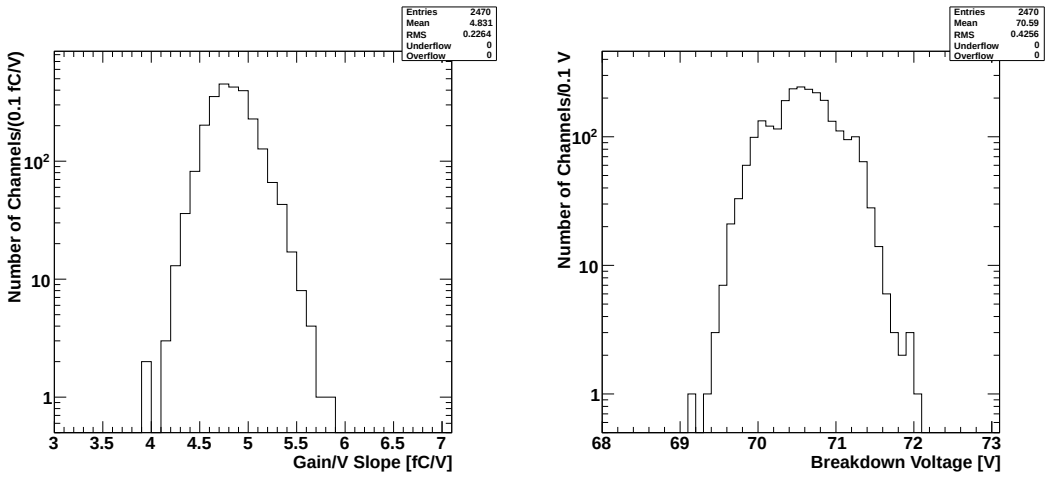

(a) (b)

Figure 3.13: Distribution of (a) gain vs voltage slope and (b) breakdown voltage for nearly all SiPMs to be installed in HO as measured from the pedestal fit analysis applied to a bias voltage scan.

3.2.5 Muon System

As indicated by its name, the design of the Compact Muon Solenoid experiment places a heavy emphasis on the detection of muons. The muon system of CMS provides the ability to trigger on muons at Level-1, and in conjunction with the tracker ensures high detection efficiency and excellent momentum resolution for muons. It is housed within the return yoke of the solenoid, which simultaneously provides a magnetic field to bend the trajectories of muons for momentum measurement and as an absorber to prevent hadrons from reaching the muon system. The muon system consists of 3 distinct sub-systems, the drift

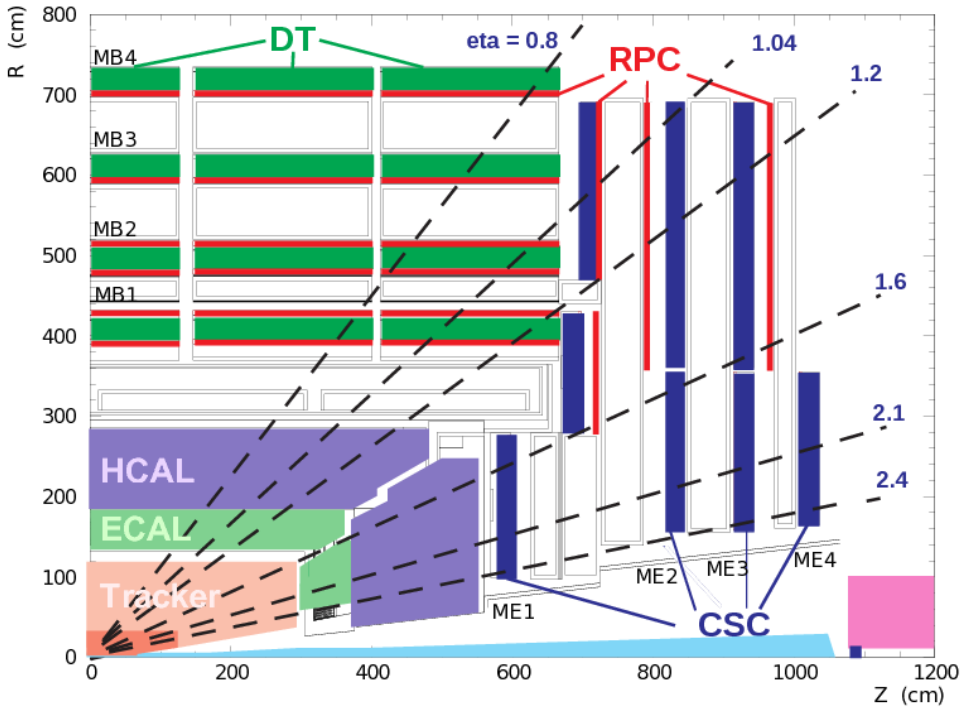

Figure 3.14: Longitudinal view of CMS indicating the positions of the DT, CSC, and RPC muon sub-systems. The collision point is at the bottom left corner of the figure. The dashed lines emerging from the collision point correspond to different values of pseudorapidity. Figure taken from Ref. [70].

tubes (DT), cathode strip chambers (CSC), and resistive plate chambers (RPC). The positions of these sub-systems within CMS can be seen in Fig. 3.14. In order to achieve the optimal momentum resolution of the muon system, it is necessary that the muon chambers are aligned amongst themselves and with the inner tracker to $\mathcal{O}(100\ \mu\text{m})$ in the transverse plane. This alignment is performed using both muon tracks measured by the detector and an optical alignment system.

The DT sub-system is located in the barrel region and extends to $|\eta| < 1.2$. It consists of 4 stations at increasing radius, with each station being sub-divided into chambers separated by the return yoke. For the innermost 3 stations, a chamber consists of 3 superlayers (SL), which in turn consist of 4 layers of rectangular drift cells. Two of the superlayers have cells running parallel to the beam axis in order to provide a measurement in the $r\phi$ plane, while the third superlayer has its cells arranged perpendicularly to provide a measurement in the rz plane. The outermost station only contains 2 superlayers, with cells arranged parallel to the beam axis. A SL has time resolution on the order of nanoseconds, which allows the bunch crossing from which a muon emerged to be efficiently determined. An individual cell has dimensions 13 mm $\times$ 42 mm $\times$ 2.4 m and contains a wire, electrode strips, and cathode strips running along its length. The geometry combined with the nominal 85% Ar, 15% CO_2 gas mixture results in a linear relationship between drift time and drift length. A signal produced in a DT cell is amplified, discriminated, and then time digitized by electronics all within the DT chamber. The DT electronics combines the individual cell signals to provide track candidate information to the Level-1 Trigger.

The CSC sub-system is located in the endcap region of CMS and extends from $0.9 < |\eta| < 2.4$. The CSC design is necessarily different than in the DT, due to the higher signal and background rates as well as the larger and less uniform

magnetic field. It consists of 4 stations in each endcap, subdivided into trapezoidal chambers perpendicular to the beam line. A chamber is composed of 6 layers of anode wires alternating with 7 layers of cathode strips. The strips run radially to provide a measurement of ϕ while the wires run perpendicularly to provide a measurement of η. The wires serve as proportional counters with avalanches which induce charge on the nearby strips. A chamber has time resolution of less than 5 ns, which allows the bunch crossing from which a muon emerged to be efficiently determined. The chambers utilize a 40% Ar, 50% CO_2, and 10% CF_4 gas mixture at atmospheric pressure. For every bunch crossing, special electronics searches for patterns consistent with muon tracks separately in the anode and cathode layers of a chamber. These patterns are then combined to form 3-dimensional track candidates, which are sent to the Level-1 Trigger. To reduce the data rate from the CSCs, data from a chamber is only sent to the central DAQ if there is a muon track candidate with timing consistent with a Level-1 trigger.

The RPC sub-system extends to $|\eta| < 1.6$ and consequently overlaps all of the DTs and much of the CSCs. The RPC system can independently reconstruct muon tracks with excellent time resolution, 1 ns, but worse position resolution than the DTs and CSCs. It consists of 4 stations in the barrel and 3 stations in the endcaps. The innermost two stations in the barrel have two RPC chambers while the outer two stations each have one. The three stations in the endcaps

border the innermost CSC chambers and have one chamber each. A chamber has a parallel-plate structure with read-out strips between the plates to provide two gaps operated in avalanche mode. For the most precise measurement of ϕ, the strips in the barrel run parallel to the beam line and those in the endcap run radially. Each chamber is filled with a gas mixture of 96.2% $C_2H_2F_4$, 3.5% iC_4H_{10}, and 0.3% SF_6. The signals from the strips are amplified and discriminated before being passed to the Level-1 trigger and in the case of a trigger, the central DAQ.

3.2.6 Trigger

Given the vast number of detector channels in CMS, each collision event that is saved requires a significant amount of bandwidth to transmit, memory to store, and time to reconstruct. These constraints require that the overall rate at which events are saved is less than around 1000 Hz. To achieve this rate without throwing out the most interesting events, CMS relies on a two-stage trigger system. The Level-1 trigger processes each collision and reduces the rate to less than 100 kHz and feeds the High Level Trigger stage, which reduces the rate to less than 1000 Hz.

The L1 Trigger processes every collision using data from the ECAL, HCAL and Muon system with coarse granularity to reduce the bandwidth of data that must be transmitted. The maximum latency for a trigger decision on an event is 3.2 μs. Using the ECAL and HCAL data, electron/photon candidates and jets

are reconstructed. Candidates for jets from hadronic τ decays are identified by their narrow width. Additionally, the number of jets, total transverse energy, missing transverse energy, and scalar jet transverse energy sum are computed. Using data from all 3 Muon sub-systems, the transverse momentum, charge, η, ϕ, and quality of muon candidates are determined. Extrapolating the track back to the calorimeter, the energy deposited in the ECAL and HCAL is compared with a threshold to determine if the muon candidate is isolated. The above trigger objects and global quantities are used to determine whether an event should be accepted or rejected.

Upon a Level-1 accept, the full data from an event is made available to the HLT so that more complex trigger algorithms can be computed. Unlike the Level-1 trigger, which uses custom electronics, the HLT uses commercially available processors and is software based. This allows the HLT algorithms to be extremely flexible and easily altered. To maximize the amount of interesting events that can be saved, the HLT trigger objects should match the offline reconstructed objects as closely as possible. However, the finite number of processors in the HLT means that the processing time per event must be limited, and hence the computationally intensive offline reconstruction algorithms can only be approximated. Upon passing the HLT, the full data from an event is stored for subsequent offline reconstruction and analysis.

Chapter 4

Event Reconstruction

Before any meaningful physics analysis of the CMS data can take place, the raw signals from the detector must be used to reconstruct the particles produced by the LHC collisions. It is only with the reconstructed objects and global event quantities that the properties of an event can be fully evaluated. The standard physics objects that CMS is able to reconstruct are electrons, photons, muons, taus, and jets. The important global event quantities for this analysis are the missing transverse momentum ($\not\!\!E_{\mathrm{T}}$), which is the negative vector sum of the momenta of all reconstructed particles in the collision, and the scalar sum of all jet p_T (H_T). This chapter briefly describes the reconstruction of the objects and quantities used in this analysis. Photons and taus are not used and therefore are not discussed here. Information about the reconstruction of these objects can be found in Refs. [71, 72].

4.1 Tracks and Primary Vertices

All of the physics objects used in this analysis are reconstructed, at least in part, using information from the CMS tracker. To measure the trajectory of a charged particle [73], hits in the pixel tracker are used to seed the track finding algorithm [74]. From the seed, the track reconstruction proceeds via combinatorial Kalman filter pattern recognition [75]. Due to the 3.8 T magnetic field, charged particles follow a helical path with radius of curvature determined by their transverse momentum. The effects of energy loss of the particle in the tracker material and multiple scattering are also accounted for in the pattern recognition.

Nearly all inelastic pp collisions produce charged particles. If at least a few of the charged particles produced in such a collision are high enough p_T to produce tracks measured by the tracker, the location of the collision can be identified. A clustering followed by a fitting algorithm [73, 76] is performed using the set of all tracks to find the 3-dimensional collision locations, called primary vertices (PVs). A vertex corresponds to the location from which multiple tracks emerge.

To ensure that a reconstructed PV corresponds to a real collision, the following quality criteria are utilized. A PV that passes each of these requirements is considered good.

- The number of degrees of freedom from the tracks in the vertex fit must be greater than 4.
- The displacement from the origin in the transverse plane must be less than 2 cm.
- The displacement from the origin along the beam direction must be less than 24 cm.

The good primary vertex with the largest sum of the transverse momentum squared of its associated tracks is considered the leading vertex of the event and assumed to be the origin of the interesting physics objects.

Due to the high instantaneous luminosity provided by the LHC, there are on average roughly 20 inelastic pp collisions per bunch crossing in the 2012 CMS pp dataset. These overlapping collisions, referred to as pile-up (PU), generally produce fewer and lower energy particles than the collisions which are interesting for physics studies. However, the large number of PU collisions that occur in the same bunch crossing with an interesting collision can introduce non-negligible bias in the reconstructed physics objects if care is not taken.

4.2 Jets

Jets are reconstructed using the anti-k_t algorithm [77] with distance parameter $R = 0.5$ in y, ϕ coordinates. This algorithm utilizes the technique of sequential recombination at the particle level with distance measure proportional to inverse momentum squared to obtain results that are both collinear and infrared safe. In other words, the jet boundaries are sensitive to the distribution of higher energy, collinear, radiation in a parton shower, but not lower energy, infrared, radiation. The infrared safety is also helpful in minimizing the effects of unrelated low energy radiation from pileup interactions.

The particle constituents supplied to the jet clustering are supplied by the Particle Flow (PF) event reconstruction algorithm [78, 79]. This algorithm attempts to identify and reconstruct all the final-state particles in an event. This consists of electrons, photons, muons, charged hadrons, and neutral hadrons. The full information of all the CMS sub-detectors is used in a coordinated way by the PF algorithm. One important consequence of this is that tracking information is used to precisely determine the momentum of charged hadrons. Because charged hadrons generally carry much of the energy in a jet, the PF-based jet energy resolution is improved compared to that of traditional jet reconstruction based solely on calorimetric information.

It is desirable that the measured energy of a jet match the true energy of the final-state particles which it encompasses. Therefore, it is necessary to correct the raw measured energy of jets to account for shifts and non-uniformities in the energy scale [80]. Such jet energy corrections (JEC) are factorized into distinct components and applied sequentially to the raw jet energy. The first level of correction removes the contribution to the jet energy from particles produced in unrelated PU collisions which overlap with the jet in η and ϕ. This is done on a jet-by-jet basis for each event using each jet's area in rapidity-ϕ space combined with the median energy density in the event [81], while accounting for the non-uniform response of the detector in η. The next level of correction is derived from simulation and makes the jet response uniform versus η. This is followed by another simulation-based correction to achieve the correct energy scale as a function of jet p_T. The final correction, applied only to data, is relatively small and removes residual data-MC differences. The uncertainty on these corrections comes from a number of sources, illustrated for various jet p_T and η in Fig. 4.1. The uncertainty increases sharply at low p_T because of the relatively large contribution from PU and above $|\eta| = 2$ due to loss of acceptance in the tracker.

To minimize the number of selected jets which arise due to detector noise or other background sources such as mis-reconstructed electrons, the following minimal set of selection requirements are applied.

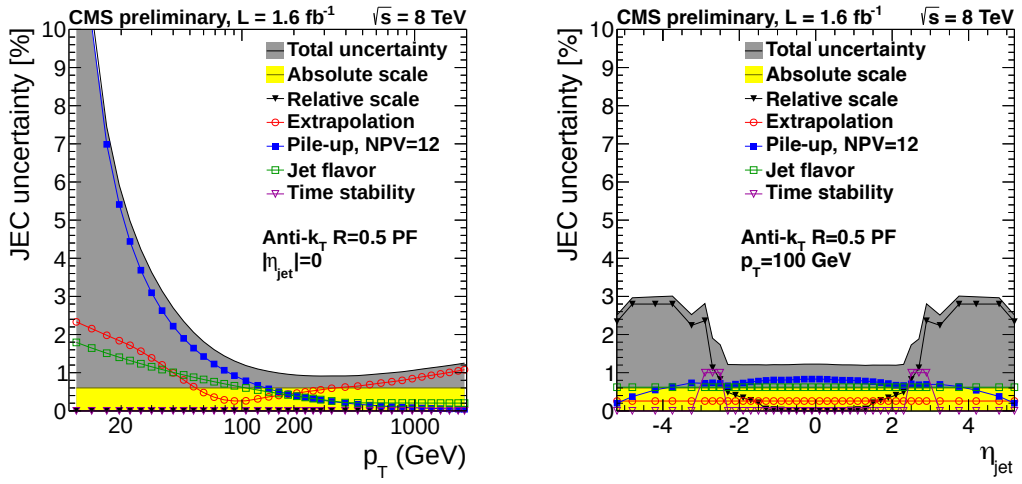

(a) (b)

Figure 4.1: JEC uncertainty in percent as (a) a function of jet p_T and (b) a function of jet η. The various sub-components of the uncertainty are shown individually. Figure taken from Ref. [82].

- Jets must have $p_T > 40$ GeV.
- Jets must have $|\eta| < 2.4$, to remain within the tracker acceptance and take full advantage of the PF reconstruction algorithm.
- Jets must contain at least two particles, at least one of which is a charged hadron or electron.
- The neutral hadron energy fraction must be less than 99%.
- The neutral electromagnetic energy fraction must be less than 99%.
- The charged electromagnetic energy fraction must be less than 99%.

- The charged hadron energy fraction must be non-zero.

4.2.1 b-quark Jet Identification

Jets produced by b-quark hadronization (b jets) have unique properties compared to other jets due to the relatively large b-quark mass and lifetime. Of all the particles produced in the b jet, the hadron containing the original b quark will have a greater than average fraction of the total momentum and be relatively long-lived ($\tau \approx 1.5$ ps). These properties of b jets can be exploited to discriminate between them and jets from other sources. When a jet has been identified as a b jet, it is said to be b tagged.

The particular b-tagging discriminator, or b tagger, used in this analysis is the Combined Secondary Vertex (CSV) algorithm [83]. This tagger utilizes a likelihood ratio built from variables from the individual tracks within a jet as well as from a secondary vertex within that jet, if one is found. The tracking variables are the number of tracks within the jet and their 3-dimensional impact parameter significances, i.e., measured impact parameter divided by its uncertainty, with respect to the associated primary vertex. A secondary vertex is only associated with a jet if it is within a $\Delta R < 0.5$ cone of the jet axis as well as distinguishably separated from the primary vertex associated with that jet. The relevant secondary vertex variables are its separation from the associated primary vertex divided by

its uncertainty in the transverse plane, mass, number of tracks, fractional energy of its tracks compared to all tracks in the jet, η of its tracks relative to the jet axis, and 2-dimensional impact parameters of its tracks. In the case that no secondary vertex is associated with the jet, only the tracking variables are used.

This analysis uses the medium working point of the CSV tagger (CSVM). The b-tag efficiencies and mistag rates at this working point are shown in Fig 4.2 separately for simulated multi-jet QCD and $t\bar{t}$ pair production events. The CSVM working point corresponds to values of the CSV discriminator above 0.679, and is intended to result in a light flavor mistag probability of roughly 1%. Light flavor jets are defined to come from u, d, and s-quarks as well as gluons. The charm-quark mistag probability is higher than that for light flavor jets due to the significantly higher mass of the charm quark. At high jet p_T, the products of the jet are more boosted and the tracks curve less due to the magnetic field, which makes impact parameter and secondary vertex measurements less precise, thus reducing the b-tag efficiency and increasing the light flavor mistag rate. At $|\eta|$ of around 2.4, the limited acceptance of the tracker also reduces the b-tag efficiency.

While the efficiency and mistag probability in simulation are similar to that in data, they are not identical. Therefore, the simulated b-tag efficiency is corrected by a scale factor SF_b which is the ratio of the efficiency in data to simulation. Similarly the charm and light flavor mistag rates are corrected by scale factors

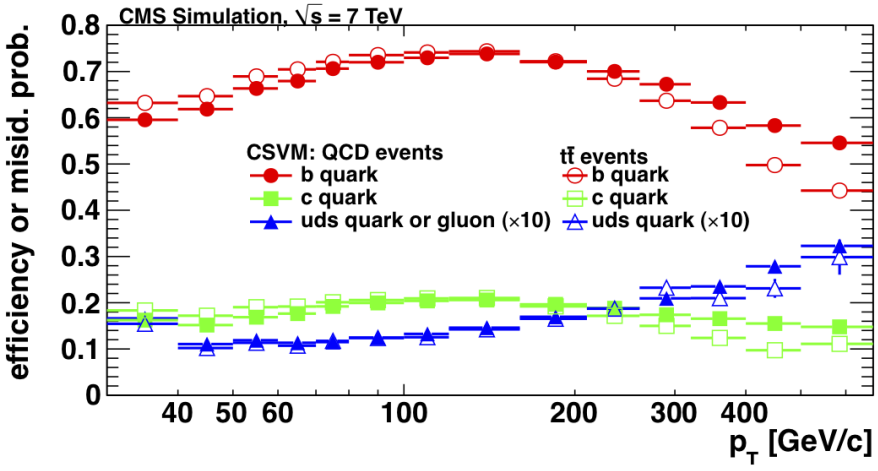

(a)

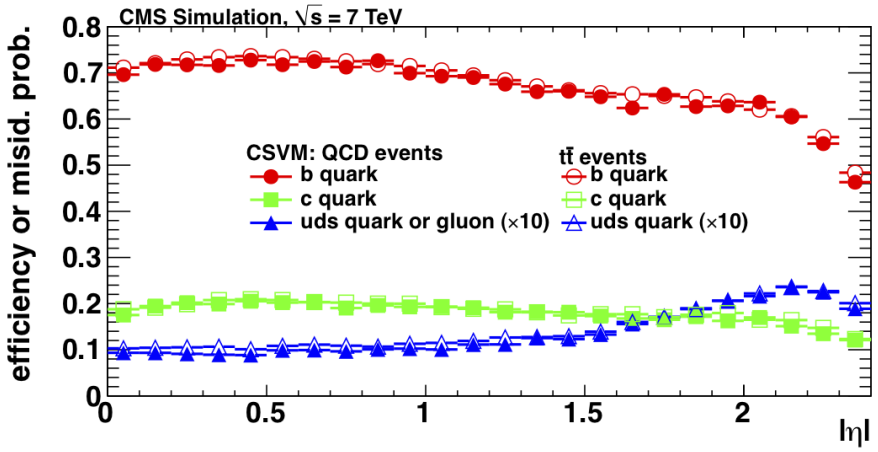

(b)

Figure 4.2: The b-tag efficiencies and mistag rates at the CSVM working point in $\sqrt{s} = 7$ TeV simulation versus (a) jet p_T and (b) jet $|\eta|$. These quantities are shown separately for multi-jet QCD and $t\bar{t}$ pair production events and are similar to those at $\sqrt{s} = 8$ TeV despite the higher energy and PU. Note that the light flavor mistag probability has been increased by a factor of 10 so that it is clearly visible. Figure taken from Ref. [83].

SF_c and SF_{lf}, which are the ratio of the respective mistag rates in data and simulation. Due to the variation of efficiency and mistag probability with respect to jet p_T and η, the scale factors are binned in each of these variables. In deriving and applying these scale factors, the jet flavors in simulation are identified using generator-level information.

4.3 Missing Transverse Momentum

The $\not\!\!E_{\mathrm{T}}$ is computed using the particle candidates reconstructed by the PF algorithm [84]. Assuming perfect measurement, a large $\not\!\!E_{\mathrm{T}}$ value indicates the presence of one or more weakly interacting particles in the final state, such as neutrinos or LSPs. The measured $\vec{\not\!\!E}_{\mathrm{T}}$ is equal to the negative vector sum of the transverse momentum of all PF candidates, with a couple of corrections [85]. The larger of the two corrections comes from applying the JEC to jets with $p_T >$ 10 GeV, i.e.,

$$\vec{\not\!\!E}_{\mathrm{T}}^{\mathrm{corr}} = \vec{\not\!\!E}_{\mathrm{T}} - \sum_{\mathrm{jets}} \left(\vec{p}_{T,\mathrm{jet}}^{\,\mathrm{corr}} - \vec{p}_{T,\mathrm{jet}}\right). \tag{4.1}$$

The other correction is designed to remove a ϕ-dependent asymmetry in the $\vec{\not\!\!E}_{\mathrm{T}}$. This correction depends linearly on the number of reconstructed PU vertices in the event and typically changes the $\not\!\!E_{\mathrm{T}}$ by less than 10 GeV, which is small compared to the scale relevant for this analysis.

Unfortunately, detector mis-reconstruction effects can also give rise to large values of $\not\!\!E_{\mathrm{T}}$, i.e., artificial $\not\!\!E_{\mathrm{T}}$. These effects are rare, but the large number of events collected by the LHC means they will affect a significant number of events. In order to reliably and effectively utilize a data sample with large $\not\!\!E_{\mathrm{T}}$ for physics, it is necessary to efficiently reject events which have large artificial $\not\!\!E_{\mathrm{T}}$. Various sources of artificial $\not\!\!E_{\mathrm{T}}$ in CMS and the filters used to reject them are described in Ref. [85]. Figure 4.3 shows the drastic change in the high tail of the $\not\!\!E_{\mathrm{T}}$ distribution in data after cleaning is applied. Without this cleaning, SUSY events with high $\not\!\!E_{\mathrm{T}}$ would be hopelessly outnumbered by background.

4.4 Electrons

Electrons in CMS are reconstructed using measurements from the ECAL and tracker. Each sub-detector provides complementary measurements of the energy and momentum of an electron, which are combined by the reconstruction algorithms. The electron reconstruction used in this analysis can proceed in two distinct ways, namely via tracker-driven and ECAL-driven seeding.

This analysis selects electron candidates from the ECAL-driven seeding algorithm [86]. The first step of this algorithm is to find an ECAL "supercluster" seed for the electron. A supercluster is a group of energy deposits in nearby ECAL

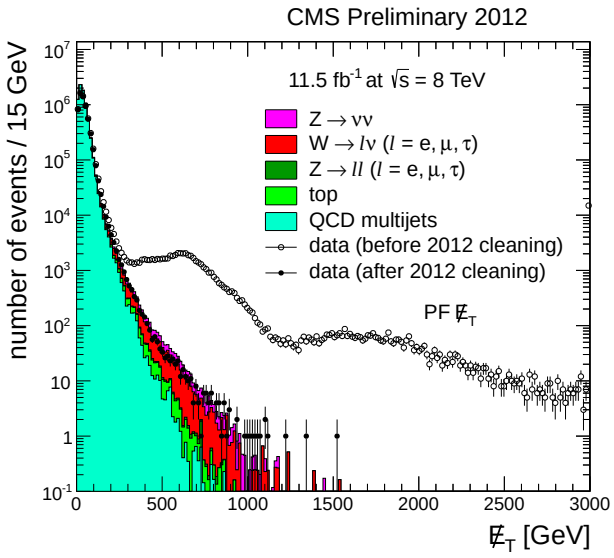

Figure 4.3: The $\not\!\!E_{\mathrm{T}}$ distribution using the PF algorithm in dijet events. The open points show the distribution in data before cleaning algorithms have been applied and the filled points show the distribution after cleaning. The stacked histograms show the leading SM contributions from simulation, which approximately agree with the cleaned data distribution. Figure taken from Ref. [85].

crystals, which takes into account the distinct pattern of energy deposition associated with electrons. This pattern corresponds to a narrow range of deposition in η but a significant spread in ϕ due to the curvature of the electron trajectory in the transverse plane as it traverses the tracker material and emits bremsstrahlung radiation. A supercluster is matched to a track seed in the pixels from which the electron track is built. The subsequent electron track reconstruction does not use the CMS standard algorithm, but instead uses a "Gaussian sum filter" [87] to

model the details of electron energy loss in the tracker region. If the supercluster and track momentum measurements agree, then their weighted average is used to determine the final electron momentum. If they disagree significantly, then the one that is expected to provide the least biased measurement, based on the electron momentum, provides the final momentum.

The tracker-driven seeding algorithm [88] is part of the PF event reconstruction. This algorithm is better for low p_T electrons due to the superior resolution at low-momentum of the tracker and the minimum ECAL energy deposit required for ECAL-driven seeding. However, for the electron p_T threshold used in this analysis, this is not important. Because PF objects are used to calculate the $\not{E}_{\mathrm{T}}$, to avoid biases it is important to check that the selected electrons from ECAL-driven seeding match those found by PF.

To differentiate true, prompt electrons from backgrounds, the following set of identification criteria are applied. Backgrounds include jets which fluctuate in their fragmentation to give mostly electromagnetic energy, leptonic hadron decays within jets, and photon conversions. A less stringent set of requirements are used to select veto electrons, in order to efficiently reject events with multiple leptons.

- Transverse momentum: Selected electrons must have $p_T > 20$ GeV. This threshold is largely motivated by trigger efficiency considerations. Veto electrons must have $p_T > 15$ GeV.

- Pseudorapidity: To remain within the acceptance of the tracker, selected and veto electrons must have $|\eta| < 2.5$ and not be within the transition region between the EB and EE.

- Track-supercluster $\Delta\phi$: The difference in ϕ between the electron track extrapolated to the ECAL and the supercluster must be less than 0.06(0.03) for selected electrons in the EB(EE). Veto electrons in the EB(EE) must have this $\Delta\phi$ less than 0.08(0.07).

- Track-supercluster $\Delta\eta$: The difference in η between the electron track extrapolated to the ECAL and the supercluster must be less than 0.004(0.007) for selected electrons in the EB(EE). Veto electrons in the EB(EE) must have this $\Delta\eta$ less than 0.007(0.01).

- ECAL shower η width: Prompt electrons have a narrow shower shape in η compared to backgrounds from π^0 meson decays, which give two nearly overlapping photons. The width of the shower in η is characterized by the variable $\sigma_{i\eta i\eta}$, defined in [89], which must be less than 0.01(0.03) for selected and veto electrons in EB(EE).

- Hadronic vs electromagnetic energy: The ratio of energy deposited into the HCAL behind the electron supercluster divided by the energy of the electron must be less than 0.12(0.1) for EB(EE) selected electrons. Veto electrons in

the EB must have this quantity less than 0.15. This requirement is designed to reject jets which fake prompt electrons.

- dZ: The distance in z between the electron and leading primary vertex at the point of closest approach must be less than 1(2) mm for selected(veto) electrons.

- Transverse impact parameter: The distance in the transverse plane between the electron and leading primary vertex at the point of closest approach must be less than 0.2(0.4) mm for selected(veto) electrons.

- E vs p: $|1/E - 1/p|$, where E comes solely from the ECAL and p comes solely from the tracker, must be less than 0.05 for selected electrons.

- Conversion rejection: Selected electrons can have at most one missing hit in the inner tracker layers. A full vertex fit, constrained to be consisted with a conversion, is also performed using the electron track paired with other tracks. The probability of this fit for any pair which includes the electron track must be less than 10^{-6}.

- PF electron matching: The closest PF reconstructed electron in ΔR to the selected electron must have p_T within 10 GeV.

- Relative Isolation: Prompt electrons should have minimal activity in the tracker and calorimeter in their immediate vicinity, i.e., be isolated. Using the PF algorithm, the sum of transverse energy from neutral hadrons, charged hadrons, and photons within a $\Delta R < 0.3$ cone of the electron is computed. Only charged hadrons matched to the same vertex as the electron are included in this sum. The neutral hadron and photon sum is corrected for the average contribution from PU based on the energy density in the event. This transverse energy sum is divided by the p_T of the electron to give the relative isolation of the electron, which must be less than 0.15 for selected and veto electrons.

The electron selection efficiency is derived with a "tag-and-probe" technique [90] in a sample of DY events at the Z mass resonance. In this technique, events containing a tag electron that passes the full set of selection criteria and a probe electron passing a less stringent selection are used. Such events must have dilepton invariant mass near the Z mass, indicating that the probe electron is likely a real, prompt electron. The efficiency of the selection requirements not applied to the probe electron is given by the fraction of probe electrons which pass them. The average electron selection efficiency is found to be roughly 80%. The efficiency increases with p_T and decreases with $|\eta|$, but does not vary more than about 20%.

4.5 Muons

Muons in CMS are reconstructed [91] using information from both the tracker and muon system. There are two distinct reconstruction approaches, which are seeded either by information solely from the tracker or muon system. In the first method, called global muon reconstruction, a muon track is found in the muon system and matched to a tracker track. The information from the muon system and tracker is then combined in a global fit of the muon trajectory. In the second method, called tracker muon reconstruction, tracker tracks are extrapolated to the muon system. If the extrapolation matches to a track stub in a DT or CSC chamber, the tracker track is considered to have come from a muon. For muons with $p_T < 200$ GeV, the momentum is taken solely from the tracker muon as the information from the muon system does not significantly improve the resolution. For higher p_T muons, the tracker and muon system measurements are used in conjunction to determine the p_T. The PF algorithm also finds muon candidates [92], starting with the candidates reconstructed with the two algorithms described above, but utilizing additional information from the calorimeters.

In order to differentiate true, prompt muons from backgrounds, the following set of identification criteria are applied. Backgrounds include leptonic hadron decays within jets, hadron punch-through, and cosmic ray muons. Hadron punch-

through occurs when a hadron produced in a jet makes it all the way to the muon system. A less stringent set of requirements are used to select veto muons, in order to efficiently reject events with multiple leptons.

- Transverse momentum: Selected muons must have $p_T > 20$ GeV. As with electrons, this threshold is largely motivated by trigger efficiency considerations. Veto muons must have $p_T > 15$ GeV.

- Pseudorapidity: To remain within the acceptance of the tracker and muon system, selected muons must have $|\eta| < 2.4$. Veto muons must have $|\eta| < 2.5$.

- Reconstruction Algorithm: Selected muons must be reconstructed with both the global and tracker reconstruction algorithms. Veto muons must be reconstructed by at least one of the two.

- dZ: The distance in z between the muon track and leading primary vertex at the point of closest approach must be less than 5 mm for selected and veto muons.

- Transverse impact parameter: The distance in the transverse plane between the muon track and leading primary vertex at the point of closest approach must less than 0.2(2) mm for selected(veto) muons.

- Normalized χ^2: The χ^2 per number of degrees of freedom of the global muon fit must be less than 10 for selected muons.

- Number of valid muon hits: For selected muons, at least one muon chamber hit must be included in the global muon fit.

- Number of matched muon stations: For selected muons, the extrapolation of the tracker track to the muon system must match hits in at least two muon stations.

- Number of pixel hits: For selected muons, the track must have at least one hit in the pixel tracker.

- Number of tracker layers: For selected muons, the track must have hits in at least 6 layers of the tracker.

- PF muon matching: Selected and veto muons should both be reconstructed by the PF algorithm. For selected muons, the p_T of the corresponding PF reconstructed muon must be within 5 GeV. As with electrons, this matching is important to avoid biases in the $\not\!\!E_{\mathrm{T}}$, which uses PF reconstructed muons.

- Relative Isolation: As with electrons, prompt muons should be isolated. The relative isolation within a $\Delta R < 0.3$ cone of the muon is computed in the same way as for electrons. The sole exception is the correction for the

contribution from PU to the neutral hadron and photon energy sum. This correction is obtained by subtracting half of the energy deposited within the isolation cone of the muon by charged hadrons not associated with the leading primary vertex. The factor of 0.5 comes roughly from the ratio of the neutral hadron and photon to charged hadron energy resulting from PU interactions. Selected(veto) muons must have relative isolation less than 0.12(0.2).

The muon selection efficiency is derived with the same tag-and-probe technique as described above for electrons. The average muon selection efficiency is found to be roughly 90%. The efficiency varies by less than 10% with p_T and $|\eta|$.

Chapter 5

Strategy, Samples, and Selection

5.1 Analysis Strategy

As described in Ch. 2, searches for gluino pair production at the LHC are well motivated by naturalness considerations and the significant cross-section due to strong production. As top squark masses are more constrained than other squarks and gluinos by naturalness, gluinos would likely be heavier than stops and decay through them, i.e., $\tilde{g} \to t\tilde{t}^{(*)}$. If the mixing between the different flavor squarks is not large and the mass splitting between the stop and LSP is sufficiently large, then the stops would decay primarily via $\tilde{t} \to t\tilde{\chi}_1^0$. Hence an event with gluino pair production could result in a final state with four top quarks and two LSPs.

Such an event would almost certainly leave a striking signature in the detector. The probability of exactly one electron or muon in the final state, either directly from one of the four W decays or from a tau which is a W decay product (e.g.,

$W \to \tau\bar{\nu}_\tau$ where $\tau \to \ell\bar{\nu}_\ell\nu_\tau$), is roughly 40%. The probability for all numbers of leptons in the final state is shown in Fig. 5.1. Because the most likely lepton multiplicity is one, it is a natural choice to perform a search for this phenomenon in the single lepton channel. As each of the top quarks yields a bottom quark as one of its decay products, there would be four b quarks in the final state. Assuming that three of the four W bosons decay hadronically to produce two quark jets each, there would be 10 jets in the event, ignoring acceptance and initial state radiation (ISR) effects. The two weakly interacting LSPs in the final state will contribute to the $\not\!\!E_{\mathrm{T}}$.

The mass splitting between the gluino and LSP determines the energy scale of the event, in particular the sum of $\not\!\!E_{\mathrm{T}}$ and H_T will be on the same scale as $2\left(m(\tilde{g}) - m(\tilde{\chi}_1^0)\right)$. This is over a TeV of energy for much of the interesting parameter space, but can also be quite small. To obtain sensitivity to as broad a range of mass splittings as possible, the strategy of using a signal region consisting of multiple exclusive bins of $\not\!\!E_{\mathrm{T}}$ and H_T thresholds has been adopted. Additionally, the energy scale of the event affects the average jet p_T which influences b-tagging acceptance and efficiency. For this reason, the signal region is divided into exclusive bins in the number of b-tagged jets, N_b.

Despite the fact that such a signature from gluino pairs decaying through stops would be quite striking, there are SM processes that can mimic it. The foremost

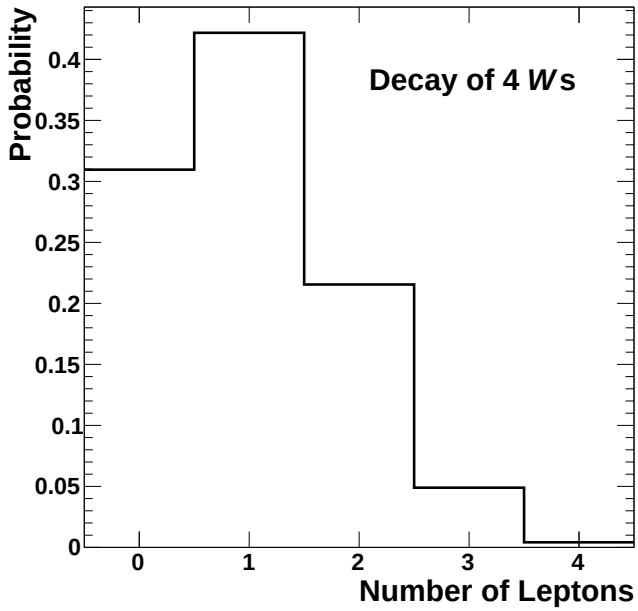

Figure 5.1: Distribution of the number of leptons from the decays of 4 W bosons. Leptons from tau decays are counted toward the total. The relevant branching fractions for W and τ decays are taken from [47]. Acceptance and selection efficiency effects are ignored.

such process is $t\bar{t}$ pair production, which has two true b jets, two W bosons, and a much higher inclusive cross-section than the signal. The second most likely process to mimic the signal is single-top production, but this has a smaller cross section than $t\bar{t}$ production, only one true b jet, and fewer jets than $t\bar{t}$. Next is W boson production in association with multiple jets, which has little true b jet enrichment. The inclusive W production cross section is very large but decreases rapidly as the number of associated jets and H_T is increased, such that it becomes a sub-dominant background in this search.

All other SM processes are expected to have a very small contribution to the background. The ones considered in this analysis are di-boson (i.e., WW, WZ, and ZZ) production, Drell-Yan (DY) production with associated jets, $t\bar{t}Z$ and $t\bar{t}W$ production, and QCD multi-jet production. With the exception of $t\bar{t}Z$ and $t\bar{t}W$, which have extremely small cross sections, all of these processes lack a significant true b-jet contribution. Leptonic Z boson decays are further suppressed because they result in two leptons and no true $\not{E}_{\mathrm{T}}$. Finally the QCD background has no true prompt leptons and few true b jets. Despite its large cross section, these factors are expected to sufficiently suppress the QCD background to a negligible level, as confirmed by a dedicated estimate of this background.

The estimation of the SM background is described in Ch. 6 and separately predicts the components based on the number of taus and leptons in the final state. The dominant background contribution comes from true single-lepton events (i.e., events with exactly one leptonic W decay and no other leptons or taus) and is estimated using the charged lepton p_T spectrum. The majority of the remainder of the background is comprised of events containing taus, which is estimated by emulating tau decays in various data control samples.

5.2 Data Sample

This analysis is performed using a data sample corresponding to 19.3 ± 0.5 fb^{-1} of integrated luminosity collected by CMS during the 2012 LHC $\sqrt{s} = 8$ TeV pp collision run. The total integrated luminosity collected by CMS during this period was 21.8 ± 0.6 fb^{-1}, but some portions cannot be used due to various temporary problems in the operation of CMS. For example, a suddenly noisy channel in the HCAL might lead to a high jet-trigger rate which uses up nearly the entire Level-1 Trigger bandwidth and prevents interesting events from being saved.

The data events in the signal sample of this analysis are required to pass at least one of a set of multi-object HLT triggers which require $\not{E}_{\mathrm{T}}$, H_T, and a lepton (electron or muon). All of these triggers require the $\not{E}_{\mathrm{T}}$ to be greater then 45 or 50 GeV. The triggers with a muon leg require either $p_T^{\mathrm{muon}} > 15$ GeV and $H_T > 350$ GeV or $p_T^{\mathrm{muon}} > 5$ GeV and $H_T > 400$ GeV. The triggers with an electron leg require either $p_T^{\mathrm{electron}} > 15$ GeV and $H_T > 300$ GeV or $p_T^{\mathrm{electron}} > 5$ GeV and $H_T > 350$ GeV.

The data events in the control sample used to estimate the true single-lepton background are required to pass at least one of a set of HLT triggers which require H_T and a lepton but no $\not{E}_{\mathrm{T}}$. The H_T thresholds are compatible with those of the signal region; namely $H_T > 350$ GeV for the muon triggers and $H_T > 300$ GeV

for the electron triggers. To keep the trigger rates at a reasonable level, the lepton p_T requirement is significantly increased to 40 GeV for both electrons and muons to compensate for the lack of a $\not\!\!E_{\mathrm{T}}$ requirement.

To not exceed its limited computing resources, the reconstruction algorithms used by the HLT are much faster approximations of the full offline reconstruction described in Ch. 4. Therefore, the offline and trigger reconstructed objects in an event will not be identical. More stringent offline requirements than the trigger thresholds are used to ensure high trigger efficiency. The combined efficiency of the H_T and $\not\!\!E_{\mathrm{T}}$ legs of the signal region triggers is just over 98% for the signal selection. The H_T leg of the control sample triggers has similar efficiency for the control sample selection. For both the signal and control samples, the corresponding triggers have roughly 96% efficiency for electrons, 98% efficiency for muons with $|\eta| < 0.9$, and 84% efficiency for muons with $|\eta| > 0.9$.

An additional set of triggers requiring only H_T is used to select a control sample with no lepton or $\not\!\!E_{\mathrm{T}}$ requirements in which the $\not\!\!E_{\mathrm{T}}$ from detector resolution effects is modeled. Multiple triggers are needed with different thresholds in order to cover the entire relevant range of H_T. Low H_T events are obtained through low threshold triggers which have large prescales. The prescale of a trigger is the inverse of the fraction of events in which that trigger path is considered. The high H_T events are obtained through higher threshold triggers which have smaller prescales or are

not prescaled at all. This is important because the high H_T event rate is much smaller and combined with a large trigger prescale would result in too few events in the control sample to effectively model the $\not{E}_{\mathrm{T}}$ resolution.

5.3 Simulated Events

In addition to data, this analysis utilizes event samples simulated with Monte Carlo methods to aid in the background prediction and to interpret the results in the context of a supersymmetric model. The simulation of SM processes is an invaluable tool because it allows the background prediction methods to be tested in a sample with much higher statistical precision than the data and because generator-level information can be used to obtain the true identity and momentum of each particle produced in the collision.

The MadGraph 5 generator [93] is used for $t\bar{t}$, W + jets, DY+jets, $t\bar{t}W$, $t\bar{t}Z$, and QCD multijet production. The POWHEG generator [94] is used for single top-quark and $t\bar{t}$ production. The usage of two $t\bar{t}$ samples is because the larger MadGraph version does not specially handle tau-lepton decays via TAUOLA [95], and consequently is not used in the prediction of the background consisting of events with taus from W boson decays. The remaining simulated SM samples, consisting only of diboson production, are generated with

the PYTHIA 6.4 generator [96]. The samples generated by MadGraph and PYTHIA use the CTEQ6L1 [97] parton distribution functions (PDFs) to parametrize the fractional momentum carried by the partonic constituents of each proton. The single top-quark samples use the CTEQ6.6M [98] PDFs and the POWHEG $t\bar{t}$ sample uses the CT10 [99] PDFs. Additionally, each sample uses the Geant4 package [100] to model the detector response and PYTHIA 6.4 with tune Z2* [101] to describe showering and hadronization.

The cross sections for each of the simulated SM samples are calculated at NLO or higher, with the exception of QCD, for which the leading order (LO) cross section calculated by the MadGraph generator is used. Most of the higher order calculations are done using either the program MCFM 6.1 [102] or FEWZ [103]. In the case of $t\bar{t}$ and single-top production, the cross sections are computed [104] at approximate next to next to leading order (NNLO). The W + jets process is simulated in bins of H_T, for which the LO cross section in each bin is corrected by the ratio of the NLO to LO cross section for inclusive W production.

The SUSY signal is generated with MadGraph 5, and uses the same PDFs and PYTHIA tune as the SM simulation. The key difference is the use of a fast simulation [105] technique to model the detector response instead of Geant4. This is done to drastically decrease the simulation time, which is necessary due to the large number of signal events needed to effectively scan over the relevant SUSY

parameter space. The fast simulation does a good job of matching the GEANT4 based simulation, but a few small differences are noticeable; most notably, the b-tag and lepton selection efficiencies are a few percent higher in the fast simulation.

To effectively use the SM simulation, significant differences with the data must be corrected. One such difference is that the simulated distribution of the number of PU interactions does not match that of the data. The mismatch comes from the fact that the PU distribution in the simulation was chosen before the majority of the 2012 dataset had been recorded. Correcting this difference is important because lepton selection efficiencies vary significantly with the amount of PU. The PU distribution in data is calculated from instantaneous luminosity measurements combined with the total pp inelastic cross-section, which the corresponding distribution in simulation is scaled bin-by-bin to match.

Lepton efficiencies in the fast simulation signal samples are corrected to remove the few percent difference with the data. However, SM simulation lepton efficiencies are within a percent of the data and are not corrected. Another difference between data and simulation is that no trigger requirements are applied to the simulation. The exact set of triggers used in data are not simulated, meaning the trigger efficiencies measured in data must be directly applied to the simulation.

The final items to correct in the simulation are the b-tagging efficiency and mistag rate, using the scale factors described in Sec. 4.2.1. Due to the presence

of multiple jets in each event, care must be taken in the application of these scale factors. The corrected efficiencies and mistag rates for the jets in an event are utilized with the appropriate combinatorial factors to determine the new weight for that event. For the fast simulation, the slightly different simulated efficiencies require distinct scale factors, which are applied in the same way.

5.4 Event Selection

In order to effectively target gluino production and decay through stops, the following requirements are used to select the signal sample: at least one good primary vertex; six or more jets, at least two of which are identified as b jets by the CSVM tagger; exactly one selected electron or muon and no additional veto electrons or muons; $H_T > 500$ GeV; and $\not{E}_{\mathrm{T}} > 150$ GeV. Chapter 4 describes the reconstruction of these objects. The additional lepton veto is necessary to simplify the background composition and ensure it is dominated by true single-lepton events. The H_T and $\not{E}_{\mathrm{T}}$ requirements are designed to be as minimal as possible while ensuring that the selected events are on the efficiency plateau for the corresponding legs of the signal triggers. In order to cross-check the background estimation methods employed in this analysis, the event yields are also predicted in a signal depleted validation region. This validation region is selected to be

kinematically very similar to the signal region, with the only difference being the requirement of between 3 and 5 jets.

In addition to the above selection some additional cleanup requirements are necessary. For one, jets are excluded from the jet multiplicity (N_{j}) and H_T calculations if they overlap within $\Delta R < 0.3$ of any veto electrons or muons. This prevents the double counting of leptons as jets by the PF algorithm. As indicated in Sec. 4.3, to effectively use a data sample with a large $\not\!\!E_{\mathrm{T}}$ requirement, filters must be imposed to reject events which are likely to have large artificial $\not\!\!E_{\mathrm{T}}$. The filters used in this analysis are designed to remove events affected by the following problems. These problems have clear signatures, and consequently the filters used to reject them have minuscule probability to reject non-problematic events.

- Beam halo and beam scraping: The LHC beam can interact with gas in the beam pipe or the beam collimators, producing showers of particles. Muons produced in these showers can traverse CMS and deposit significant energy in the calorimeter in time with the proton bunches.

- HB and HE noise: Individual HPDs as well as groups of 4 HPDs (a readout box) occasionally generate significant anomalous noise.

- Tracking failure: In events with extremely large tracker hit multiplicity, the track reconstruction algorithm can fail to efficiently reconstruct tracks. This

results in events with large calorimeter energy deposits, but relatively few tracks. This signature can also be created by events which come from proton-proton collisions far away from the nominal collision point, at $|z| \approx 75$ cm.

- HCAL laser misfire: The laser used for HCAL calibration rarely misfires during collision data taking, leading to huge energy deposits in the HCAL and $\not\!\!E_{\mathrm{T}}$ due to non-uniformity of the calibration system.

- Noisy EE clusters: There are two 5×5 groups of crystals in the EE which occasionally produce high amplitude noise.

- Dead ECAL channels: Around 1% of the crystals in the ECAL are masked in reconstruction either because they are noisy or have readout-electronics which cannot send data. In the case that a jet or electron deposits energy into one or more of these channels, significant artificial $\not\!\!E_{\mathrm{T}}$ can be created.

- Improperly calibrated ECAL channels: In the course of regularly updating the transparency loss corrections for the ECAL, some channels can be assigned unphysically large correction factors, leading to $\not\!\!E_{\mathrm{T}}$.

To gain sensitivity to a broad range of parameter space, the signal region in this analysis is divided into bins of $\not\!\!E_{\mathrm{T}}$ and N_b as well as by distinct H_T thresholds. The $\not\!\!E_{\mathrm{T}}$ is divided into bins of $(150, 250]$, $(250, 350]$, $(350, 450]$, $(450, \mathrm{inf})$ GeV. Bins

of exactly 2 and three or more b tags are used. The H_T is not separated into exclusive bins, but rather by three thresholds of 500, 750, and 1000 GeV.

Chapter 6

Background Prediction

There are multiple SM processes which can produce events which pass the event selection requirements in Sec. 5.4 and thereby mimic the SUSY signature targeted by this analysis. The prediction of the SM background in the $N_b = 2$ signal regions is divided into categories, described below, each of which employs a distinct estimation method. The categories are distinguished by the number of prompt leptons in the final state as well as the presence of tau-leptons. Each estimation method, described in Sec. 6.1-6.3, derives its power mainly from the data, with the exception of the prediction of the extremely small $Z+$jets background, which is taken from simulation and assigned a 100% systematic uncertainty.

However, the extremely small event yields in the $N_b \geq 3$ data control samples mean they cannot be used to adequately estimate the $N_b \geq 3$ signal yields. Instead, the $N_b \geq 3$ background estimates are obtained from the $N_b = 2$ predictions using an extrapolation factor derived in simulation, as described in Sec. 6.4.

The predictions of the $N_{\mathrm{j}} \geq 6$ signal regions and $3 \leq N_{\mathrm{j}} \leq 5$ validation regions are performed using identical procedures. The only difference between the two predictions is the N_{j} requirement in the respective control samples. Therefore, the tables and figures in this chapter will focus on the signal region and the validation region predictions will be summarized in Ch. 7.

6.1 Single Lepton Background

The dominant background in this search comes from events with exactly one prompt lepton and no $W \to \tau\nu$ decays and constitutes roughly two-thirds of the total background. The Lepton Spectrum (LS) method used to estimate its contribution is based on the approximate equivalence in the SM of the momentum spectra of charged leptons and neutrinos in $W \to \ell\nu_\ell$ decays. Due to this near equivalence, the charged lepton p_T spectrum can be used with small, well-understood corrections to predict the neutrino, and hence $\not{E}_{\mathrm{T}}$, spectrum. This has the desirable feature that it can be done in a data-driven manner with respect to important effects which are not necessarily well simulated, such as the $\not{E}_{\mathrm{T}}$ resolution and the high tail of W boson p_T distribution. Furthermore, such a prediction suffers little contamination from SUSY events, which generally have

an enhanced $\not{E}_{\mathrm{T}}$ spectrum compared to their charged lepton p_T spectrum due to the presence of LSPs.

Figure 6.1 illustrates the principle underlying this method by showing the $\not{E}_{\mathrm{T}}$ versus lepton p_T in the dominant SM background of $t\bar{t}$ and a SUSY T1tttt benchmark model. Consider the neutrino and lepton p_T in a single lepton $t\bar{t}$ event. In the W rest frame, the lepton and neutrino would have the same momentum. However, in the lab frame the boost of the W enhances the p_T of either the lepton or neutrino with respect to the other, depending on their angle of decay relative to the W momentum axis. Because this anti-correlation affects leptons and neutrinos nearly democratically, the lepton and neutrino($\not{E}_{\mathrm{T}}$) spectra are similar. This is very different than the typical SUSY model, as illustrated in the figure, in which the lepton p_T spectrum has a much smaller mean than the $\not{E}_{\mathrm{T}}$ spectrum.

In order to use the lepton p_T spectrum to accurately predict the $\not{E}_{\mathrm{T}}$ spectrum of SM single lepton events, there are a few important effects which must be taken into account.

- $\not{E}_{\mathrm{T}}$ resolution: Because the detector does not have perfect resolution, the measured $\not{E}_{\mathrm{T}}$ will not be identical to the neutrino p_T. Instead, the imperfect jet and lepton measurements lead to a smearing of the $\not{E}_{\mathrm{T}}$. Because the lepton p_T measurements are more precise, the jet energy resolution dominates the $\not{E}_{\mathrm{T}}$ resolution. Therefore, the $\not{E}_{\mathrm{T}}$ resolution can be quantified using a

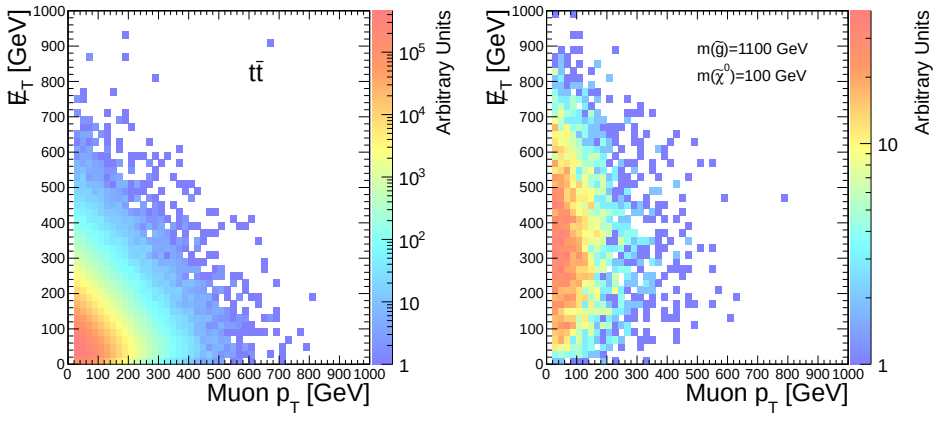

(a) (b)

Figure 6.1: Distributions of $\not\!\!E_{\mathrm{T}}$ vs muon p_T for single lepton events in simulated samples of (a) $t\bar{t}$ events and (b) the T1tttt model with $m(\tilde{g}) = 1100$, $m(\tilde{\chi}_1^0) = 100$ GeV. In $t\bar{t}$ events, the lepton p_T and $\not\!\!E_{\mathrm{T}}$ spectra are very similar. In the T1tttt benchmark model, which is typical of many SUSY models, the $\not\!\!E_{\mathrm{T}}$ is larger on average than the lepton p_T, since it is enhanced by the presence of two LSPs.

QCD multi-jet sample. For events passing the minimal signal selection, the $\not\!\!E_{\mathrm{T}}$ threshold (150 GeV) is significantly larger than the resolution, meaning the $\not\!\!E_{\mathrm{T}}$ does serve as a reasonable proxy for the neutrino p_T.

- Non single lepton events: The good agreement between the lepton p_T and $\not\!\!E_{\mathrm{T}}$ spectra is only achieved in true single lepton SM events. In events with multiple neutrinos, disregarding resolution effects, the $\not\!\!E_{\mathrm{T}}$ is given by the vector sum of the neutrino p_T's, which will be greater on average than the p_T of the selected lepton. Multiple neutrinos can arise from multiple leptonic

W decays in an event or a single $W \to \tau\nu_\tau \to \ell\nu_\ell\nu_\tau\nu_\tau$ decay. These types of backgrounds are predicted separately, as described in Sec. 6.2.

- W boson polarization: The polarization of W bosons in SM processes together with the $V - A$ nature of the weak interaction result in differing neutrino and lepton p_T spectra, described in more detail in Sec. 6.1.2. Due to the distinct nature of direct W boson and $t\bar{t}$ production, the W polarization distribution is different in events with top quarks and $W +$ jets events.

- Lepton p_T threshold: Due to the anti-correlation described above between the lepton and neutrino p_T in individual W decays, the lepton p_T requirement in the signal selection biases the neutrino spectrum. This requirement removes only events with low lepton p_T which can have much larger neutrino p_T. The net result is that the high tail of the $\not{E}_{\mathrm{T}}$ spectrum is shifted down while the lepton p_T spectrum is unaffected.

The effects of the last two items in this list are visualized in Fig. 6.2, in which the generator level muon and muon-neutrino p_T spectra in $t\bar{t}$ simulation are plotted before and after a muon $p_T > 20$ GeV requirement. Before the p_T requirement, the enhancement of the neutrino spectrum compared to the muon spectrum indicates the effect of W polarization. The effect of the muon p_T requirement is apparent in the downward shift of the neutrino spectrum.

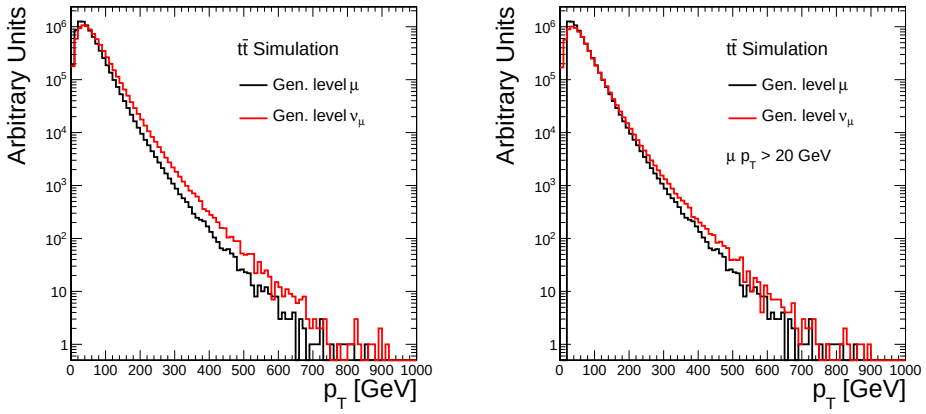

(a) (b)

Figure 6.2: The muon and muon-neutrino p_T spectra in simulated $t\bar{t}$ single-lepton events (a) before and (b) after a muon $p_T > 20$ GeV requirement. All quantities are generator level. Muon $|\eta| < 2.4$ is required in both plots.

To predict the single lepton background, a control sample with no $\not\!\!E_{\rm T}$ requirement, lepton $p_T > 50$ GeV, and all the other requirements of the signal selection is used. The lepton p_T threshold is set to be on the efficiency plateau of the lepton plus H_T cross-trigger used to select the events. The lepton p_T distribution in the data control sample is smeared with the $\not\!\!E_{\rm T}$ resolution derived from data to obtain a raw prediction of the $\not\!\!E_{\rm T}$ distribution in the signal region. However, this raw prediction must still be corrected to account for the final three bullets in the above list. These three effects are all related to the W boson decays and are well described in the simulation. The correction of the raw prediction is done with the multiplicative factor $\kappa_{\rm LS}$, derived using the SM simulation separately for

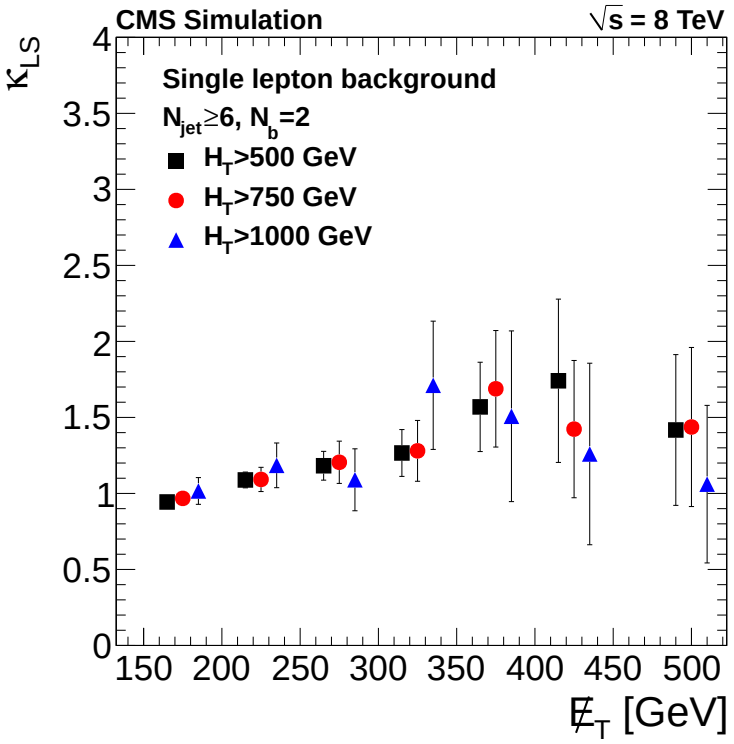

Figure 6.3: κ_{LS} as a function of $\not\!\!E_{\mathrm{T}}$ for $N_b = 2$, $N_{\mathrm{j}} \geq 6$, and the three H_T thresholds. The final $\not\!\!E_{\mathrm{T}}$ bin extends to infinity. The 50 GeV bins of $\not\!\!E_{\mathrm{T}}$ are used here for illustration purposes, while the values of κ_{LS} used in the analysis correspond to the signal $\not\!\!E_{\mathrm{T}}$ bins.

each signal bin of $\not\!\!E_{\mathrm{T}}$. It is defined as

$$\kappa_{\mathrm{LS}}(\not\!\!E_{\mathrm{T}}) = \frac{N^{\mathrm{true}}(\not\!\!E_{\mathrm{T}})}{N^{\mathrm{pred}}_{\mathrm{raw}}(\not\!\!E_{\mathrm{T}})}, \tag{6.1}$$

where $N^{\mathrm{true}}(\not\!\!E_{\mathrm{T}})$ is the number of simulated true single lepton events and $N^{\mathrm{pred}}_{\mathrm{raw}}(\not\!\!E_{\mathrm{T}})$ is the number of raw predicted events when using the simulated lepton p_T distribution smeared with the $\not\!\!E_{\mathrm{T}}$ resolution. Figure 6.3 shows κ_{LS} as a function of $\not\!\!E_{\mathrm{T}}$ for $N_b = 2$, $N_{\mathrm{j}} \geq 6$, and the different H_T thresholds.

The most challenging aspects of the Lepton Spectrum prediction are accounting for the $\not\!\!E_{\rm T}$ resolution, W polarization, and systematic uncertainties. The next three subsections describe in more detail the way in which these are handled.

6.1.1 $\not\!\!E_{\rm T}$ Resolution

As mentioned above, the lepton p_T resolution is significantly better than that of the $\not\!\!E_{\rm T}$, a fact which must be accounted for when using the lepton p_T spectrum to predict the $\not\!\!E_{\rm T}$ spectrum. This is done using $\not\!\!E_{\rm T}$ resolution templates derived in a QCD multijet dominated data control sample. This particular control sample is used because the $\not\!\!E_{\rm T}$ should be dominated by detector resolution due to the lack of neutrinos in QCD multijet events. Further, because the templates are derived in data, even anomalous sources of large artificial $\not\!\!E_{\rm T}$ are taken into account in the prediction, provided that they have the same frequency in QCD multijet and single lepton events.

To obtain the QCD multijet dominated control sample, no requirement on the presence of leptons is made. Because the $\not\!\!E_{\rm T}$ distribution is correlated with both H_T and $N_{\rm j}$, the templates are binned in each. Template bins with $N_{\rm j} = 4$ and $N_{\rm j} \geq 5$ are used in the $3 \leq N_{\rm j} \leq 5$ validation and $N_{\rm j} \geq 6$ signal region predictions, respectively. The $N_{\rm j}$ threshold is relaxed from the signal selection in order to increase the statistical precision of the templates. Events are also required to

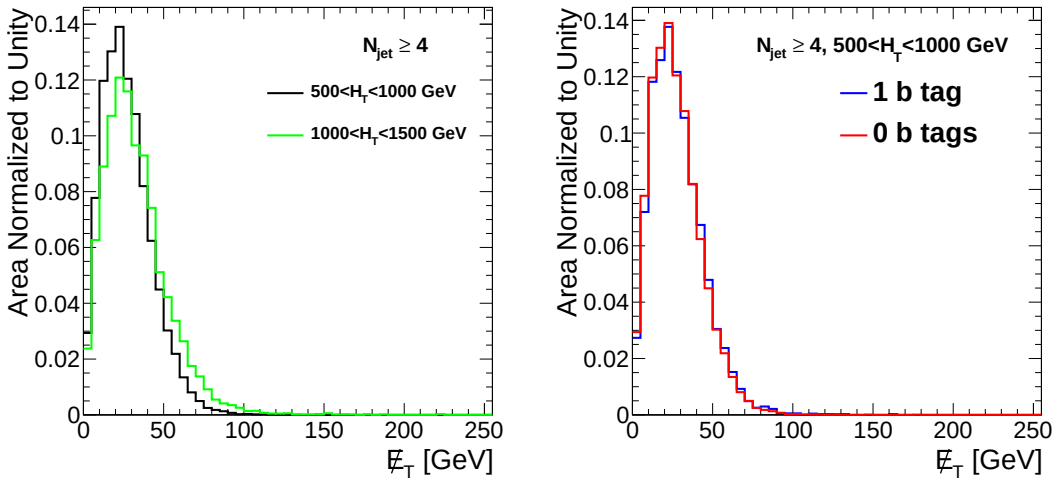

(a) (b)

Figure 6.4: $\not\!\!E_{\mathrm{T}}$ templates for different selections. To decrease the statistical uncertainty for illustrative purposes, the jet requirement has been loosened to $N_{\mathrm{j}} \geq 4$ and much wider than usual H_T bins are used. (a) shows two templates with different H_T requirements, and (b) shows two templates with different N_b.

have at least one CSVM tagged jet. This is important because b jets can decay semi-leptonically, which produces neutrinos and contributes to the $\not\!\!E_{\mathrm{T}}$. As with N_{j}, the N_b requirement is relaxed compared to the signal selection in order to increase the statistical precision of the templates. Fig. 6.4 shows a few example templates and illustrates the effect of the H_T and N_b selections on the template shape. The larger H_T selection slightly increases the mean and width of the core while the N_b selection has very little effect.

The data control sample is selected using a set of H_T triggers. As described in Sec. 5.2, a wide range of H_T thresholds are needed due to trigger prescale

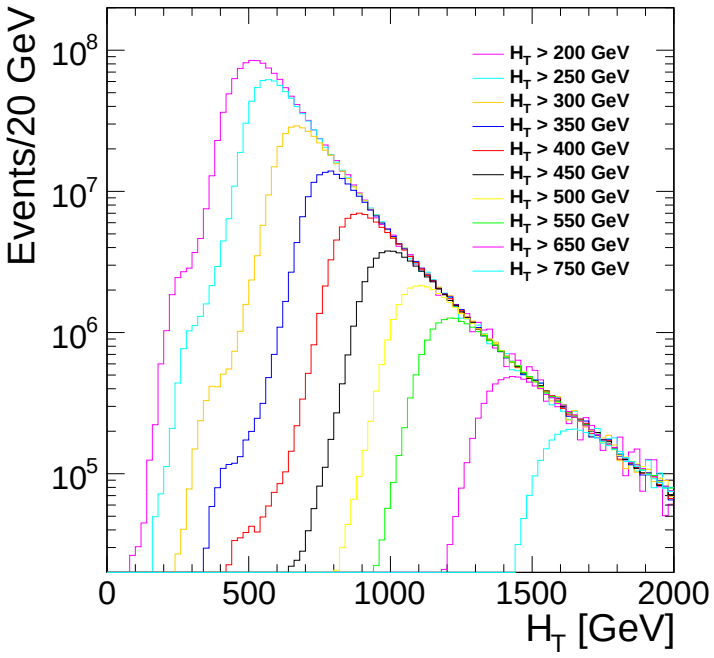

Figure 6.5: Reconstructed H_T in 19.3 fb^{-1} of data for the different H_T triggers.

considerations. Fig. 6.5 shows the H_T distribution for the different triggers used in the selection, corrected according to their prescales. An event with a given H_T enters the $\not\!\!E_{\rm T}$ resolution templates only if it passes the trigger with the lowest prescale, i.e., highest threshold, which is approximately fully efficient for that H_T. The $\not\!\!E_{\rm T}$ resolution templates correspond to 10 GeV wide bins of H_T with bin edges such that only one H_T trigger is used to select events in a given template.

The following procedure is performed to correct the lepton p_T spectrum by the $\not\!\!E_{\rm T}$ resolution using a set of toy samples smeared with the $\not\!\!E_{\rm T}$ resolution templates. To accomodate the H_T binning of the $\not\!\!E_{\rm T}$ templates, the uncorrected

lepton p_T spectrum is binned in both lepton p_T and H_T. For a given toy, each bin of the uncorrected lepton p_T spectrum and $\not\!\!E_{\rm T}$ templates has its number of entries independently varied according to its statistical uncertainty. For each bin of the uncorrected lepton p_T spectrum, a random value is chosen according to the applicable $\not\!\!E_{\rm T}$ resolution template and added vectorially at a random angle to the p_T. The resulting magnitude of the smeared p_T along with the normalization of the original unsmeared bin are used to fill the corrected lepton p_T spectrum. After doing this for all bins of the uncorrected lepton p_T spectrum, the corrected spectrum for that toy is obtained. The central value and statistical uncertainty on a given bin of the corrected lepton p_T spectrum comes from the mean and standard deviation, respectively, of that bin across the ensemble of toys. The smearing results in a roughly 10% enhancement of the high lepton p_T tail.

6.1.2 W Boson Polarization

The polarization of W bosons is one of the most important factors that gives rise to the asymmetry of the lepton and neutrino p_T spectra in single lepton events. In particular, asymmetry in the W polarization distribution combined with the $V-A$ nature of the W decays creates an asymmetry in the angular distribution of the decay lepton and neutrino in the W rest frame with respect to the W momentum axis. When boosted to the lab frame, this angular asymmetry

results in differing lepton and neutrino p_T spectra. The relative difference in the spectra is largest at high p_T, which coincides with the phase space probed by this analysis. This section discusses the effects of W polarization in $t\bar{t}$ and $W+$jets events, which are treated separately due to their distinct characteristics.

To characterize the polarization distribution, the fractions of W bosons with positive helicity (f_{+1}), negative helicity (f_{-1}), and zero helicity (f_0) are used. The axis used for the helicity calculation is the W flight direction in the lab frame for $W+$jets events and in the top rest frame in $t\bar{t}$ events. The top rest frame is used in $t\bar{t}$ events because the W comes from the decay of a top quark. The angle between the W flight axis and the lepton in the W rest frame is used to define a polar angle θ^*_ℓ and azimuthal angle ϕ^*_ℓ. Using the fact that a spin-1 W decays to a spin-1/2 lepton and neutrino along with the $V-A$ nature of the decay, one can calculate the distribution of leptons [106], with the minimal assumption of azimuthal ϕ^*_ℓ symmetry, in terms of θ^*_ℓ:

$$\frac{1}{N}\frac{dN}{d\cos\theta^*_\ell} = f_{+1}\frac{3}{8}(1+\cos\theta^*_\ell)^2 + f_{-1}\frac{3}{8}(1-\cos\theta^*_\ell)^2 + f_0\frac{3}{4}\sin^2\theta^*_\ell, \qquad (6.2)$$

where N is the event yield. The distribution of $\cos\theta^*_\ell$ provides a handle to study the systematic uncertainty associated with the W polarization distribution in MC.

Each of the W bosons in $t\bar{t}$ events is produced via the decay $t \to bW^+$ or $\bar{t} \to \bar{b}W^-$. In the former decay, the left-handedness of the bottom quark, combined with its relatively small mass compared to the top quark has important

implications for the W^+ polarization distribution. In the limit that the bottom quark mass goes to zero, it will have negative helicity and conservation of angular momentum forbids the W from having positive helicity, i.e., $f_{+1} = 0$. The actual non-zero bottom mass is sufficiently low, though, such that f_{+1} is still small. A full calculation of the polarization fractions [107] results in the following values.

$$\begin{aligned} f_0 &= 0.687 \pm 0.005 \\ f_{-1} &= 0.311 \pm 0.005 \\ f_{+1} &= 0.0017 \pm 0.0001 \end{aligned} \tag{6.3}$$

These fractions were derived with the assumption that the top quarks are longitudinally unpolarized. This is a reasonable assumption given the parity conserving nature of the QCD production mechanism and consistent with recent measurements [108, 109]. Only a small, sub-percent polarization arises due to weak-interaction corrections [110], whose effect on this analysis is more than covered by the systematic uncertainty assigned to the polarization fractions.

For $\bar{t} \to \bar{b}W^-$ decays, the anti-bottom is right-handed and instead the negative helicity state of the W is heavily suppressed. In fact, the polarization fractions for W^- should be the same as those of W^+, but with f_{+1} and f_{-1} interchanged. However, because W^- decays to a left-handed lepton but W^+ decays to a right-handed anti-lepton, the distribution of $\cos\theta^*_\ell$ will be identical between the two.

The polarization fractions have been measured by multiple experiments [111, 112, 113, 114, 115], which have found them consistent with the above theoretical prediction. Given this agreement and the fact that the experimental uncertainties are over five times as large as the theoretical uncertainties, the predicted values from theory are used. An additional reason for this choice is that there is no potential for contamination from new physics, which could affect the experimentally measured values.

To obtain a systematic on the W polarization in $t\bar{t}$ events, a 5% variation is applied to the f_0 helicity polarization fraction. The f_{-1} fraction is correspondingly changed such that $f_{+1} + f_0 + f_{-1} = 1$ while the tiny f_{+1} fraction, which has extremely small uncertainty, is left unchanged. This 5% variation is roughly ten times larger than the theoretical error on these polarization fractions. Figure 6.6 shows the predicted angular distribution in the W frame and how it changes when applying this 5% variation.

Unlike in $t\bar{t}$, the polarization in $W+$jets events depends strongly on both the rapidity and transverse momentum of the W due to the EW production mechanism. There is also a small difference between the polarization of W^+ and W^-. For the high W-boson p_T (p_T^W) relevant for this analysis, left handed polarization should dominate. An analysis using an NLO QCD calculation [116] found the computation of the polarization fractions to be theoretically robust, higher-order

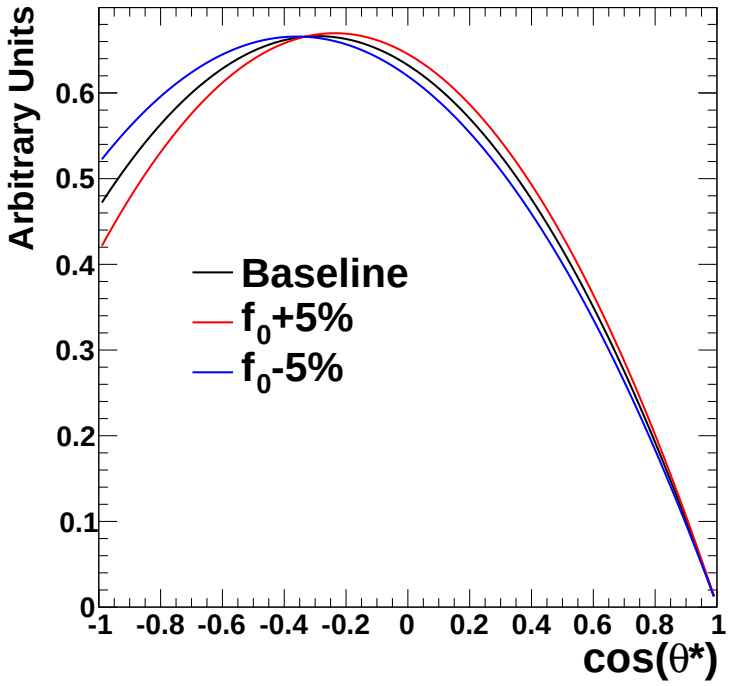

Figure 6.6: The $\frac{dN}{d\cos\theta^*_\ell}$ distribution in $t\bar{t}$ events from theory. The curves corresponding to 5% variations of f_0, used to derive the systematic uncertainty, are also shown.

QCD corrections to be small, and a theoretical uncertainty of around 10%. The computed polarization fractions were found to be consistent with measurements from both CMS [117] and ATLAS [118]. It was also found in [116] that the polarization fractions are also quite stable over p_T^W, with the left-handed piece on the order of 60% and rising with p_T^W, the right-handed piece staying constant around 20-25%, and the remaining longitudinal fraction dropping towards zero as p_T^W in-

creases. The above calculation used a center of mass energy of 7 TeV, but the conclusions were largely independent of this assumption and still hold at 8 TeV.

Since the W^+ and W^- have very similar polarization fractions, their decay leptons, which are respectively right and left-handed, should have opposite asymmetries in $\cos\theta^*_\ell$. If W production was charge symmetric, then the asymmetries would nearly cancel leaving $\cos\theta^*_\ell$ almost flat. However, W^+ production is more common [119] at the LHC, leading to a shift in the $\cos\theta^*_\ell$ distribution toward negative values in $W+$jets events.

In order to apply a systematic uncertainty to the prediction based on the uncertainty in the W polarization fractions, the fractions must first be quantified. Since the polarization in $W+$jets events depends on the W boson p_T, $|y|$, and charge, it is parametrized in bins of each of these variables. In particular, 3 bins of p_T corresponding to [100,300), [300,500), and [500,inf) GeV are used along with 3 bins of $|y|$ corresponding to [0,1), [1,2), and [2,5). Events with $p_T^W < 100$ GeV are ignored as they do not result in leptons or neutrinos with high enough p_T to pass the signal or control region selections. Additionally, the $p_T^W > 500$ GeV and $2 < |y| < 5$ bin for both W^+ and W^- is not used in the systematic variations due to a lack of events in this bin which causes an inability to accurately measure the polarization fractions.

Figures 6.7 and 6.8 show the $\frac{dN}{d\cos\theta^*_\ell}$ distributions in the W + jets simulation in the bins described above. In each bin a fit is performed to determine the polarization fractions. From these fits, a few general observations can be made. The helicity zero fraction decreases at high W-boson p_T, while the helicity -1 and $+1$ fractions gradually increase and remain relatively flat, respectively. At large rapidity the helicity -1 and $+1$ fractions increase and decrease, respectively, while the helicity zero fraction stays roughly the same. These observations are consistent with those made in the polarization calculations in Ref [116].

After fitting the angular distributions to obtain the polarization fractions, the systematic uncertainty on the LS prediction due to the W polarization uncertainties in W + jets is determined by varying the polarization fractions in each of the bins. Based on the theoretical uncertainties in Ref [116], 3 variations of the polarization fractions are chosen: 1) 10% variation to $f_{-1} - f_{+1}$ simultaneously for W^+ and W^-; 2) 5% variation of $f_{-1} - f_{+1}$ separately for W^+ and W^-; 3) 10% variation to the longitudinal polarization fraction f_0 simultaneously for W^+ and W^-. Figure 6.9 shows exactly the reweighting applied for the first variation type in the $300 < p_T^W < 500$ GeV, $0 < |y(W)| < 1$ bin separately for W^+ and W^-.

The uncertainties from these 3 variations are quite small across all signal bins, generally at the percent level or less, despite the significant polarization variations. This is because W + jets is such a small component of the background. The

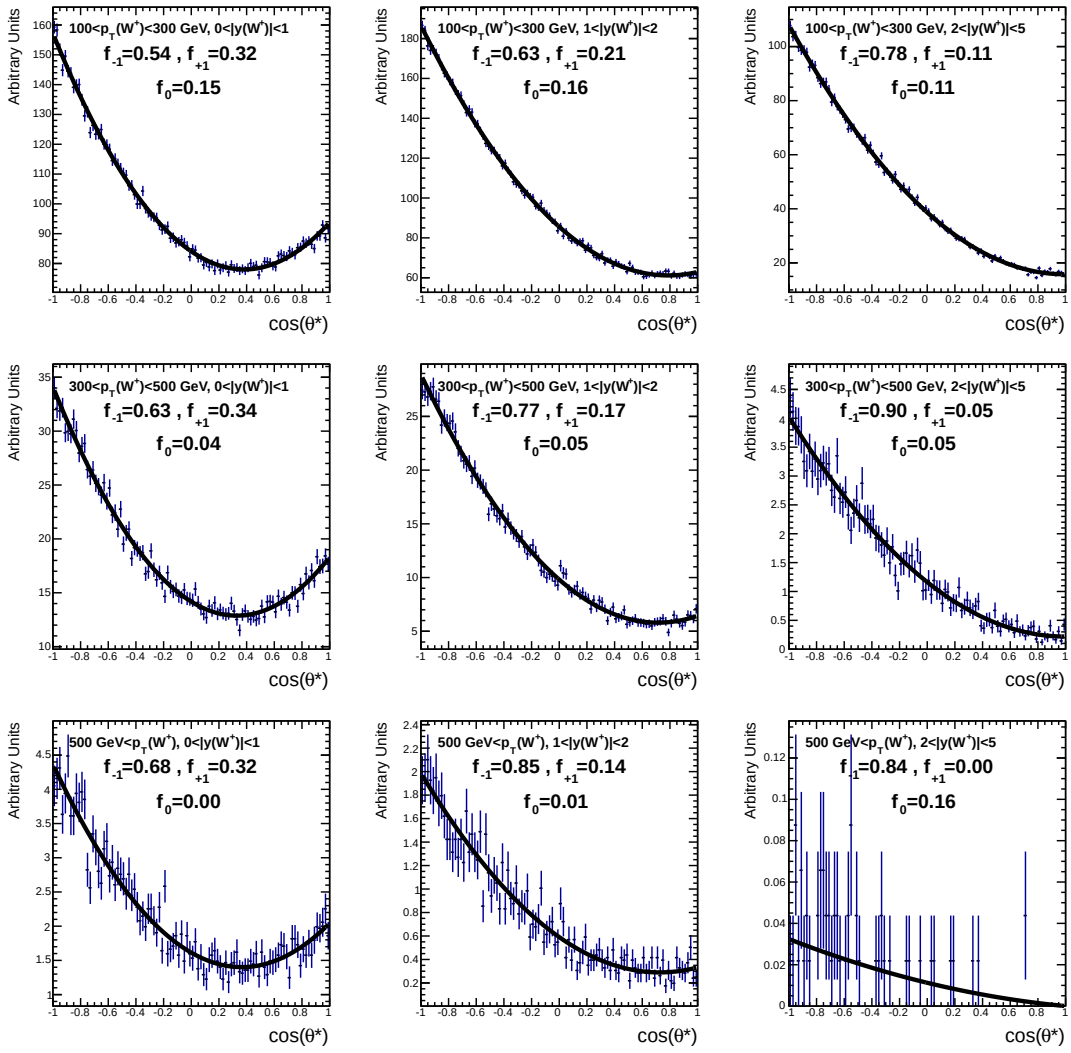

Figure 6.7: Fits to the simulated $\frac{dN}{d\cos\theta^*_\ell}$ distribution for W^+ in $W+$jets events in bins of W boson p_T and $|y|$. The helicity fractions in each bin are printed on each plot. For these plots the $\cos\theta^*_\ell$ was measured using the generator level momentum of the W^+ and its decay lepton.

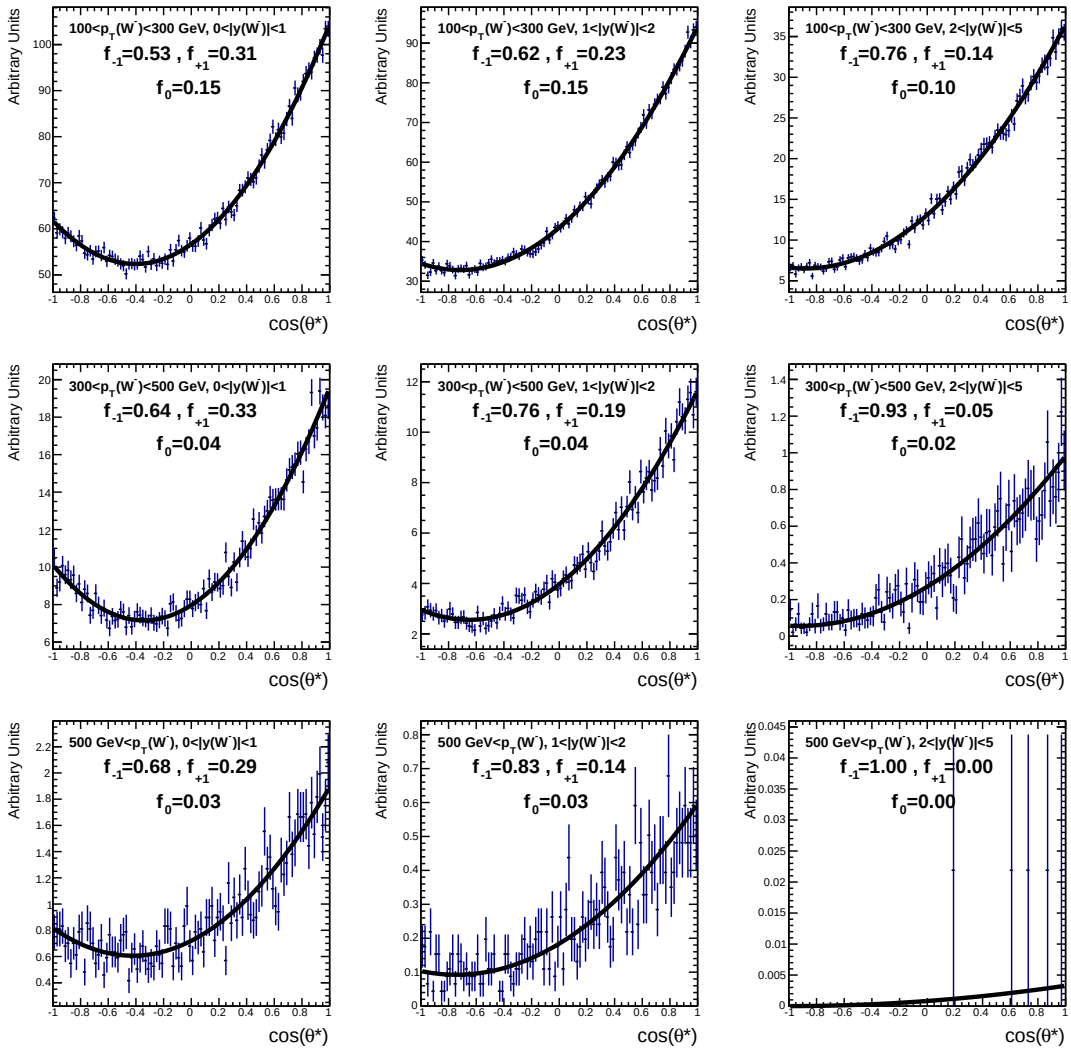

Figure 6.8: Fits to the simulated $\frac{dN}{d\cos\theta^*_\ell}$ distribution for W^- in $W+$jets events in bins of W boson p_T and $|y|$. The helicity fractions in each bin are printed on each plot. For these plots the $\cos\theta^*_\ell$ was measured using the generator level momentum of the W^- and its decay lepton.

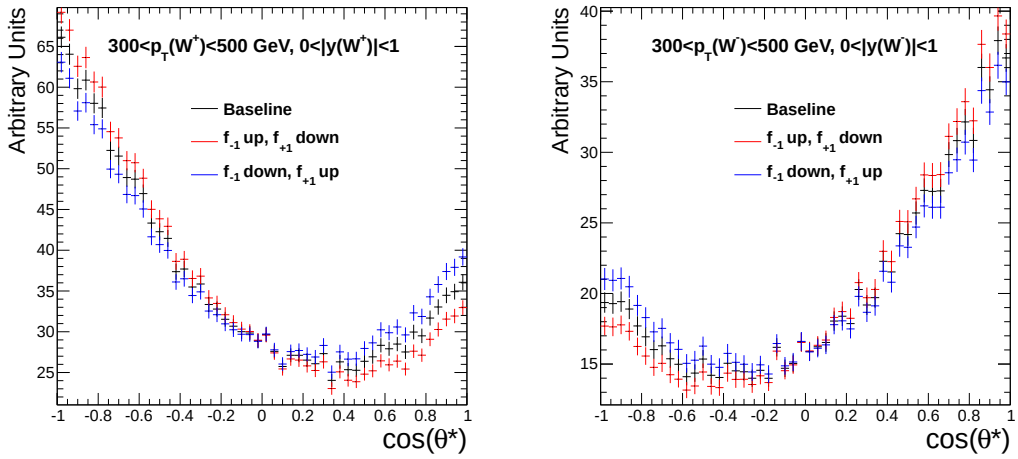

(a) (b)

Figure 6.9: The simulated $\frac{dN}{d\cos\theta^*_\ell}$ distribution in W + jets events for (a) W^+ and (b) W^- in the $300 < p_T^W < 500$ GeV, $0 < |y(W)| < 1$ bin. The distributions corresponding to a $\pm 10\%$ variation of $f_{-1} - f_{+1}$, which is used in determining the systematic uncertainty, are also shown.

procedure used to derive the uncertainties from the W polarization variations is described in Sec. 6.1.3.

6.1.3 Systematic Uncertainties

There are several distinct systematic effects that could bias the single lepton background prediction from the LS method. For all of these effects, the bias enters because the simulation, in which the $\kappa_{\rm LS}$ factors are derived, does not match the data. To gauge this bias, a given effect is varied by its uncertainty and the change

in κ_{LS} is noted. The relative systematic uncertainty is

$$\text{Relative Uncertainty} = \frac{|\kappa_{\mathrm{LS}}(\text{Nominal}) - \kappa_{\mathrm{LS}}(\text{Variation})|}{\kappa_{\mathrm{LS}}(\text{Nominal})}. \tag{6.4}$$

For sources of uncertainty which correspond to multiple variations of κ_{LS}, e.g., positive and negative variations of a systematic effect, the systematic uncertainty on κ_{LS} is conservatively taken to be the maximum of these variations and treated as symmetric. The systematic uncertainty is derived separately for each signal region of the analysis. Although, this relative uncertainty is derived from the change in κ_{LS}, it applies equally well to the final prediction from the LS method.

The sources of systematic uncertainty along with their treatment are:

- **Jet and $\not\!\!E_{\mathrm{T}}$ energy scale:** This is a dominant uncertainty for the lepton spectrum method. The uncertainty on the jet and $\not\!\!E_{\mathrm{T}}$ energy scales is highly correlated, and is therefore treated as one source of uncertainty. Because the LS method uses lepton p_T to predict $\not\!\!E_{\mathrm{T}}$, a shift in the $\not\!\!E_{\mathrm{T}}$ scale changes κ_{LS} by altering the numerator of Eq. 6.1 but leaving the denominator unchanged. This uncertainty is measured by varying the energies of all jets and unclustered calorimeter deposits in each event by $\pm 1\sigma$ of their uncertainty.

- **W polarization in $t\bar{t}$:** A 5% variation to the f_{-1} and f_0 W helicity fractions is applied. This 5% variation is roughly ten times larger than the theoretical error on these polarization fractions. More details are described in Sec. 6.1.2.

- W **polarization in W+jets:** 3 variations of the polarization fractions are used: 1) 10% variation to $f_{-1} - f_{+1}$ simultaneously in W^+ and W^-, 2) 5% variation to $f_{-1} - f_{+1}$ separately for W^+ or W^-, 3) 10% variation to the longitudinal polarization fraction, f_0, simultaneously in W^+ and W^-. These variations are applied in bins of $p_T(W)$ and rapidity of the W. More details on the procedure and the specifics of the binning are given in Sec. 6.1.2.

- $\sigma(W)$**:** While the inclusive W+jets cross section is well known theoretically and experimentally, the cross section for $W+ \geq 6$ jets is much less constrained. The uncertainty on the $W +$ jets cross section is measured using $Z +$ jets events passing the same H_T and N_{j} selection criteria by comparing the event yield in data and MC. More details are given in the subsection below. The contribution of $W + b\bar{b}$ is particularly uncertain, so an additional uncertainty from a 100% variation of the $W + b\bar{b}$ cross section is included.

- $\sigma(t\bar{t})$**:** The $t\bar{t}$ production cross section is varied by its theoretical uncertainty, taken from Ref. [104].

- **Single top cross sections:** The single top cross sections are varied according to the uncertainty given in [104]. The t-channel, s-channel and tW components are varied up or down simultaneously.

- **Lepton efficiency vs p_T:** This takes into account uncertainties arising from data to simulation differences in the lepton reconstruction and identification and is measured by varying the electron and muon efficiencies. The lepton efficiency is changed according to the data/MC ratios given in Ref. [120], which are generally within a few percent of unity across the full range of lepton p_T. This leads to a small uncertainty in the prediction in both the muon and electron channels.

- **Z + jets background:** The contribution of Z + jets events to the lepton p_T spectrum is assigned a 100% uncertainty. The large relative uncertainty is intended to cover the poorly known Z plus many jets and $Z + b\bar{b}$ cross sections as well as uncertainty on reconstruction and selection inefficiencies which allow $Z \to \ell\ell$ events to enter the control sample. This large relative uncertainty, however, translates to a very small uncertainty on the total prediction due to the tiny Z + jets contribution to the control sample.

- **Muon p_T scale:** Analogous to changing the $\not\!\!E_{\mathrm{T}}$ scale, a shift in the muon p_T scale would change κ_{LS} by altering the denominator of Eq. 6.1 but leaving the numerator unchanged. The systematic uncertainty due to the muon p_T scale is measured using an ensemble of mock data samples drawn from $t\bar{t}$ simulation, where the curvature corrections in each mock data sample

are smeared according to the uncertainties with which these corrections are measured in Ref. [121]. See the subsection at the end of this section for more details.

- **Scale factor statistical uncertainty:** The statistical uncertainty on the measurement of the κ_{LS} factors are included in the systematic uncertainties.

Table 6.1 summarizes the systematic uncertainties associated with the single lepton background prediction for the three search H_T thresholds.

Systematic Uncertainty on the $W+$jets cross section

The $W+$jets cross section uncertainty is measured by comparing data to simulation in a $Z+$jets sample. $Z+$jets makes a reasonable proxy for $W+$jets events because of the similarity of their production diagrams. This measurement is performed in a baseline sample with $N_{\mathrm{j}} \geq 4$, $H_T > 500$ GeV, exactly two selected muons or electrons, and no additional leptons passing the veto selection. Events are required to pass the lepton+H_T cross triggers and have leading lepton $p_T > 50$ GeV in order to be on plateau for the lepton leg of these triggers. Figure 6.10 shows the dilepton mass distribution in events with $N_{\mathrm{j}} \geq 4$, $N_{\mathrm{j}} \geq 6$, or $N_{\mathrm{j}} \geq 4$ and $N_b \geq 2$. The $N_{\mathrm{j}} \geq 6$ and $N_b \geq 2$ selection is not used because too few events pass this selection for a useful data/simulation comparison.

Table 6.1: Systematic uncertainties, in percent, in bins of $\not\!\!E_{\mathrm{T}}$ for the single lepton background prediction for $H_T > (500/750/1000)$ GeV and $N_{\mathrm{j}} \geq 6$. Each uncertainty is expressed as the change in the ratio of predicted to true number of events (evaluated using simulated events).

$\not\!\!E_{\mathrm{T}}$ bin:	$[150, 250)$	$[250, 350)$	$[350, 450)$	≥ 450 GeV
$\not\!\!E_{\mathrm{T}}$ and jet energy scale	2.5/2.1/1.4	7.7/7.0/9.1	10/12/7.1	28/28/26
W polarization in $t\bar{t}$	2.9/2.9/2.9	3.9/4.0/3.2	3.1/2.4/2.2	3.4/3.7/4.4
W polarization in $W+$jets	$< 0.1/0.1/0.1$	0.2/0.4/0.7	0.5/0.4/0.8	2.0/2.1/3.0
$\sigma(t\bar{t})$	0.9/1.5/1.3	0.3/0.9/1.6	0.4/0.3/2.1	2.8/2.8/2.6
$\sigma(W)$	0.4/0.5/0.3	0.2/0.3/1.6	1.3/0.6/2.3	2.1/1.8/2.1
Single top cross section	0.6/1.9/0.1	0.1/1.0/2.3	1.8/0.1/0.1	$< 0.1/< 0.1/< 0.1$
Lepton efficiency (μ) vs. p_T	0.5/0.5/0.5	0.5/0.5/0.6	0.5/0.5/0.8	0.2/0.2/0.7
Lepton efficiency (e) vs. p_T	0.2/0.2/0.2	0.2/0.2/0.2	0.2/0.2/0.1	0.3/0.3/0.2
$Z+$jets background	0.3/0.4/0.4	0.4/0.6/0.1	1.2/1.2/0.6	$0.2/0.3/< 0.1$
μ p_T scale	$< 0.1/< 0.1/< 0.1$	0.1/0.4/0.8	1.4/1.3/3.4	2.7/1.5/2.5
Total (excluding scale factors)	4.0/4.4/3.6	8.7/8.2/10	11/12/9.5	29/29/27
MC statistics (scale factors)	3.3/5.2/8.8	8.7/11/17	22/24/37	34/36/49
Total	5.2/6.8/9.5	12/14/20	25/27/38	45/46/56

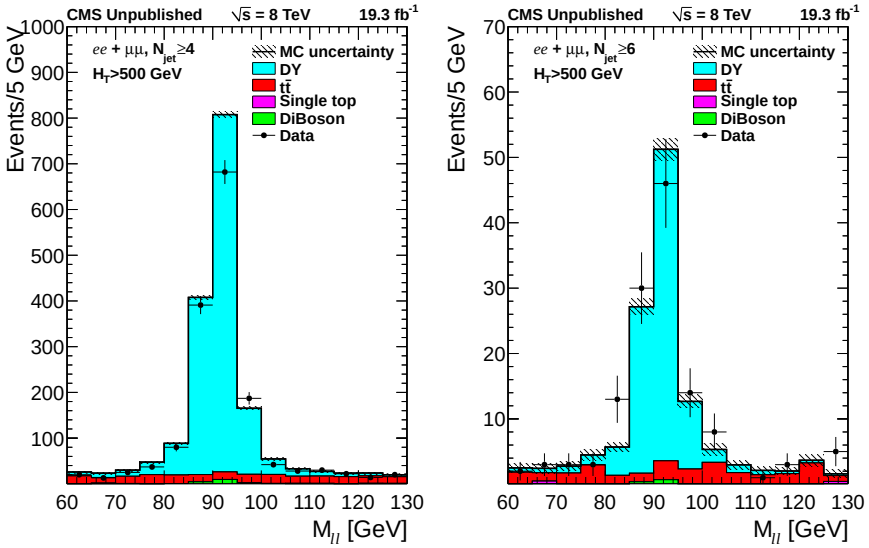

(a) (b)

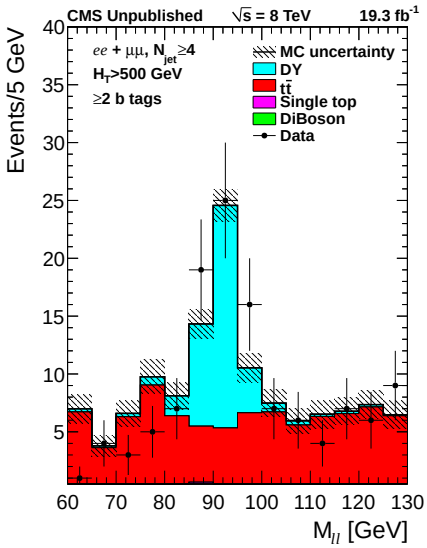

(c)

Figure 6.10: Dimuon and dielectron mass distribution after an $H_T > 500$ GeV requirement for: (a) $N_{\mathrm{j}} \geq 4$, (b) $N_{\mathrm{j}} \geq 6$, and (c) $N_{\mathrm{j}} \geq 4$ and $N_b \geq 2$. The uncertainties shown for both simulation and data are statistical only.

Table 6.2: Yields and ratios in data and simulation in the dilepton mass window of [80,100] GeV. A baseline cut of $H_T > 500$ GeV is applied.

N_{j}	N_b	Data	DY Simulation	non-DY Simulation	Data/Simulation
≥ 4	≥ 0	1340	1382.5 ± 7.9	86.4 ± 4.1	0.91 ± 0.03
≥ 6	≥ 0	103	87.8 ± 2.0	9.0 ± 1.4	1.07 ± 0.12
≥ 4	≥ 2	67	33.7 ± 1.2	23.9 ± 2.2	1.28 ± 0.26

Table 6.2 lists the ratios of data to simulated Drell-Yan event yields in the dilepton mass window of [80,100] GeV. The expected non-DY yield from simulation is subtracted from data before dividing by the expected DY yield in simulation. When determining the uncertainty on κ_{LS}, the uncertainty on the $W+$jets cross section was taken from the $N_{\mathrm{j}} \geq 6$, $N_b \geq 0$ line of Tab. 6.2, namely $\sqrt{7^2 + 12^2} = 14\%$.

Systematic Uncertainty from the Muon p_T Scale

Muon p_T scale uncertainties are obtained from the study of the q/p_T distributions of muons in Z events described in Ref. [121]. This study compares the q/p_T distributions of positive and negative muons. A fixed bias $q/p_T \rightarrow q/p_T + \kappa$ is injected, and the χ^2 between the p_T distribution of the positively and negatively charged muons is computed. The curvature bias is the value of κ that minimizes this χ^2, and its distribution as a function of (η, ϕ) is shown in Fig. 6.11.

Toy studies are performed to understand the systematic error on κ_{LS} due to the muon p_T scale uncertainty. A total of 1000 toy samples from $t\bar{t}$ simulation

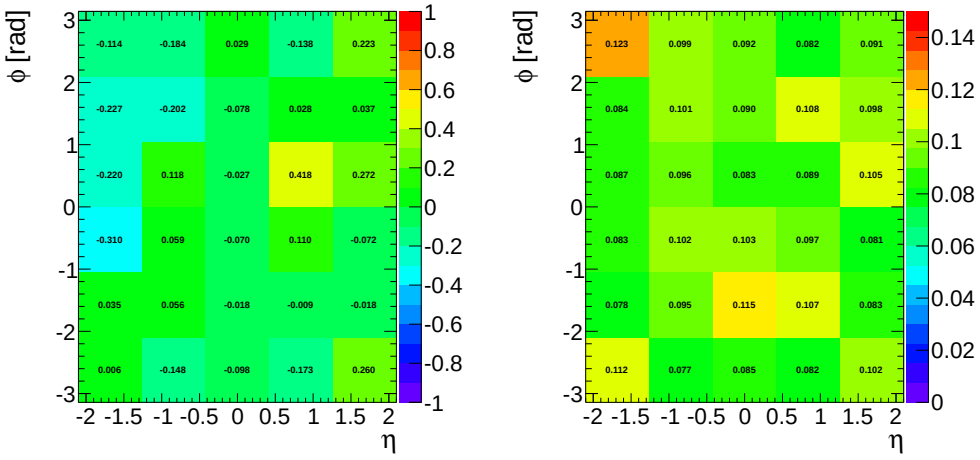

(a) (b)

Figure 6.11: Muon curvature bias (a) and its error (b).

scaled to the data luminosity are used. To reduce statistical fluctuations in the results, events with muons and electrons with $|\eta| < 2.4$ and no N_b requirement are used. For each sample, the curvature bias in each (η, ϕ) bin is smeared by its error. The resulting distribution is used to correct the p_T distribution of each muon and electron in the toy sample. The relative difference between the uncorrected yield and the mean of the distribution of yields across the ensemble of toy samples is taken as an uncertainty on the muon p_T spectrum and hence on κ_{LS}.

In addition to being statistically limited, this method is also affected by the precision with which the curvature bias was determined. As a cross-check, the

same analysis is performed with a constant curvature bias of $0.05c/$ TeV. The more conservative result from the toy procedure is used as the systematic.

6.2 Dilepton and τ-lepton Backgrounds

Because the LS method does not estimate the backgrounds from events with dileptons or τ-leptons, they must be estimated separately. This section describes the procedures used to predict these backgrounds and their associated systematic uncertainties. A requirement of $N_b = 2$ is made throughout this section.

The tail of the $\not\!\!E_{\mathrm{T}}$ distribution in reconstructed single lepton events has a small but non-negligible contribution from dilepton and tau events. The prediction of these backgrounds can be broken down into two techniques, one data-driven for the predictions involving leptonic (denoted τ_ℓ) and hadronic (denoted τ_{h}) tau decays, the other simulation based for the prediction of dilepton events. These backgrounds can be subdivided into four distinct categories:

- **Dilepton:** Events with two promptly produced leptons.
- **Single τ_ℓ:** Events with one tau which decays leptonically and no other taus or leptons.
- **$\ell + \tau_{\mathbf{h}}$:** Events with one hadronically decaying tau and one lepton. The lepton can be promptly produced or from a leptonic tau decay.

- $\ell + \tau_\ell$**:** Events with one leptonically decaying tau and an additional lepton. The lepton can be promptly produced or from a leptonic tau decay.

The estimates of these backgrounds utilize the following control samples: reconstructed dilepton events to predict dilepton, $\ell + \tau_{\rm h}$, and $\ell + \tau_\ell$ and reconstructed single lepton events to predict the single τ_ℓ background.

6.2.1 Dilepton: Lost and Ignored

There are two basic ways in which dilepton events can contribute to the selected single lepton signal sample. These ways, via ignored and lost leptons, are similar and thus treated together in the background prediction. Ignored lepton events are those where both leptons are reconstructed, but one of the leptons is not identified by the lepton veto selection. Because the ignored lepton is reconstructed, it has its energy properly accounted in the $\not\!\!E_{\rm T}$ calculation. However, these events do have an extra neutrino associated with the second lepton which changes the $\not\!\!E_{\rm T}$ distribution compared to true single lepton events. In lost lepton events, one lepton is not reconstructed, generally due to being outside the η or p_T acceptance of the detector. In these events, the p_T of the lost lepton is absent from the $\not\!\!E_{\rm T}$ calculation. However, for the majority of these events the contribution to the $\not\!\!E_{\rm T}$ from the lost lepton is small compared to the contribution from the two neutrinos.

The prediction uses a control sample of events which have two selected leptons, each with $p_T > 20$ GeV, no additional leptons passing the veto selection, $N_{\rm j} \geq 6$, and $\not\!\!E_{\rm T} > 100$ GeV. Data events are required to pass the same lepton+H_T +$\not\!\!E_{\rm T}$ cross-triggers as the single lepton signal sample. To reject $Z+$jets, for ee and $\mu\mu$ events there is a veto on invariant dilepton masses between 71 and 111 GeV. The $\not\!\!E_{\rm T}$ requirement is placed in order to be on the efficiency plateau for the $\not\!\!E_{\rm T}$ leg of the triggers and also serves to further suppress $Z+$jets events.

Because lost and ignored dilepton events contain leptons that are either not reconstructed or in an extreme kinematic regime, i.e., very low p_T or high η, it is rather difficult to model them properly using a data control sample. This difficulty motivates the use of the $\not\!\!E_{\rm T}$ shapes of these backgrounds from simulation. Since ignored and lost lepton events come from the same SM processes as selected dilepton events, the prediction is obtained by scaling the simulated $\not\!\!E_{\rm T}$ distribution of these backgrounds to the ratio of yields in data over simulation in the above control sample. The $\not\!\!E_{\rm T}$ distributions in data and simulation in this dilepton control sample, with the integral of the simulation scaled to that of the data, are shown in Fig. 6.12. The resulting data/simulation normalization ratios are 0.73 ± 0.18, 0.46 ± 0.20, and 0.44 ± 0.32 for H_T >500, 750, and 1000 GeV, respectively. Using these ratios to scale the simulated $\not\!\!E_{\rm T}$ spectrum, the lost and ignored dilepton predictions are listed in Table 6.3 and can be seen in figure 6.13.

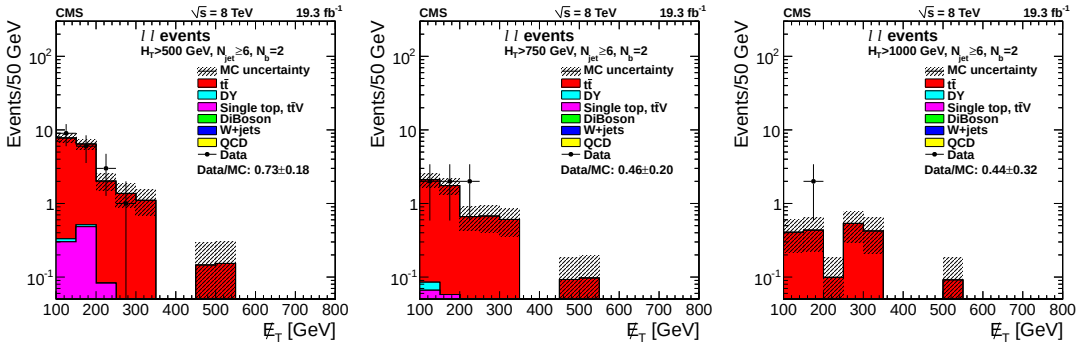

(a) (b) (c)

Figure 6.12: $\not{E}_{\mathrm{T}}$ distribution of the $N_{\mathrm{j}} \geq 6$ and $N_b = 2$ dilepton control sample in data and simulation, with the integral of the simulation scaled to that of the data, for the different H_T thresholds.

Table 6.3: Predicted yields for the ignored and lost lepton backgrounds for the different H_T thresholds, $N_{\mathrm{j}} \geq 6$, and $N_b = 2$. The first uncertainty is statistical and the second is systematic.

	Prediction		
$\not{E}_{\mathrm{T}}$ bin [GeV]	$H_T > 500$	$H_T > 750$	$H_T > 1000$ GeV
$[150, 250)$	12.52±1.38±3.41	4.02±0.63±1.76	1.34±0.34±1.00
$[250, 350)$	2.56±0.65±0.75	1.30±0.38±0.60	1.13±0.35±0.86
$[350, 450)$	0.63±0.30±0.22	0.40±0.19±0.20	0.19±0.12±0.15
$[450, \infty)$	0.10±0.09±0.05	0.06±0.05±0.04	0.05±0.05±0.04

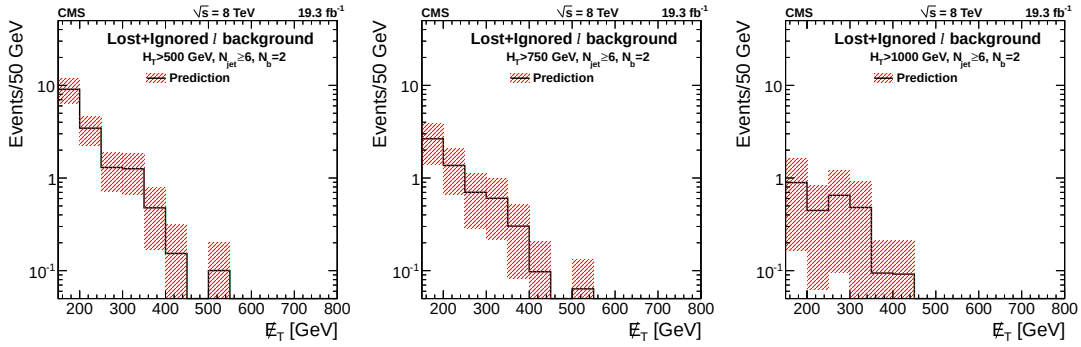

(a) (b) (c)

Figure 6.13: Predicted $\not\!\!E_{\mathrm{T}}$ distribution of lost and ignored lepton events for $N_{\mathrm{j}} \geq 6$ and $N_b = 2$. The errors shown include the systematic uncertainties.

Systematic Uncertainties on the Lost and Ignored Dilepton Prediction

The systematic uncertainty on the lost and ignored dilepton prediction comes from the following sources, described in more detail below.

- The relative statistical uncertainty on the data to simulation scale factor.
- The uncertainty on the pile-up distribution.
- The uncertainty on the lepton selection efficiencies.
- The uncertainty on the trigger efficiency.
- The uncertainty on the top-quark p_T spectrum.

Unlike the data-driven methods used for predicting the other backgrounds in this analysis, this method can be more heavily biased by assumptions in the simulation, i.e., the last four items in the above list.

The uncertainty on the prediction due to the uncertainty on the pile-up distribution is important to consider because lepton identification efficiencies and possibly the N_{j} and N_b distributions depend on the amount of pile-up. This uncertainty is derived by first recalculating the weights used to scale the simulated pile-up distribution to match that of the data. The recalculation is done after increasing and decreasing the inelastic pp cross section, which is used to calculate the pile-up distribution in data, by 5%. For each of these variations, the prediction is re-calculated by re-determining the data to simulation ratio in the dilepton control sample as well as the true $\not\!\!E_{\mathrm{T}}$ distribution in simulation. For each signal bin, the larger change in the predicted yield from the two variations is taken as a systematic uncertainty. This systematic uncertainty is less than 12% for the lower $\not\!\!E_{\mathrm{T}}$ signal bins but is on the order of 40% for the highest bin due to very limited statistics in that bin.

The difference in lepton selection efficiencies between data and simulation is an important effect for this prediction because the signal region and control samples are affected by it in different ways. For example, a decrease in the lepton efficiency will decrease the yield in the dilepton control sample, but potentially increase the

yield in the single lepton signal region though feed-down. As found in Ref. [120], the lepton efficiencies in data and simulation are close to 1 with small statistical uncertainty and a 2% systematic uncertainty. To estimate the uncertainty due to a possible lepton efficiency difference in data and simulation, the simulated efficiencies are increased and decreased by 2%. For each signal bin, the larger change in the predicted yield from the two variations is taken as a systematic uncertainty. The uncertainty across the signal bins varies from roughly 2-8%

The lepton leg of the cross-triggers used to select the control and signal samples in this analysis is roughly 94% efficient on average. The dilepton events used in this prediction are nearly 100% efficient for the lepton leg of the trigger because of the presence of two leptons. However, lost and ignored dilepton background events will be less efficient due to the presence of only one selected lepton. This means there is some trigger inefficiency due to the lepton leg that is not accounted for in the data/MC ratio in the dilepton control sample. To account for this potential bias of the prediction, a 6% systematic uncertainty, equal to the average lepton trigger leg inefficiency, is assigned to the prediction.

In order to measure the uncertainty due to the top p_T spectrum, the W-boson p_T spectrum in $t\bar{t}$ simulation is varied and compared to data. The W-boson p_T in an event is reconstructed from the vector sum of the lepton $\vec{p}_T$ and $\vec{\not{E}}_{\mathrm{T}}$. This test uses a single lepton sample with $H_T > 500$ GeV, $N_{\mathrm{j}} \geq 4$, $N_b \geq 2$,

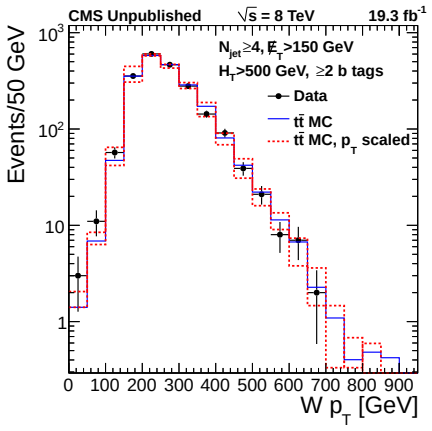

Figure 6.14: W-boson p_T distribution in data and simulation for a single lepton sample with requirements $N_{\mathrm{j}} \geq 4$, $N_b \geq 2$, $H_T > 500$ GeV, and $\not\!\!E_{\mathrm{T}} > 150$ GeV. The 1 sigma variations in the simulated spectrum are shown as red dashed lines.

and $\not\!\!E_{\mathrm{T}} > 150$ GeV. The $\not\!\!E_{\mathrm{T}}$ and H_T requirements are set in order to be on the efficiency plateau for the signal triggers. The b-tag multiplicity requirement ensures a highly $t\bar{t}$ dominated sample. To vary the W-boson p_T spectrum in simulation, the W p_T of each event is multiplied by a scale factor. The simulated spectrum is varied up and down until the normalized χ^2 between the data and simulated distributions increases by 1. The variation factors that achieve this are 1.023 and 0.951. The data and resulting simulated W p_T spectra are shown in Fig. 6.14. The systematic uncertainty on the prediction is obtained from the maximum change in the prediction after re-weighting the lost and ignored lepton events in $t\bar{t}$ simulation to match the two varied W p_T spectra. This systematic uncertainty tends to be in the range of 10-25%.

Table 6.4: Systematic uncertainties, in percent, on the lost and ignored lepton prediction for H_T >(500/750/1000) GeV, $N_\mathrm{j} \geq 6$, and $N_b = 2$.

$\not\!\!E_\mathrm{T}$ bin:	[150,250)	[250,350)	[350,450)	$\geq$ 450 GeV
PU	2.6/2.6/6.7	0.5/4.0/4.4	4.1/4.2/12	42/42/47
top quark p_T	8.2/3.6/0.9	13/14/13	24/24/33	12/12/15
lepton efficiency	4.7/4.7/4.6	6.1/6.2/4.6	2.1/2.1/2.3	8.0/8.0/2.0
trigger efficiency	6.0/6.0/6.0	6.0/6.0/6.0	6.0/6.0/6.0	6.0/6.0/6.0
data/simulation scale	25/43/73	25/43/73	25/43/73	25/43/73
Total	28/44/74	29/46/75	35/50/81	51/62/88

The systematic uncertainties in all signal bins are shown in Table 6.4.

6.2.2 Hadronic tau

Due to the neutrinos from tau decays, events with tau leptons have an enhanced $\not\!\!E_\mathrm{T}$ spectrum. In $\ell + \tau_\mathrm{h}$ events, the hadronic tau decay contributes to the $\not\!\!E_\mathrm{T}$ via a neutrino but potentially also to the jet multiplicity. To estimate the $\not\!\!E_\mathrm{T}$ in these events, a similar dilepton control sample to the one in Sec. 6.2.1 is used, but with a few differences. Namely, data events are also selected with the lepton+H_T triggers, the N_j threshold is reduced by one, the H_T threshold is loosened to 425 GeV, and the $\not\!\!E_\mathrm{T}$ requirement is dropped for $e\mu$ events and set to 40 GeV for ee and $\mu\mu$ events in order to suppress $Z +$ jets. The H_T and N_j requirements are relaxed from the baseline signal selection for reasons described below. The requirement on H_T is placed to retain trigger efficiency.

The concept of the prediction is to separately use each lepton in a control sample event to emulate a hadronic tau decay via p_T-dependent tau-jet response functions derived in simulation. These functions correspond to the p_T of the tau-jet, i.e., the jet resulting from the hadronic tau decay, as a fraction of the tau p_T and are shown in Fig. 6.15. The templates are derived in a simulated $t\bar{t}$ sample with a selection similar to the signal selection to minimize bias. In particular, one W is required to decay to an e or μ with true $p_T > 20$ GeV and $|\eta| < 2.4$ and the other W is required to decay to a τ with $|\eta| < 2.4$ which decays to hadrons. If a generator level tau is matched to a reconstructed jet within $\Delta R < 0.2$ and the jet has fewer than 11 associated PF charged candidates, the ratio of the reconstructed jet p_T and generator-level tau p_T enters the template. The requirement on the number of PF charged candidates helps reject overlapping jets that are not related to the tau decay.

For a lepton in the dilepton control sample, a random number r_j is picked from the appropriate tau-jet response function. To simulate the neutrino from the tau decay, $(1 - r_j)\vec{p}_T^{\,\ell}$ is added vectorially to the $\vec{\not{E}}_{\mathrm{T}}$ already present in the event. The p_T of the emulated jet, $r_j p_T^{\ell}$, is then counted among the jets and added to the H_T calculation, provided it passes the jet p_T threshold of 40 GeV. The event is then required to pass the signal selection. In order to get a more precise prediction, the τ_{h} emulation is performed a hundred times for each lepton in each event and then

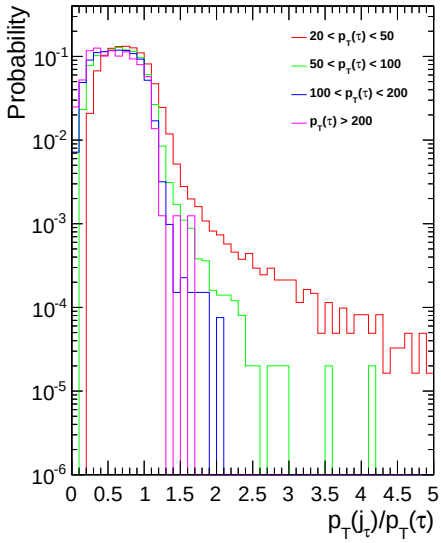

Figure 6.15: Tau-jet response functions in $p_T(\tau)$ bins.

averaged to determine the contribution of that event. Applying this procedure to the dilepton control sample provides the raw predicted $\not\!\!E_{\mathrm{T}}$ spectrum. The statistical uncertainty on the prediction comes from the square root of the sum of the squares of the contributions from each event in the control sample.

In order to correct the raw predicted $\not\!\!E_{\mathrm{T}}$ spectrum in data, two ratios derived in simulation, called α and κ, are used. These factors are determined and applied in the same way for the $\ell + \tau_{\mathrm{h}}$, $\ell + \tau_\ell$, and single τ_ℓ predictions.

The scale α is the ratio of the simulated signal yield of $\ell + \tau_{\mathrm{h}}$ events in the range $100 \leq \not\!\!E_{\mathrm{T}} < 250$ GeV to the raw prediction in simulation of the same range:

$$\alpha = \frac{\ell + \tau_{\mathrm{h}} \text{ signal yield in } 100 \leq \not\!\!E_{\mathrm{T}} < 250 \text{ GeV}}{\text{raw prediction in } 100 \leq \not\!\!E_{\mathrm{T}} < 250 \text{ GeV}} \tag{6.5}$$

This is done for each H_T requirement and normalizes the raw prediction at low $\not\!\!E_{\mathrm{T}}$. α is taken from simulation because many of the systematics inherent to the simulation cancel out in the ratio. The α factor takes into account many different effects, but for this background component, the tau to hadrons branching ratio is of chief importance with lepton acceptance and efficiency effects also relevant.

The second scale which corrects the prediction is a κ-factor. These κ-factors are the ratio in simulation of the $\ell + \tau_{\mathrm{h}}$ signal yield within a particular $\not\!\!E_{\mathrm{T}}$ bin to the number of events in the prediction in that bin obtained by multiplying the raw prediction by the α factor:

$$\kappa = \frac{\ell + \tau_{\mathrm{h}} \text{ signal yield in } \not\!\!E_{\mathrm{T}} \text{ bin}}{\alpha \times \text{ raw prediction in } \not\!\!E_{\mathrm{T}} \text{ bin}}$$

The κ-factors correct for potential systematic biases in the procedure, such as p_T or η dependent lepton efficiency or biases in the tau to hadrons decay response templates. These κ-factors can have large statistical errors in the most stringently selected signal regions due to the small event yields. The systematic uncertainty on κ is taken to be $100\% \cdot (1 - \kappa)$. The κ-factors for each of the three H_T selections are shown in Fig. 6.16.

To obtain the final data driven prediction, the raw $\not\!\!E_{\mathrm{T}}$ prediction from data in each signal bin is multiplied by the appropriate α and κ:

$$\mathrm{Prediction}(H_T, \not\!\!E_{\mathrm{T}}) = \mathrm{Raw\_Prediction}(H_T, \not\!\!E_{\mathrm{T}}) \times \alpha(H_T) \times \kappa(H_T, \not\!\!E_{\mathrm{T}})$$

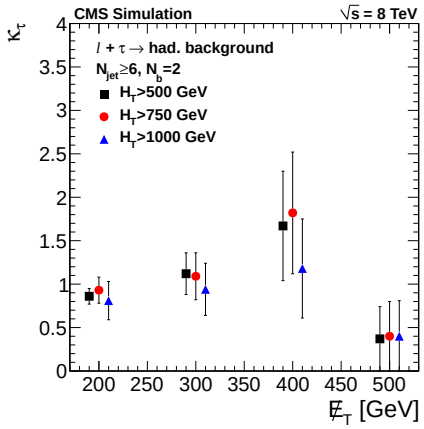

Figure 6.16: κ-factors used in the $\ell + \tau_{\mathrm{h}}$ prediction for $N_{\mathrm{j}} \geq 6$ and $N_b = 2$. The error bars denote the statistical uncertainty.

In the $\ell + \tau_{\mathrm{h}}$ prediction, the emulated hadronic tau decays do not contribute the number of b-tagged jets. The fact that actual hadronic tau decays can be b tagged is accounted for in the α and κ factors described above.

The systematic error on the prediction from the α and κ factors comes from a combination of the statistical precision on their calculation and any biases that are encoded in the deviation of the κ-factors from one. This error is determined in the same way for the $\ell + \tau_{\mathrm{h}}$, $\ell + \tau_{\ell}$, and single τ_{ℓ} predictions. Systematic errors are calculated as:

$$\frac{\text{systematic from } \alpha, \kappa}{\text{prediction}} = \frac{1}{\kappa} \cdot (\delta\kappa_{\text{stat.}} \oplus 100\% \cdot (1 - \kappa)) \oplus \frac{1}{\alpha} \cdot \delta\alpha_{\text{stat.}}$$

An additional systematic uncertainty on this prediction is assigned to gauge the uncertainty on the tau-jet response templates. This systematic is determined from the change in the prediction after using response templates determined when loosening the cut on the matched jet's PF charged candidate multiplicity from less than 11 to less than 16. This systematic is less than 10% for all signal regions with the exception of one very low statistics $H_T > 1000$ GeV and $N_{\mathrm{j}} \geq 6$ $\not\!\!E_{\mathrm{T}}$ bin.

Because this background prediction uses a dilepton control sample to estimate a background with only one lepton in the final state, the α factor must be corrected to account for the inefficiency of the lepton leg of the triggers for the sample in the numerator of Eq. 6.5. The simulated $\ell + \tau_{\mathrm{h}}$ yield is therefore reduced by 6% to account for this, directly resulting in the same reduction of α. An uncertainty of 3% is assigned to the prediction to account for the potential spread in the trigger inefficiency due to the $|\eta|$ dependent muon trigger efficiency.

The simulated yields and predictions used to obtain the κ factors and the predictions in data for $\ell + \tau_{\mathrm{h}}$ events are listed in Tables 6.5, 6.6, and 6.7 for the H_T requirements of 500, 750, and 1000 GeV, respectively. In these tables, the simulated yields and predictions have been scaled by the α factors of 0.54 ± 0.04, 0.51 ± 0.06, and 0.59 ± 0.12 for the H_T >500, 750, and 1000 GeV selections, respectively. Closure tests in simulation showing the predicted $\not\!\!E_{\mathrm{T}}$ spectrum over

Table 6.5: $\ell + \tau_{\mathrm{h}}$: Predicted yields for H_T >500 GeV, $N_{\mathrm{j}} \geq 6$, and $N_b = 2$. This selection corresponds to an α factor of 0.54 ± 0.04.

$\not\!\!E_{\mathrm{T}}$ bin [GeV]	Simulated Yield	Simulated Prediction	κ	Data-driven Prediction
$[150, 250)$	23.62±2.19	27.34±1.51	0.86±0.09	20.57±2.46±4.25
$[250, 350)$	7.09±1.34	6.32±0.67	1.12±0.24	4.63±1.22±1.18
$[350, 450)$	2.11±0.66	1.26±0.27	1.67±0.63	1.39±0.63±0.78
$[450, \infty)$	0.23±0.21	0.61±0.24	0.37±0.37	$0.05^{+0.20+0.39}_{-0.04-0.05}$

Table 6.6: $\ell + \tau_{\mathrm{h}}$: Predicted yields for H_T >750 GeV, Njetsix, and $N_b = 2$. This selection corresponds to an α factor of 0.51 ± 0.06.

$\not\!\!E_{\mathrm{T}}$ bin [GeV]	Simulated Yield	Simulated Prediction	κ	Data-driven Prediction
$[150, 250)$	11.64±1.57	12.48±0.97	0.93±0.15	7.95±1.43±1.65
$[250, 350)$	4.97±1.08	4.55±0.54	1.09±0.27	2.52±0.94±0.72
$[350, 450)$	2.09±0.66	1.15±0.25	1.82±0.70	0.58±0.30±0.35
$[450, \infty)$	0.23±0.21	0.57±0.23	0.40±0.40	$0.05^{+0.20+0.37}_{-0.04-0.05}$

the expected yield can be seen in Fig. 6.17. The data driven prediction and the simulated $\not\!\!E_{\mathrm{T}}$ spectrum shown for comparison, are displayed in Fig. 6.18.

6.2.3 Leptonic tau + lepton

Events in this category have two leptons in the final state where at least one of the leptons comes from a leptonic tau decay. They differ from the lost and ignored dilepton events previously described because of the presence of additional neutrinos from the tau decay. The control sample for this prediction is the same

Table 6.7: $\ell + \tau_{\mathrm{h}}$: Predicted yields for H_T >1000 GeV, $N_{\mathrm{j}} \geq 6$, and $N_b = 2$. This selection corresponds to an α factor of 0.59 ± 0.12.

$\not\!\!E_{\mathrm{T}}$ bin [GeV]	Simulated Yield	Simulated Prediction	κ	Data-driven Prediction
$[150, 250)$	3.39±0.83	4.18±0.50	0.81±0.22	1.67±0.74±0.69
$[250, 350)$	2.73±0.74	2.90±0.50	0.94±0.30	1.11±0.67±0.43
$[350, 450)$	1.24±0.52	1.05±0.25	1.18±0.57	$0.06^{+0.70+0.42}_{-0.06-0.03}$
$[450, \infty)$	0.23±0.21	0.56±0.26	0.40±0.41	$0.00^{+0.24+0.43}_{-0.00-0.00}$

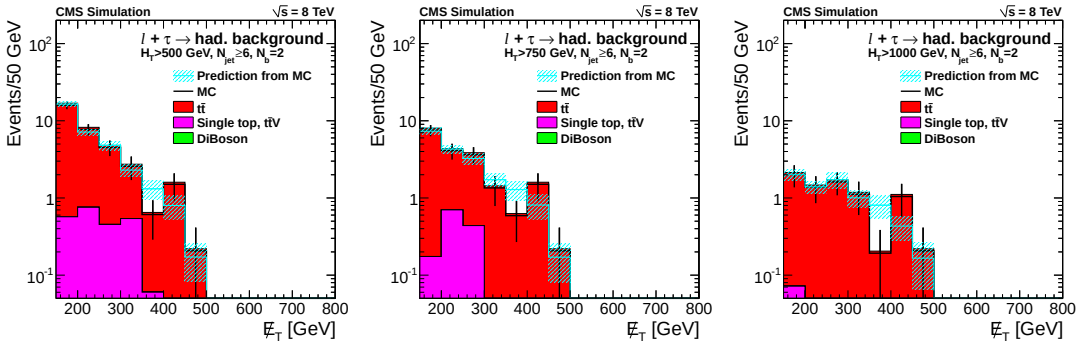

(a) (b) (c)

Figure 6.17: $\ell + \tau_{\mathrm{h}}$: As a closure test, the $N_{\mathrm{j}} \geq 6$ and $N_b = 2$ prediction from simulation is overlaid on the $\not\!\!E_{\mathrm{T}}$ distribution from simulation. By construction, the yields of the two distributions should be identical in any signal $\not\!\!E_{\mathrm{T}}$ bin.

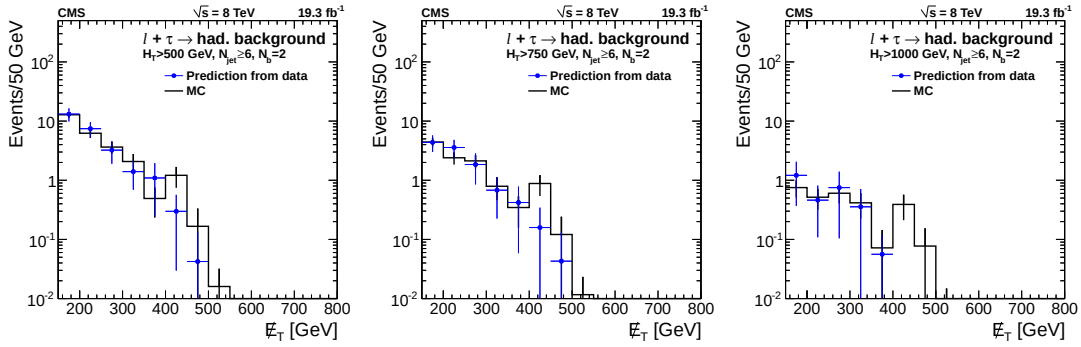

(a) (b) (c)

Figure 6.18: $\ell + \tau_{\mathrm{h}}$: The $\not\!\!E_{\mathrm{T}}$ spectrum prediction for $N_{\mathrm{j}} \geq 6$ and $N_b = 2$ from data overlaid with the simulated $\not\!\!E_{\mathrm{T}}$ distribution. The integral of the MC truth distribution is scaled to match that of the prediction from data. The uncertainty shown for the prediction from data includes the systematic uncertainties.

used for $\ell + \tau_{\mathrm{h}}$, except that the N_{j} and H_T requirements are those of the nominal signal selection.

The method to predict these events is similar to the method used for the $\ell + \tau_{\mathrm{h}}$ background, the difference being that leptons in the control sample are used to predict leptonic tau decays. This requires the use of a leptonic tau decay response function. The response functions used can be found in Fig. 6.19. They are derived in simulation from the p_T ratio of the generator level lepton to its mother tau. As seen in the figure, the templates are nearly identical in the different tau p_T bins because their derivation is not sensitive to measurement resolution and acceptance effects. The templates are derived from a simulated $t\bar{t}$ sample in which one W is required to decay to a τ with $|\eta| < 2.4$ which decays to a muon. The other

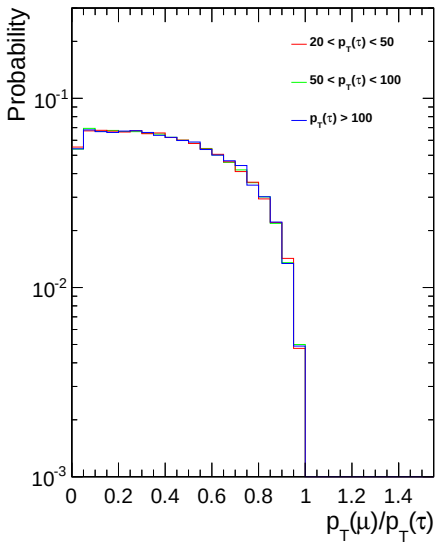

Figure 6.19: Tau-lepton response functions for various $p_T(\tau)$ bins.

W is required to decay hadronically to avoid confusion when matching the tau to its decay lepton. Tau to muon decays are used to create the templates, but they apply equally well to tau to electron decays.

From the tau-lepton response function, a random number, r_ℓ, is drawn. For one of the two leptons in the control sample event, $(1 - r_\ell)\vec{p}_T^{\,\ell}$ is added vectorially to the $\vec{\not{E}}_{\rm T}$ and the lepton is replaced by an emulated one with p_T of $r_\ell p_T^\ell$. The resulting event is required to pass the signal selection, meaning that the emulated decay lepton must have $p_T < 15$ GeV. One hundred samples are performed for each lepton in each event and averaged to determine the contribution of that

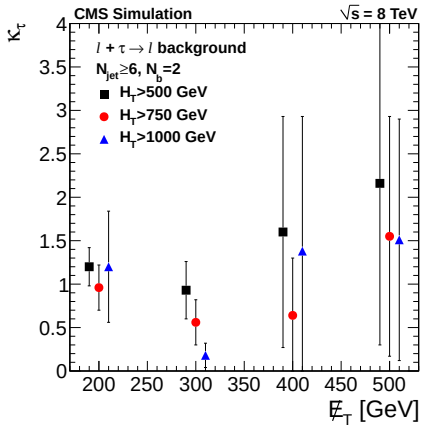

Figure 6.20: κ-factors used in the $\ell + \tau_\ell$ prediction for $N_\mathrm{j} \geq 6$ and $N_b = 2$. The error bars denote the statistical uncertainty.

event to the raw prediction. The statistical uncertainty on the raw prediction is determined in the same way as in the $\ell + \tau_\mathrm{h}$ prediction.

In this sample, the α factors come predominantly from lepton acceptance and efficiency effects, but the tau to lepton branching ratio is also important. The κ-factors for each of the three H_T selections are shown in Fig. 6.20.

This background prediction uses a dilepton control sample to estimate a background with two leptons in the final state, with only one selected. Because the non-selected lepton is less likely to fire the lepton leg of the trigger, there is a potential difference in trigger efficiency between the control and signal samples. To account for this potential bias, the average lepton leg inefficiency, 6%, is assigned as a systematic uncertainty to the prediction.

Table 6.8: $\ell + \tau_\ell$: Predicted yields for H_T >500 GeV, $N_\mathrm{j} \geq 6$, and $N_b = 2$. This selection corresponds to an α factor of 0.83 ± 0.12.

$\not\!\!E_\mathrm{T}$ bin [GeV]	Simulated Yield	Simulated Prediction	κ	Data-driven Prediction
$[150, 250)$	9.68±1.46	8.08±0.89	1.20±0.22	9.26±2.20±2.70
$[250, 350)$	1.99±0.60	2.15±0.42	0.93±0.33	1.16±0.46±0.46
$[350, 450)$	0.46±0.31	0.29±0.14	1.60±1.33	$0.00^{+1.33+1.23}_{-0.00-0.00}$
$[450, \infty)$	0.50±0.34	0.23±0.13	2.16±1.86	$0.00^{+1.80+1.84}_{-0.00-0.00}$

Table 6.9: $\ell + \tau_\ell$: Predicted yields for H_T >750 GeV, $N_\mathrm{j} \geq 6$, and $N_b = 2$. This selection corresponds to an α factor of 1.09 ± 0.22.

$\not\!\!E_\mathrm{T}$ bin [GeV]	Simulated Yield	Simulated Prediction	κ	Data-driven Prediction
$[150, 250)$	4.45±1.03	4.64±0.70	0.96±0.26	2.91±1.23±1.02
$[250, 350)$	1.05±0.42	1.88±0.46	0.56±0.26	0.30±0.16±0.28
$[350, 450)$	0.24±0.22	0.38±0.18	0.64±0.66	$0.00^{+0.70+0.83}_{-0.00-0.00}$
$[450, \infty)$	0.47±0.34	0.31±0.17	1.55±1.38	$0.00^{+1.69+1.66}_{-0.00-0.00}$

The simulated yields and predictions used to obtain the κ factors and the predictions in data for $\ell + \tau_\ell$ events are listed in Tables 6.8, 6.9, and 6.10 for the H_T requirements of 500, 750, and 1000 GeV, respectively. In these tables, the simulated yields and predictions have been scaled by the α factors of 0.83 ± 0.12, 1.09 ± 0.22, and 1.21 ± 0.54 for the H_T >500, 750, and 1000 GeV selections, respectively. Closure tests in simulation showing the predicted $\not\!\!E_\mathrm{T}$ spectrum overlaid on the expected yield are shown in Fig. 6.21. The data driven prediction and the $\not\!\!E_\mathrm{T}$ distribution from simulation, shown for comparison, are displayed in Fig. 6.22.

Table 6.10: $\ell + \tau_\ell$: Predicted yields for H_T >1000 GeV, $N_\mathrm{j} \geq 6$, and $N_b = 2$. This selection corresponds to an α factor of 1.21 ± 0.54.

$\not\!\!E_\mathrm{T}$ bin [GeV]	Simulated Yield	Simulated Prediction	κ	Data-driven Prediction
$[150, 250)$	1.07±0.48	0.89±0.26	1.20±0.64	1.02±0.78±0.73
$[250, 350)$	0.27±0.19	1.47±0.44	0.18±0.14	$0.02^{+0.22+1.01}_{-0.02-0.02}$
$[350, 450)$	0.22±0.22	0.16±0.08	1.38±1.55	$0.00^{+1.68+2.08}_{-0.00-0.00}$
$[450, \infty)$	0.47±0.34	0.31±0.18	1.51±1.39	$0.00^{+1.83+1.97}_{-0.00-0.00}$

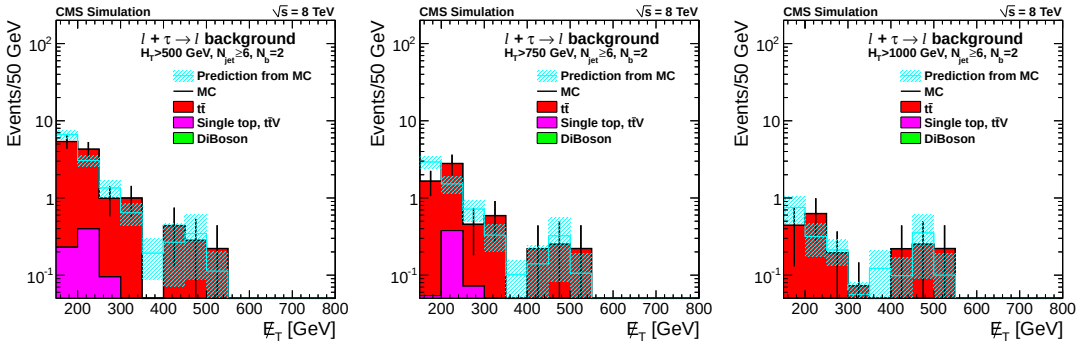

(a) (b) (c)

Figure 6.21: $\ell + \tau_\ell$: As a closure test, the $N_\mathrm{j} \geq 6$ and $N_b = 2$ prediction from simulation is overlayed on the simulated $\not\!\!E_\mathrm{T}$ distribution. By construction, the yields of the two distributions should be identical in any signal $\not\!\!E_\mathrm{T}$ bin.

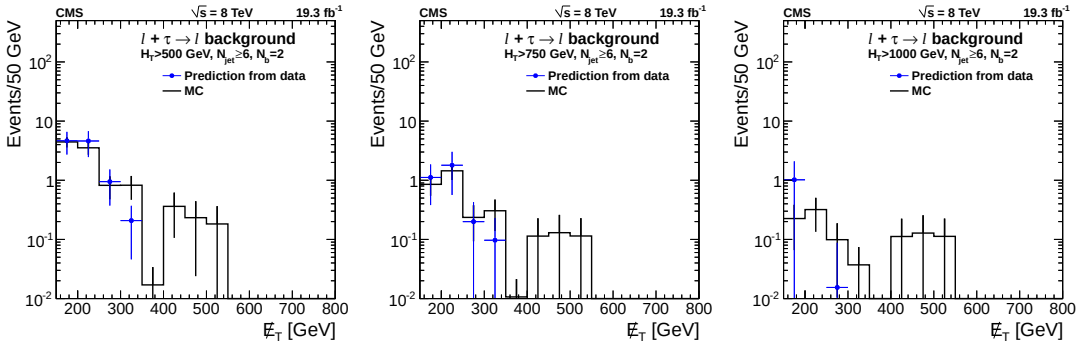

(a) (b) (c)

Figure 6.22: $\ell + \tau_\ell$: The $\not\!\!E_{\mathrm{T}}$ spectrum prediction for $N_{\mathrm{j}} \geq 6$ and $N_b = 2$ from data overlaid with the simulated $\not\!\!E_{\mathrm{T}}$ distribution. The integral of the simulated distribution is scaled to match that of the prediction from data. The uncertainty shown for the prediction from data includes the systematic uncertainties.

6.2.4 Single tau

The final major contributor to the background $\not\!\!E_{\mathrm{T}}$ distribution is events with a single tau and no other leptons, where the tau decays to an electron or a muon. These events have an enhanced $\not\!\!E_{\mathrm{T}}$ distribution compared to true single lepton events due to the neutrinos from the tau decay. The procedure to estimate this background is very similar to that for $\ell + \tau_\ell$ described above, with the major difference being the use of a single lepton control sample rather than a dilepton control sample. This control sample is the same as the signal sample with the exception that the $\not\!\!E_{\mathrm{T}}$ requirement is dropped and events can enter on the lepton+H_T (+$\not\!\!E_{\mathrm{T}}$) triggers. For electron events, there is an additional require-

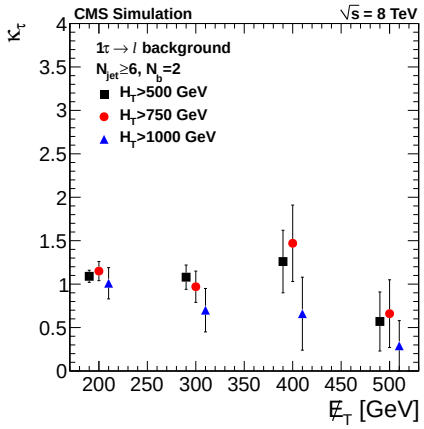

Figure 6.23: κ-factors used in the single τ_ℓ prediction for $N_\mathrm{j} \geq 6$ and $N_b = 2$. The error bars denote the statistical uncertainty.

ment of $0.26 < \Delta\phi(\not{E}_\mathrm{T}, j_1) < 3.05$, where j_1 is the highest p_T jet, which is used to suppress QCD.

Leptons in the control sample are used to emulate τ_ℓ decays just as in the $\ell+\tau_\ell$ prediction. After emulation, the resulting event is required to pass the signal selection, meaning that the emulated decay lepton must have $p_T > 20$ GeV. Each event is sampled a hundred times and averaged. The statistical uncertainty on the raw prediction is determined in the same way as in the other tau predictions.

The α factors for the single tau prediction are dominated by the tau to lepton branching ratio. The κ-factors for each of the H_T selections are shown in Fig. 6.23.

The simulated yields and predictions used to obtain the κ factors and the predictions in data for single τ_ℓ events are listed in Tables 6.11, 6.12, and 6.13 for the H_T requirements of 500, 750, and 1000 GeV, respectively. In these tables, the

Table 6.11: single τ_ℓ: Predicted yields for H_T >500 GeV, $N_\mathrm{j} \geq 6$, and $N_b = 2$. This selection corresponds to an α factor of 0.17 ± 0.01.

$\not\!\!E_\mathrm{T}$ bin [GeV]	Simulated Yield	Simulated Prediction	κ	Data-driven Prediction
$[150, 250)$	58.74±3.60	53.82±0.88	1.09±0.07	47.25±1.84±5.37
$[250, 350)$	13.61±1.73	12.58±0.41	1.08±0.14	8.87±0.75±1.40
$[350, 450)$	3.74±1.03	2.98±0.20	1.26±0.36	1.84±0.34±0.65
$[450, \infty)$	0.60±0.35	1.06±0.12	0.57±0.34	0.28±0.10±0.27

Table 6.12: single τ_ℓ: Predicted yields for H_T >750 GeV, $N_\mathrm{j} \geq 6$, and $N_b = 2$. This selection corresponds to an α factor of 0.17 ± 0.01.

$\not\!\!E_\mathrm{T}$ bin [GeV]	Simulated Yield	Simulated Prediction	κ	Data-driven Prediction
$[150, 250)$	23.53±2.25	20.49±0.52	1.15±0.11	18.66±1.17±3.32
$[250, 350)$	6.74±1.24	6.95±0.30	0.97±0.18	3.51±0.44±0.72
$[350, 450)$	3.48±1.00	2.36±0.17	1.47±0.44	1.65±0.34±0.73
$[450, \infty)$	0.60±0.35	0.91±0.10	0.66±0.39	0.29±0.10±0.23

simulated yields and predictions have been scaled by the α factors of 0.17 ± 0.01, 0.17 ± 0.01, and 0.19 ± 0.02 for the H_T >500, 750, and 1000 GeV selections, respectively. Closure tests in simulation showing the predicted $\not\!\!E_\mathrm{T}$ spectrum overlaid on the expected yield are shown in Fig. 6.24. The data driven prediction and the simulated $\not\!\!E_\mathrm{T}$ distribution, shown for comparison, are displayed in Fig. 6.25.

Table 6.13: single τ_ℓ: Predicted yields for H_T >1000 GeV, $N_\mathrm{j} \geq 6$, and $N_b = 2$. This selection corresponds to an α factor of 0.19 ± 0.02.

$\not{E}_\mathrm{T}$ bin [GeV]	Simulated Yield	Simulated Prediction	κ	Data-driven Prediction
$[150, 250)$	7.66±1.31	7.59±0.34	1.01±0.18	6.64±0.71±1.43
$[250, 350)$	2.00±0.69	2.84±0.20	0.70±0.25	0.97±0.20±0.55
$[350, 450)$	0.86±0.55	1.31±0.14	0.66±0.42	0.35±0.11±0.30
$[450, \infty)$	0.21±0.21	0.73±0.10	0.29±0.29	0.07±0.04±0.20

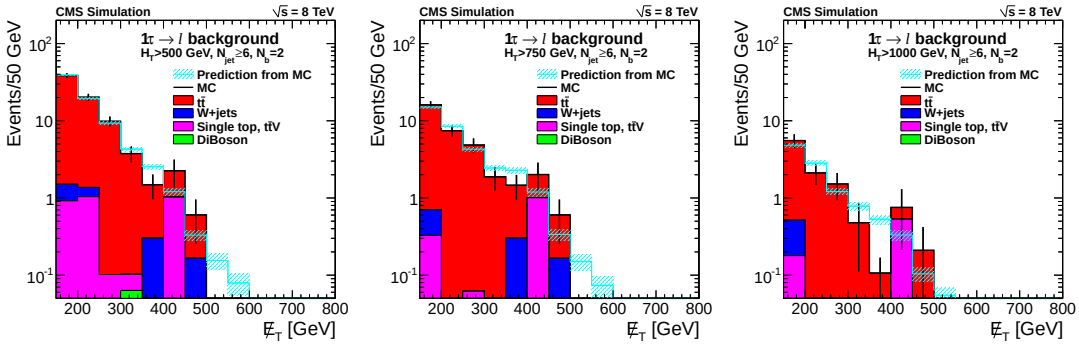

(a) (b) (c)

Figure 6.24: single τ_ℓ: As a closure test, the $N_\mathrm{j} \geq 6$ and $N_b = 2$ prediction from simulation is overlaid on the simulated $\not{E}_\mathrm{T}$ distribution. By construction, the yields of the two distributions should be identical in any signal $\not{E}_\mathrm{T}$ bin.

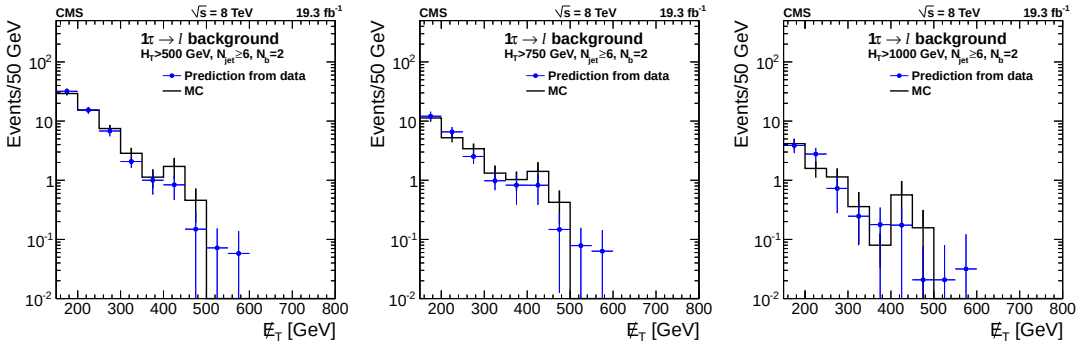

(a) (b) (c)

Figure 6.25: single τ_ℓ: The $\not\!\!E_{\mathrm{T}}$ spectrum prediction for $N_{\mathrm{j}} \geq 6$ and $N_b = 2$ from data overlaid with the simulated distribution. The integral of the simulated distribution is scaled to match that of the prediction from data. The uncertainty shown for the prediction from data includes the systematic uncertainties.

6.3 QCD Multijet Background

The QCD multijet background to this search is very small, but non-trivial to estimate. The absence of promptly produced leptons means that some background source must mimic a prompt lepton for an event to pass the selection. Some of these backgrounds are briefly discussed in Sec. 4.5 for muons and Sec. 4.4 for electrons. Additionally, because multijet events do not have significant genuine $\not\!\!E_{\mathrm{T}}$ from neutrinos, large mis-measurements of the jet energies are usually required in order to pass the signal selection. Finally, the fact that the multijet background is not particularly b-quark enriched further suppresses it with respect to the dominant $t\bar{t}$ background. However, despite the multiple factors that reduce

the multijet background, it has an enormous cross section and therefore could possibly appear in the signal and control samples. Because the cross section is poorly known theoretically and the multijet background contains difficult to simulate mis-reconstruction and mis-measurement effects, the estimate of this background should rely heavily on data. Due to the small expected QCD background yield, a simple and relatively imprecise approach can be used.

The QCD multijet background is estimated using the sidebands of the relative isolation distribution. The analysis selection is performed as usual except the relative isolation requirement is removed. Before extrapolating the QCD background from the sideband, the small contribution of non-QCD backgrounds, i.e., those with promptly produced leptons, must be determined. This is done by treating the entire non-QCD background as originating from $t\bar{t}$ and normalizing its cross section such that the expected number of such events equals the data yield in the QCD depleted, low relative isolation region. The treatment of $t\bar{t}$ as the sole component of the prompt lepton background is justified because it is by far the dominant component and the isolation shape of the other prompt lepton backgrounds is very similar.

After normalizing its cross section, the relative isolation distribution from $t\bar{t}$ simulation is then subtracted from that observed in data to remove its contamination of the high isolation sideband. Assuming the multijet relative isolation

distribution is flat over the relevant region, it is extrapolated into the signal region by scaling the $t\bar{t}$-subtracted data yield in the sideband by the ratio of the width in isolation of the signal to sideband regions. Because the electron triggers impose an isolation requirement, the extent of the electron isolation sideband used in the prediction is restricted to avoid trigger bias. The muon triggers have no such isolation requirement, and hence the muon sideband can extend to higher isolation.

An advantage of this method is that it does not use multijet simulation nor does it depend on the predicted cross-sections of the backgrounds. Because the full event selection is applied, the predictions are only practical for the $H_T > 500$ GeV selection due to a lack of events in the high relative isolation sideband. However, inclusive QCD simulation shows that the yield of events passing $H_T > 750$ GeV is an order of magnitude smaller than for $H_T > 500$ GeV, which is negligible.

Figures 6.26–6.28 (6.29–6.31) show the results of the QCD background prediction to the p_T ($\not\!\!E_{\mathrm{T}}$) spectrum in both the electron and muon channels and Tab. 6.14(6.15) summarizes these results. As a result of these measurements, which are consistent with zero QCD contribution to the MET signal regions ($\not\!\!E_{\mathrm{T}} > 250$ GeV) and the p_T spectrum relevant for the single lepton prediction ($p_T > 250$ GeV), the QCD background can be safely neglected in this analysis.

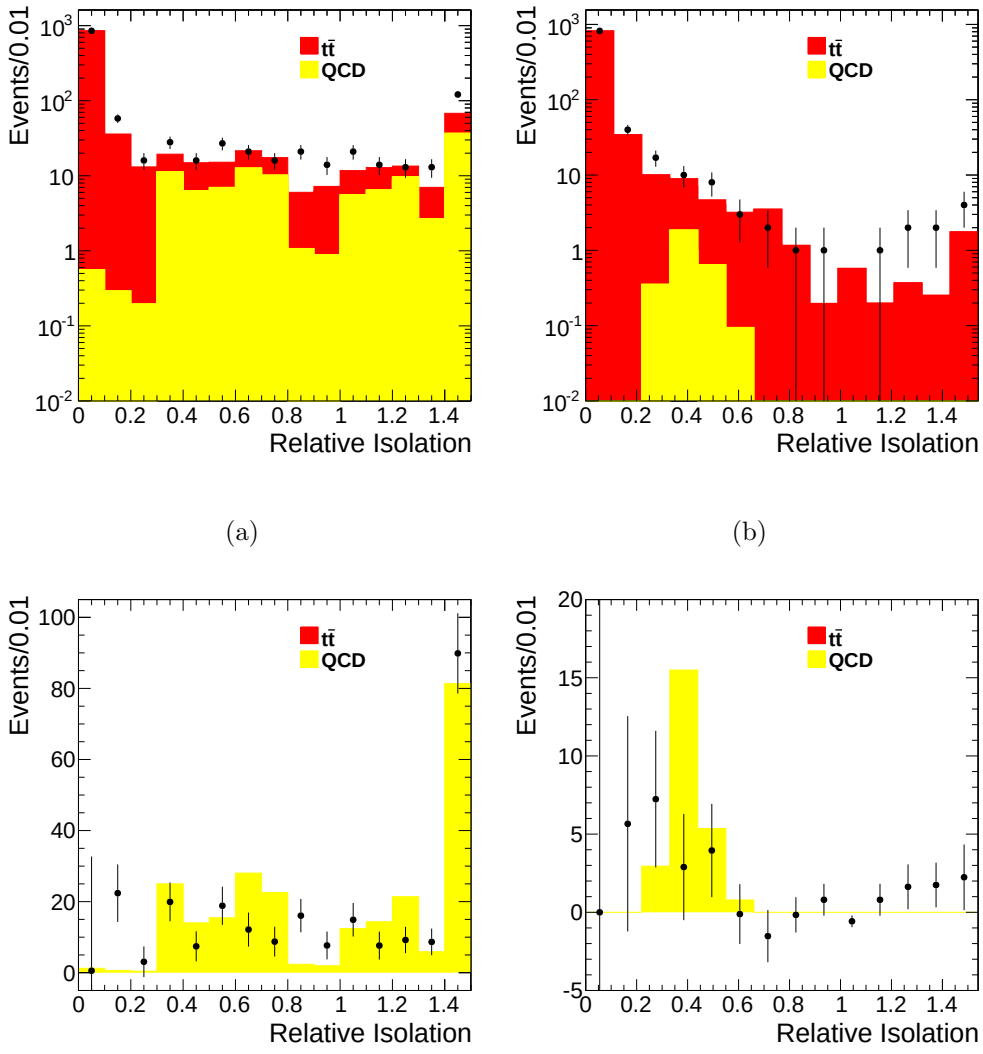

Figure 6.26: QCD relative isolation distribution in the muon (left) and electron (right) channels before (top) and after (bottom) background subtraction for $50 < p_T < 100$ GeV. In the lower plots, the MC is scaled to the predicted yield. The highest histogram bin contains the overflow.

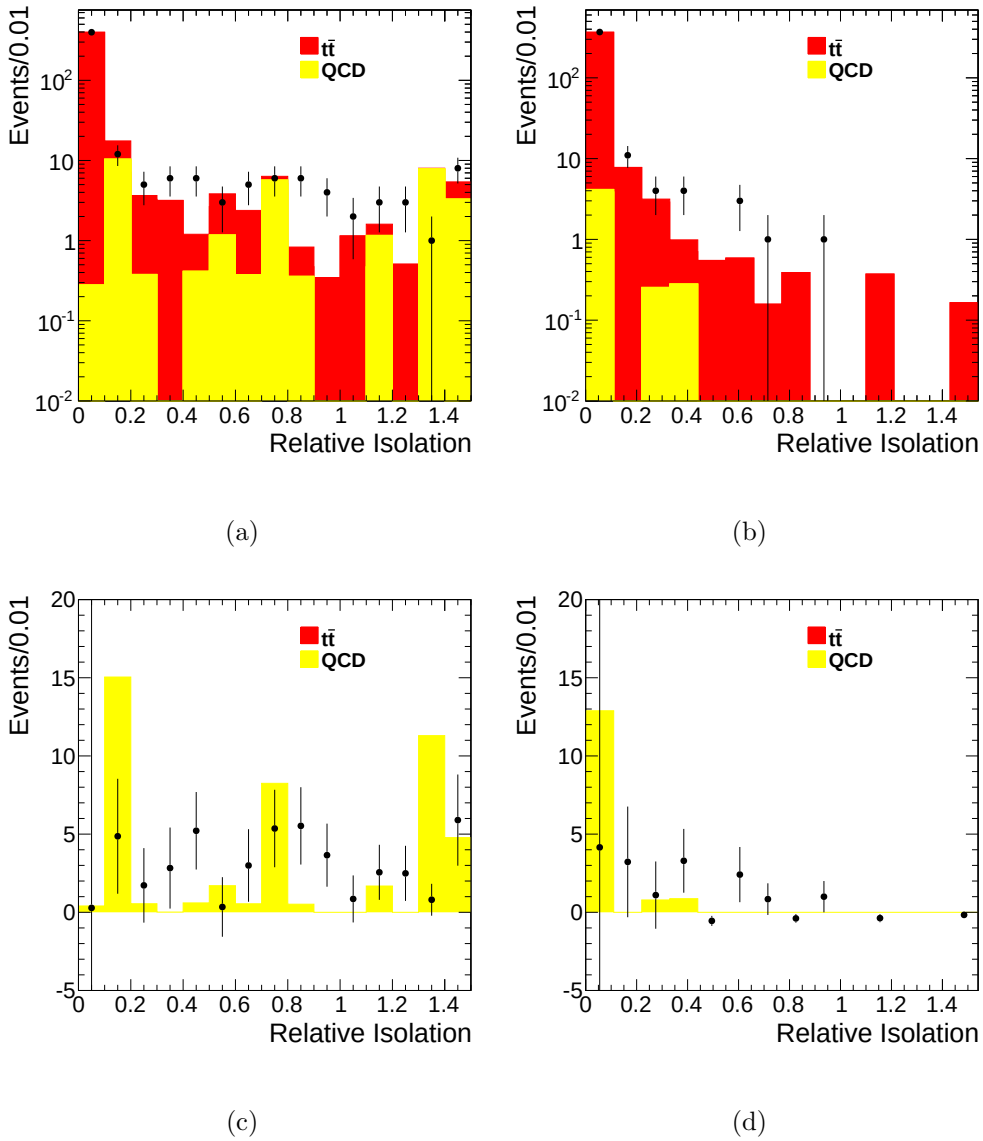

Figure 6.27: QCD relative isolation distribution in the muon (left) and electron (right) channels before (top) and after (bottom) background subtraction for $100 < p_T < 250$ GeV. In the lower plots, the MC is scaled to the predicted yield. The highest histogram bin contains the overflow.

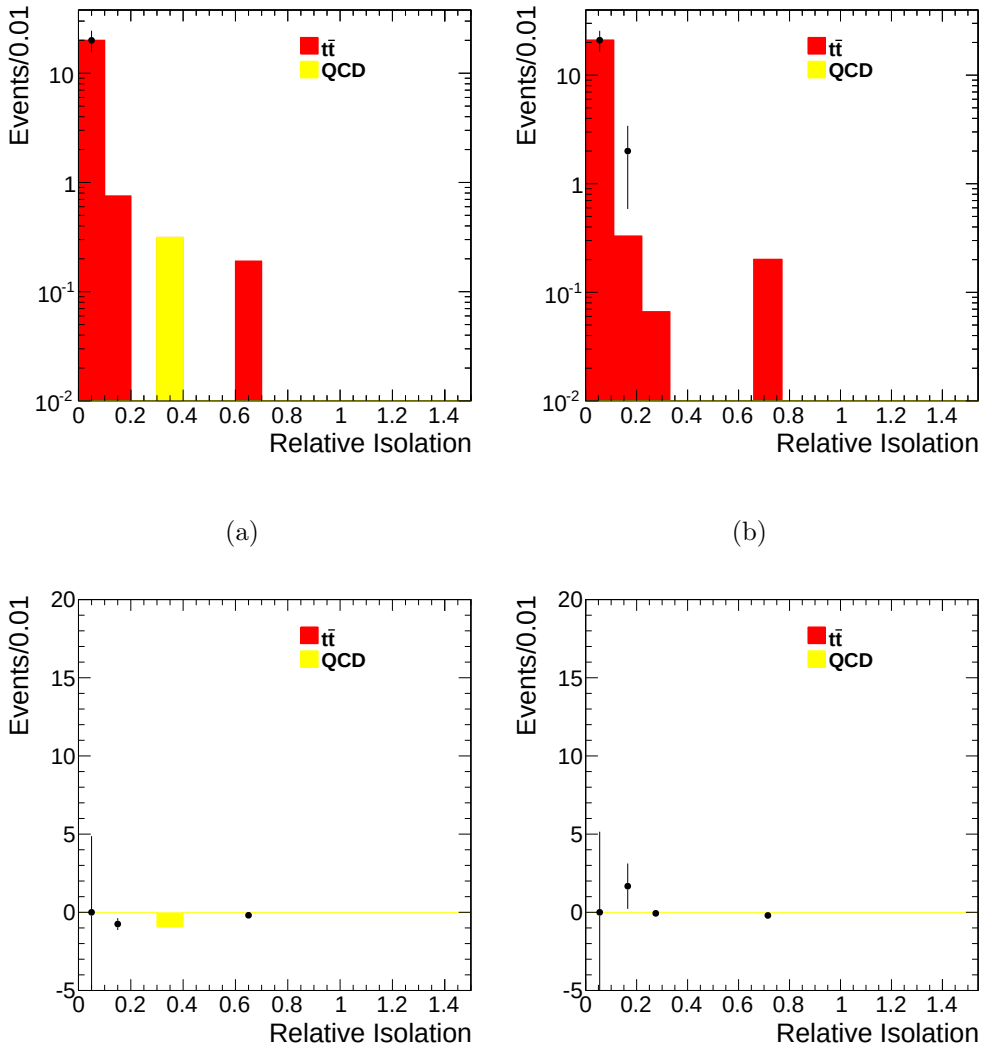

Figure 6.28: QCD relative isolation distribution in the muon (left) and electron (right) channels before (top) and after (bottom) background subtraction for $p_T >$ 250 GeV. In the lower plots, the MC is scaled to the predicted yield. The highest histogram bin contains the overflow.

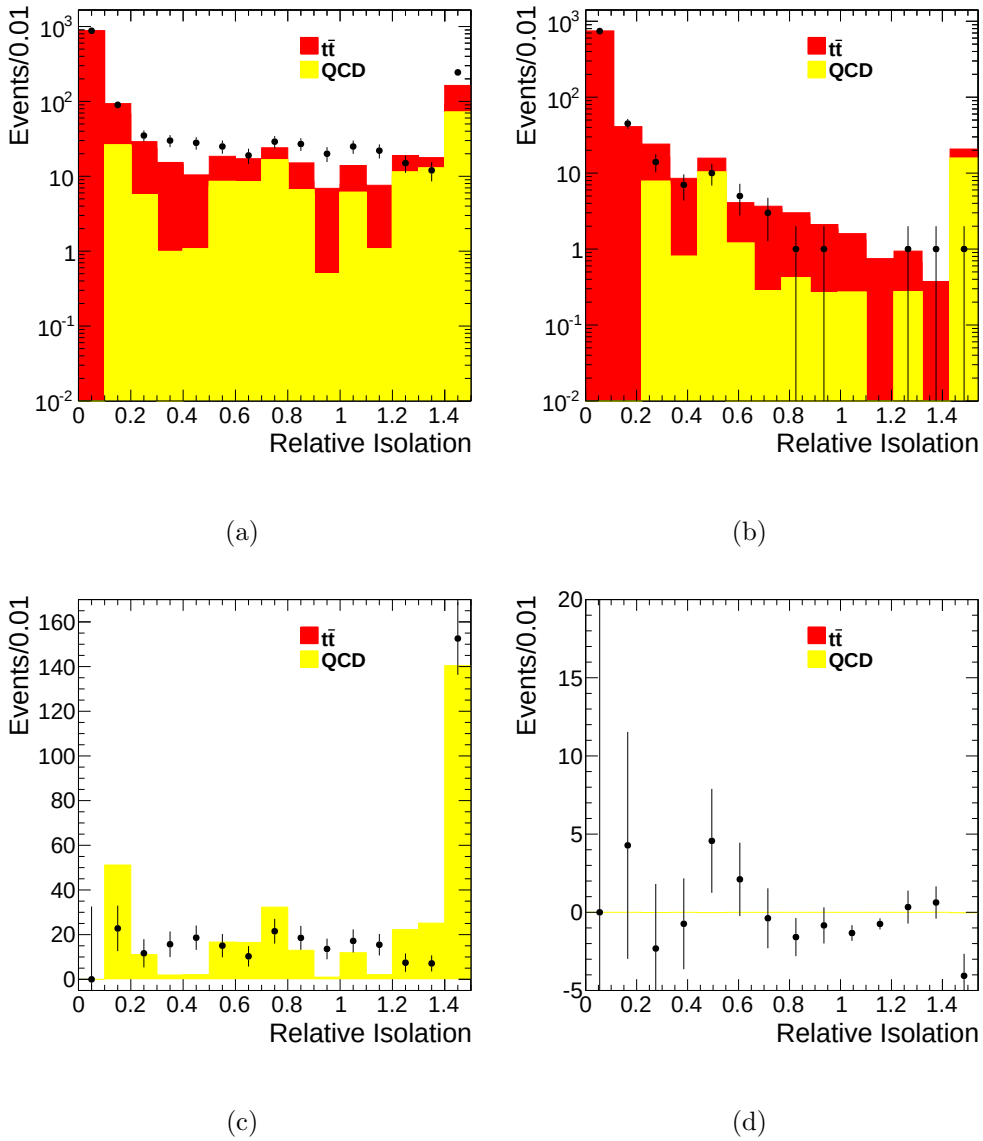

Figure 6.29: QCD relative isolation distribution in the muon (left) and electron (right) channels before (top) and after (bottom) background subtraction for $50 < \not\!\!E_T < 100$ GeV. In the lower plots, the MC is scaled to the predicted yield. The highest histogram bin contains the overflow.

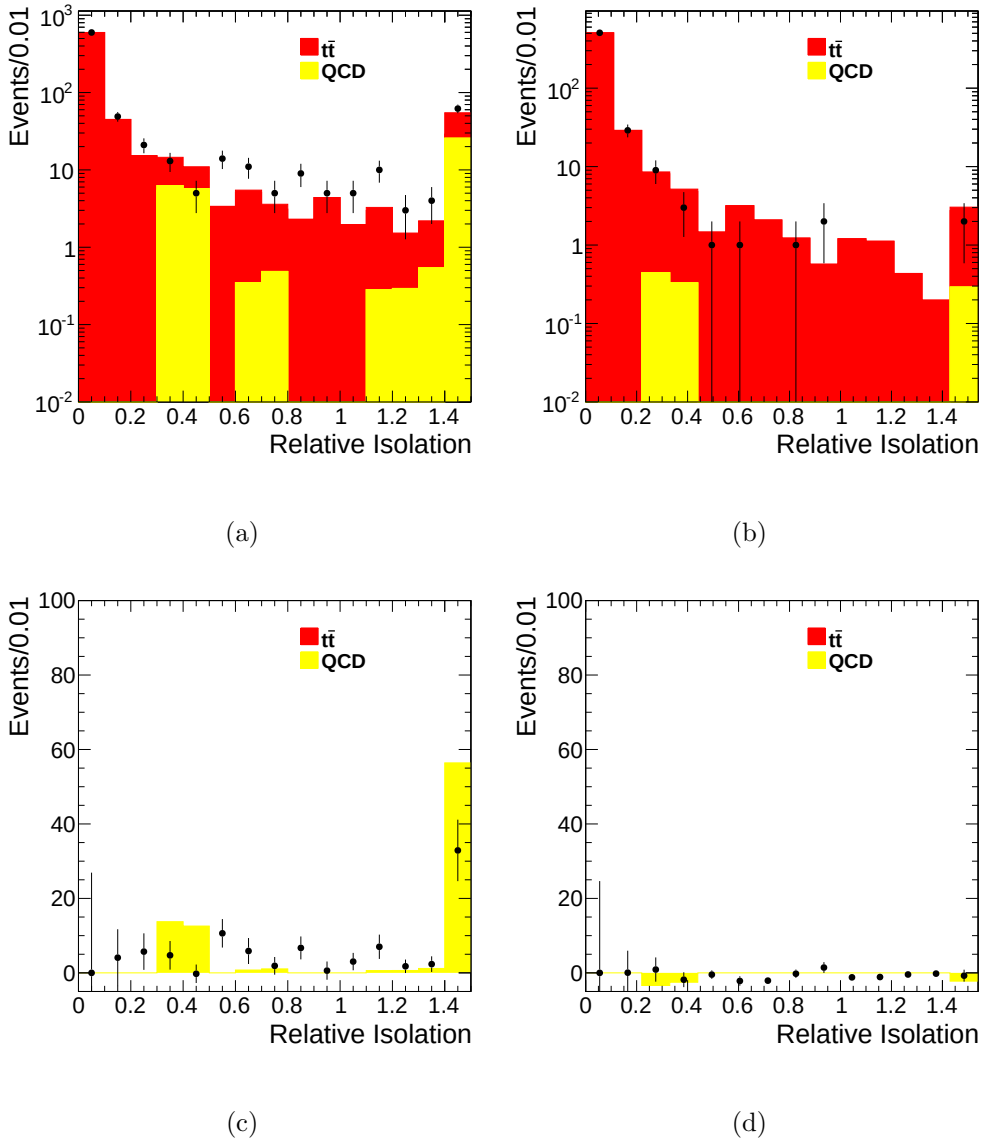

Figure 6.30: QCD relative isolation distribution in the muon (left) and electron (right) channels before (top) and after (bottom) background subtraction for $100 < \not\!\!E_T < 250$ GeV. In the lower plots, the MC is scaled to the predicted yield. The highest histogram bin contains the overflow.

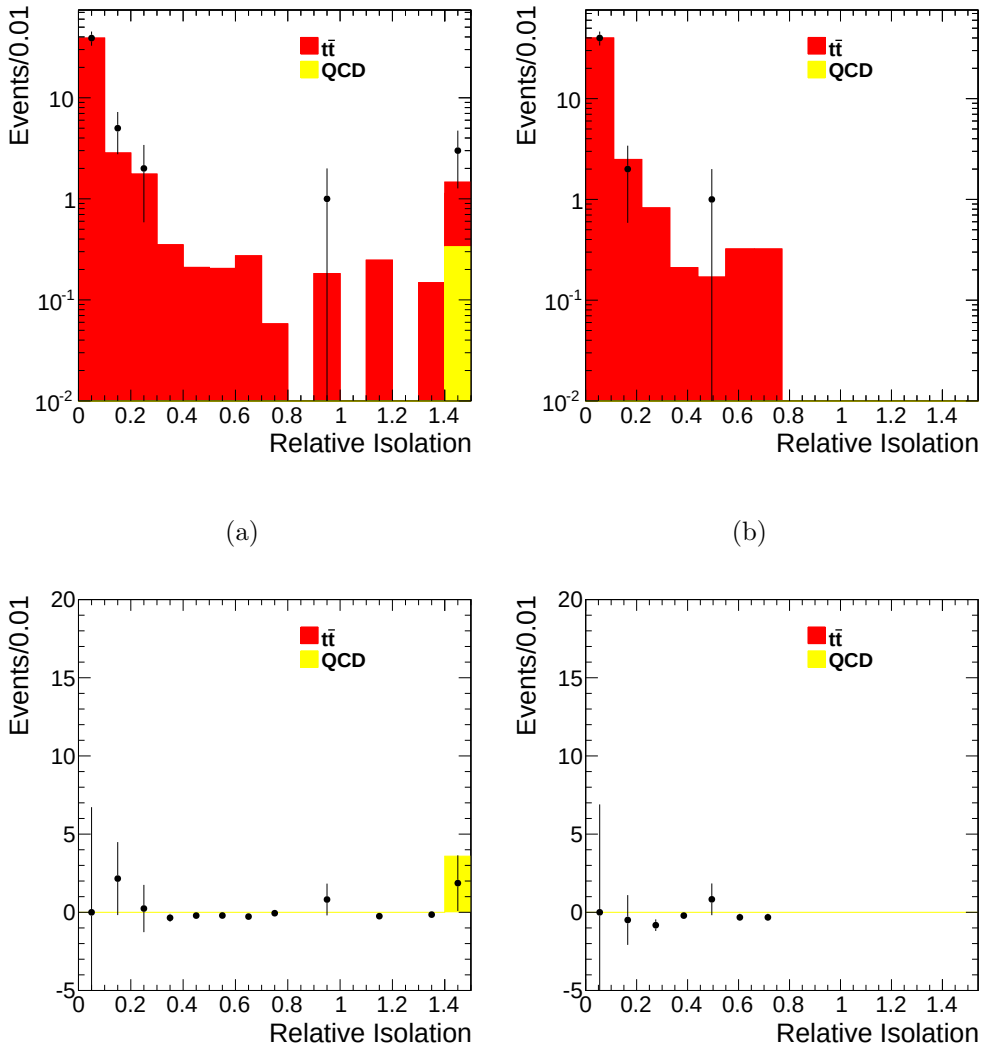

Figure 6.31: QCD relative isolation distribution in the muon (left) and electron (right) channels before (top) and after (bottom) background subtraction for $\not\!\!E_T >$ 250 GeV. In the lower plots, the MC is scaled to the predicted yield. The highest histogram bin contains the overflow.

Table 6.14: Predicted QCD backgrounds to p_T distribution for H_T >500 GeV.

Lepton	p_T range	Subtracted yield	Scale factor	QCD estimate
Muon	$50 < p_T < 100$	134.3 ± 15.4	0.1	13.4 ± 1.5
	$100 < p_T < 250$	34.3 ± 7.3		3.4 ± 0.7
	$p_T > 250$	0.0 ± 0.2		0.00 ± 0.02
Electron	$50 < p_T < 100$	12.9 ± 8.2	0.75	9.7 ± 6.1
	$100 < p_T < 250$	4.3 ± 4.1		3.3 ± 3.1
	$p_T > 250$	1.6 ± 1.5		1.2 ± 1.1

Table 6.15: Predicted QCD background to $\not\!\!E_T$ distribution for H_T >500 GeV.

Lepton	$\not\!\!E_T$ range	Subtracted yield	Scale factor	QCD estimate
Muon	$50 < \not\!\!E_T < 100$	172.3 ± 17.6	0.1	17.2 ± 1.8
	$100 < \not\!\!E_T < 250$	50.0 ± 10.8		5.0 ± 1.1
	$150 < \not\!\!E_T < 250$	7.2 ± 5.6		0.7 ± 0.6
	$\not\!\!E_T > 250$	0.0 ± 1.8		0.00 ± 0.18
Electron	$50 < \not\!\!E_T < 100$	2.0 ± 8.3	0.75	1.5 ± 6.3
	$100 < \not\!\!E_T < 250$	0.9 ± 6.7		0.7 ± 5.1
	$150 < \not\!\!E_T < 250$	1.1 ± 4.0		0.9 ± 3.0
	$\not\!\!E_T > 250$	0.0 ± 1.6		0.0 ± 1.2

6.4 Extrapolating the $N_b = 2$ Prediction to $N_b \geq 3$

Because the dominant background in this search is $t\bar{t}$, and each top-quark decay results in one bottom-quark, the $N_b \geq 3$ selection drastically reduces the background yield. The third b tag must come from either a b quark produced by gluon splitting, or the mistag of a light flavor or charm jet. These sources of b tags are suppressed by the low occurrence rate of the former and the low mistag rate of the latter.

Due to their small event yields, the $N_b \geq 3$ data control samples cannot be used to adequately estimate the $N_b \geq 3$ signal yields. Therefore, the $N_b \geq 3$ background is estimated from the $N_b = 2$ background predictions using extrapolation factors from simulation, referred to as R_{32}. A separate R_{32} factor is derived for each signal region and is defined as:

$$R_{32} = \frac{N_b \geq 3 \text{ yield}}{N_b = 2 \text{ yield}}, \tag{6.6}$$

so that the $N_b \geq 3$ prediction in a given signal bin is simply:

$$(N_b \geq 3 \text{ prediction}) = (N_b = 2 \text{ prediction}) \times R_{32}. \tag{6.7}$$

The full set of relevant SM processes are used to calculate R_{32}. It is important to have separate R_{32} for different N_{j}, H_T, and $\not{E}_{\text{T}}$ selections as the resulting change in event kinematics can alter R_{32}. The H_T and $\not{E}_{\text{T}}$ selections affect the average

Table 6.16: R_{32} in the $\not\!\!E_{\mathrm{T}}$ signal bins for the different H_T thresholds and $N_{\mathrm{j}} \geq 6$. The quoted uncertainties are statistical only.

	R_{32}		
$\not\!\!E_{\mathrm{T}}$ bin [GeV]	$H_T > 500$	$H_T > 750$	$H_T > 1000$ GeV
$[150, 250)$	0.223 ± 0.004	0.226 ± 0.005	0.242 ± 0.011
$[250, 350)$	0.213 ± 0.007	0.225 ± 0.011	0.238 ± 0.019
$[350, 450)$	0.203 ± 0.014	0.200 ± 0.017	0.190 ± 0.022
$[450, \infty)$	0.210 ± 0.022	0.210 ± 0.022	0.220 ± 0.026

jet p_T and $|\eta|$, sculpting the b-tag efficiencies. The N_{j} selection has a larger effect because additional jets provide more opportunities to tag a third jet in the event. Table 6.16 lists the values of R_{32} in each of the signal regions.

In deriving R_{32}, the jet b-tag probabilities in the simulated events are reweighted to match the data, as described in Sec. 4.2.1. To maximize the statistical precision with which R_{32} is measured in simulation, a combinatorial reweighting approach is utilized in which the tag efficiency of each jet in the event is used to calculate the contribution of the event to each N_b bin. To properly evaluate the statistical uncertainty on R_{32} given that events can contribute to both the numerator and denominator of Eq. 6.6, the "jackknife" resampling technique [122] is used.

Because the R_{32} factors are derived in simulation, the $N_b \geq 3$ background prediction is sensitive to biases arising from differences between simulation and data. There are multiple such potential differences, described below, for which systematic uncertainties on R_{32} are assigned.

- **b-tag efficiency/mistag rate:** The scale factors used to reweight the simulated b-tag efficiency and mistag rates to match the data have associated uncertainty [83]. The SF_b and SF_c values across all jet p_T and $|\eta|$ bins are simultaneously varied up or down by their uncertainty, and the resulting maximum change in R_{32} is taken as a systematic. Separately, the SF_{lf} values across all bins are simultaneously varied by their uncertainty and the resulting change in R_{32} is taken as a systematic.

- **Kinematic differences in the non b-quark hadronic system:** Because the mistag rates vary considerably with jet p_T and $|\eta|$, the kinematic differences in the non b-quark jets can influence R_{32}. To evaluate such differences, the non b-tagged jets in each $N_b = 2$ event are randomly assigned a flavor such that one is treated as coming from a c quark and the others are treated as light flavor with regards to their mistag probabilities. After this flavor assignment, R_{32} is calculated in both simulation and data, and the relative difference between the two is taken as a systematic error on R_{32}.

- **Gluon splitting:** The simulation does not model initial state or final state radiation $g \to b\bar{b}$ or $g \to c\bar{c}$ splitting particularly well. According to CMS standard practice, the contribution of events with gluon splitting to $b\bar{b}$ or $c\bar{c}$

Table 6.17: Systematic uncertainties, in percent, on R_{32} for H_T >(500/750/1000) GeV and $N_{\mathrm{j}} \geq 6$.

$\not\!\!E_{\mathrm{T}}$ bin:	[150,250)	[250,350)	[350,450)	$\geq$ 450 GeV
SF_b and SF_c	3/3/3	3/3/3	4/4/4	5/5/6
SF_{lf}	4/4/4	4/4/4	4/4/5	4/4/4
Kinematic differences	0.6/0.3/5	0.2/0.4/4	1/2/15	16/16/16
Gluon splitting	7/6/7	6/6/5	3/3/5	8/8/7
Charm fraction	6/6/5	7/8/9	9/11/13	12/12/11
Total	11/10/11	10/11/12	11/13/22	22/22/22

is varied up and down by 50% and the resulting maximum change in R_{32} is taken as a systematic uncertainty.

- **Charm-quark fraction:** Because the charm content in the simulation is not precisely known, the fraction of events with a c quark not originating from gluon splitting is varied up and down by 50%. The resulting maximum change in R_{32} is taken as a systematic uncertainty. This is a conservative estimate of the uncertainty because the majority of the c quarks in the sample which do not originate from gluon splitting are from W decays, and therefore reasonably well modeled.

The relative systematic uncertainty on R_{32} in the signal regions from the above sources is shown in Tab. 6.17.

Finally, a cross-check is performed by comparing R_{32} in simulation and data to determine whether there are any other sources of mis-modeling in the sim-

ulation which bias R_{32}. This comparison is done in an $H_T < 400$ GeV and $100 < \not{E}_{\mathrm{T}} < 250$ GeV control sample to avoid signal contamination. Because of the H_T requirement, the usual lepton+H_T (+$\not{E}_{\mathrm{T}}$) triggers are not efficient, and single electron or muon triggers are used instead to select the events. The only other modifications to the usual signal selection are an increased lepton p_T threshold of 30 GeV to remain on the efficiency plateau of the single lepton triggers and selecting in bins of $N_{\mathrm{j}} \geq 6$ and $N_{\mathrm{j}} = 5$. For $N_{\mathrm{j}} \geq 6$, R_{32} is measured to be 0.235 ± 0.065 (stat.) in the data and 0.195 ± 0.013 (stat.) in simulation. For $N_{\mathrm{j}} = 5$, R_{32} is is measured to be 0.158 ± 0.015 (stat.) in the data and 0.142 ± 0.003 (stat.) in simulation. In each N_{j} bin, the measured values agree to within statistical uncertainty and the cross-check is passed.

Chapter 7

Results

The estimates of the distinct background components[1] described in Ch. 6 are combined and plotted with the observations in data for the three H_T selections in Fig. 7.1 for the $N_b = 2$ and $3 \leq N_{\mathrm{j}} \leq 5$ validation region. Figure 7.2 shows the total background prediction for the $N_b \geq 3$ validation region along with the data. The predicted and observed yields in the validation regions agree reasonably well, demonstrating a successful cross-check of the estimation methods. Figs. 7.3 and 7.4 show the observations and predictions in the $N_{\mathrm{j}} \geq 6$ signal regions for $N_b = 2$ and $N_b \geq 3$, respectively. A point from the T1tttt SMS, excluded by this analysis, is shown for reference.

The predictions and observations in the validation regions are summarized in Tables 7.1-7.6 for the different H_T and N_b selections. The predictions and observations in the $\not\!\!E_{\mathrm{T}}$ signal bins are summarized in Tables 7.7-7.12. Because

[1]For simplicity, the subdominant background contributions from lost and ignored dilepton, $\ell+\tau_\ell$, and $\ell+\tau_{\mathrm{h}}$ are summed and collectively referred to as "Dilepton" throughout this chapter.

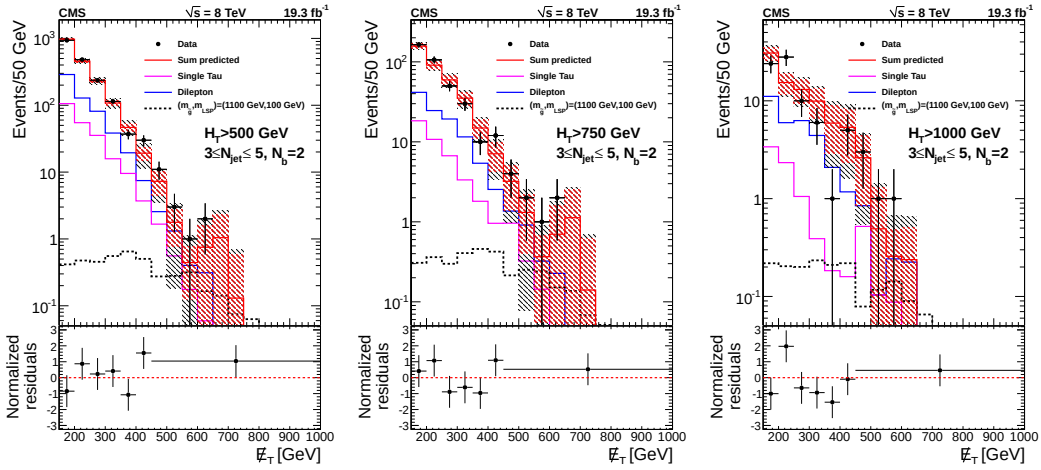

(a) (b) (c)

Figure 7.1: Data (dots with error bars) overlaid on the total prediction (red histogram) for $3 \leq N_{\mathrm{j}} \leq 5$ and $N_b = 2$ for the three H_T selections. The top panel shows the absolute yields while the bottom shows the difference between the observation and prediction, divided by its uncertainty. The purple line is the predicted contribution from single taus and the blue line is the predicted dilepton contribution. The red error band includes the statistical error in the single lepton scale factor and the JET/MET scale uncertainty and the black error band indicates the total uncertainty on the prediction. A reference signal point (dashed histogram) is shown for comparison.

the relative contributions of individual background components can differ between the N_b bins and are not specifically predicted in the $N_b \geq 3$ case, only the total prediction is quoted for $N_b \geq 3$. The signal yields in two points from the T1tttt SMS, only one of which is within the exclusion reach of this analysis, are shown for reference.

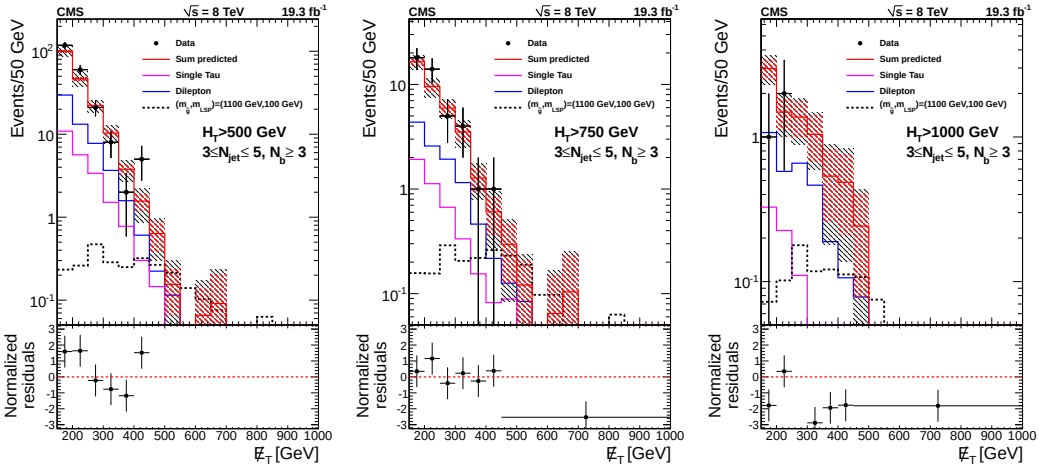

(a) (b) (c)

Figure 7.2: Data (dots with error bars) overlaid on the total prediction (red histogram) for $3 \leq N_{\mathrm{j}} \leq 5$ and $N_b \geq 3$ for the three H_T selections. The top panel shows the absolute yields while the bottom shows the difference between the observation and prediction, divided by its uncertainty. The single tau and dilepton background components are shown for reference only, as their contributions are not separately predicted with R_{32}. The red error band includes the statistical error in the single lepton scale factor and the JET/MET scale uncertainty and the black error band indicates the total uncertainty on the prediction. A reference signal point (dashed histogram) is shown for comparison.

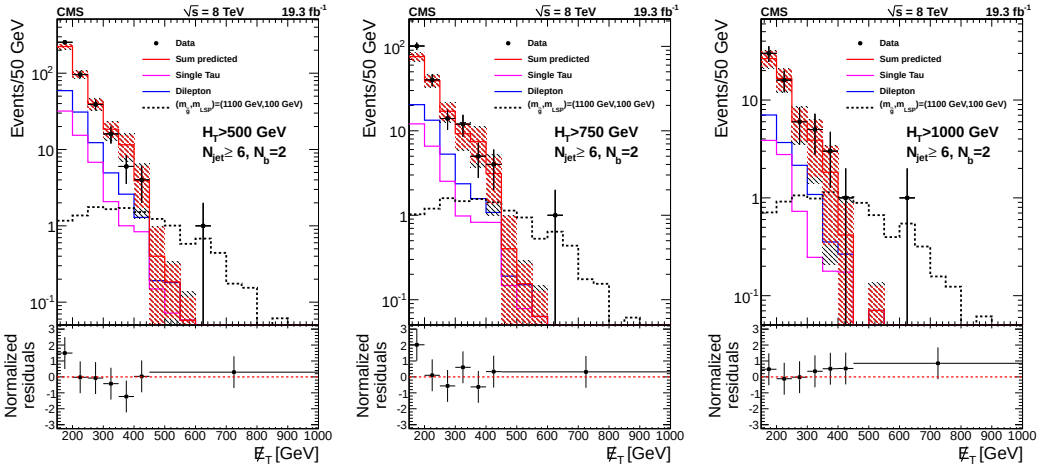

(a) (b) (c)

Figure 7.3: Data (dots with error bars) overlaid on the total prediction (red histogram) for $N_{\mathrm{j}} \geq 6$ and $N_b = 2$ for the three H_T selections. The top panel shows the absolute yields while the bottom shows the difference between the observation and prediction, divided by its uncertainty. The purple line is the predicted contribution from single taus and the blue line is the predicted dilepton contribution. The red error band includes the statistical error in the single lepton scale factor and the JET/MET scale uncertainty and the black error band indicates the total uncertainty on the prediction. A reference signal point (dashed histogram) is shown for comparison.

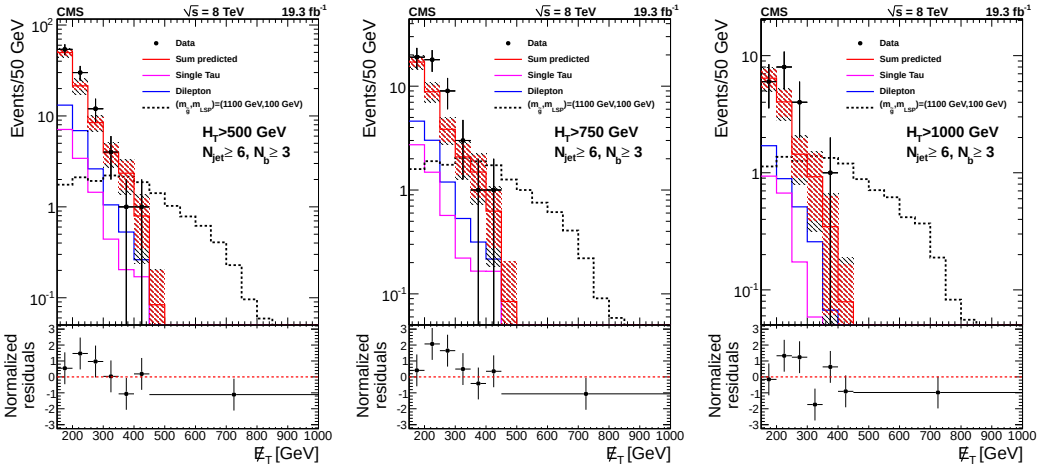

(a) (b) (c)

Figure 7.4: Data (dots with error bars) overlaid on the total prediction (red histogram) for $N_{\mathrm{j}} \geq 6$ and $N_b \geq 3$ for the three H_T selections. The top panel shows the absolute yields while the bottom shows the difference between the observation and prediction, divided by its uncertainty. The single tau and dilepton background components are shown for reference only, as their contributions are not separately predicted with R_{32}. The red error band includes the statistical error in the single lepton scale factor and the JET/MET scale uncertainty and the black error band indicates the total uncertainty on the prediction. A reference signal point (dashed histogram) is shown for comparison.

Table 7.1: Observed and predicted yields in the $\not\!\!E_{\mathrm{T}}$ signal bins for H_T >500 GeV, $3 \leq N_{\mathrm{j}} \leq 5$, and $N_b = 2$. The first uncertainty on each prediction is statistical and the second is the full systematic uncertainty. The background component estimates are shown separately. The expected signal yields and their statistical uncertainty are shown for two T1tttt SMS points labeled by $(m_{\tilde{g}}, m_{\mathrm{LSP}})$ in GeV.

$\not\!\!E_{\mathrm{T}}$:	[150,250)	[250,350)	[350,450)	$\geq$ 450 GeV
1 ℓ	1012±31±53	220±16±26	38.8±7.5±9.7	6.8±3.3±3.1
Dilepton	251.8±9.3±16.3	67.6±4.6±6.7	13.5±1.8±1.8	2.1±0.6±0.2
Single Tau	160.7±3.4±9.5	51.2±2.1±11.6	13.3±1.1±6.5	2.5±0.5±0.6
Z + jets	3.9±0.3±3.9	0.8±0.2±0.8	0.2±0.1±0.2	< 0.1
QCD multijet	$1.6 \pm 3.1 \pm 3.1$		$0.0 \pm 1.2 \pm 1.2$	
Total Prediction	1429±33±56	339±17±30	65.7±7.8±11.8	11.4±3.4±3.2
Data, **total** (μ, e)	**1420** (800, 620)	**350** (193, 157)	**67** (34, 33)	**17** (9, 8)
T1tttt $(1150, 500)$	0.8±0.1	0.7±0.1	0.9±0.1	0.5±0.1
T1tttt $(1100, 100)$	0.9±0.1	1.0±0.1	1.2±0.1	1.4±0.1

Table 7.2: Observed and predicted yields in the $\not\!\!E_{\mathrm{T}}$ signal bins for H_T >750 GeV, $3 \leq N_{\mathrm{j}} \leq 5$, and $N_b = 2$. The first uncertainty on each prediction is statistical and the second is the full systematic uncertainty. The background component estimates are shown separately. The expected signal yields and their statistical uncertainty are shown for two T1tttt SMS points labeled by $(m_{\tilde{g}}, m_{\mathrm{LSP}})$ in GeV.

$\not\!\!E_{\mathrm{T}}$:	[150,250)	[250,350)	[350,450)	$\geq$ 450 GeV
1 ℓ	182±14±12	63.8±9.9±8.9	14.0±4.8±3.8	4.1±2.6±1.9
Dilepton	36.1±3.1±3.8	20.6±2.6±3.4	5.1±1.0±1.1	1.3±0.4±0.1
Single Tau	29.1±1.4±4.7	10.0±0.8±1.9	2.8±0.4±0.9	1.5±0.3±0.4
Z + jets	1.0±0.2±1.0	0.2±0.1±0.2	< 0.1	< 0.1
QCD multijet	< 1	< 0.1	< 0.1	< 0.1
Total Prediction	248±15±14	95±10±10	22.0±4.9±4.0	6.9±2.7±1.9
Data, **total** (μ, e)	**270** (145, 125)	**80** (42, 38)	**22** (13, 9)	**9** (4, 5)
T1tttt $(1150, 500)$	0.3±0.0	0.3±0.0	0.3±0.0	0.3±0.0
T1tttt $(1100, 100)$	0.7±0.1	0.7±0.1	0.9±0.1	1.1±0.1

Table 7.3: Observed and predicted yields in the $\not{E}_{\mathrm{T}}$ signal bins for H_T >1000 GeV, $3 \leq N_{\mathrm{j}} \leq 5$, and $N_b = 2$. The first uncertainty on each prediction is statistical and the second is the full systematic uncertainty. The background component estimates are shown separately. The expected signal yields and their statistical uncertainty are shown for two T1tttt SMS points labeled by $(m_{\tilde{g}}, m_{\mathrm{LSP}})$ in GeV.

$\not{E}_{\mathrm{T}}$:	[150,250)	[250,350)	[350,450)	$\geq$ 450 GeV
1 ℓ	29.1±5.6±2.8	12.3±4.7±2.5	8.0±4.2±3.0	2.2±1.9±1.2
Dilepton	10.9±2.0±2.4	9.1±1.7±2.2	2.9±0.8±1.0	0.7±0.4±0.2
Single Tau	5.7±0.6±1.4	1.4±0.2±0.6	0.3±0.1±0.4	0.7±0.3±0.3
Z + jets	0.4±0.1±0.4	0.2±0.1±0.2	< 0.1	< 0.1
QCD multijet	< 0.1	< 0.1	< 0.1	< 0.1
Total Prediction	46.2±5.9±3.9	23.0±5.0±3.4	11.3±4.3±3.2	3.6±2.0±1.3
Data, **total** (μ, e)	**52** (23, 29)	**16** (10, 6)	**6** (3, 3)	**5** (2, 3)
T1tttt (1150, 500)	< 0.1	< 0.1	< 0.1	< 0.1
T1tttt (1100, 100)	0.4±0.1	0.4±0.1	0.4±0.1	0.6±0.1

Table 7.4: Observed and predicted yields in the $\not{E}_{\mathrm{T}}$ signal bins for H_T >500 GeV, $3 \leq N_{\mathrm{j}} \leq 5$, and $N_b \geq 3$. The first uncertainty on each prediction is statistical and the second is the full systematic uncertainty. The expected signal yields and their statistical uncertainty are shown for two T1tttt SMS points labeled by $(m_{\tilde{g}}, m_{\mathrm{LSP}})$ in GeV.

$\not{E}_{\mathrm{T}}$:	[150,250)	[250,350)	[350,450)	$\geq$ 450 GeV
Total Prediction	147.0±3.5±6.6	32.4±1.7±2.9	5.3±0.6±1.0	1.0±0.3±0.3
Data, **total** (μ, e)	**178** (93, 85)	**29** (19, 10)	**7** (4, 3)	**0** (0, 0)
T1tttt (1150, 500)	0.5±0.1	0.5±0.1	0.4±0.0	0.3±0.0
T1tttt (1100, 100)	0.5±0.1	0.8±0.1	0.6±0.1	0.9±0.1

Table 7.5: Observed and predicted yields in the $\not{E}_{\mathrm{T}}$ signal bins for H_T >750 GeV, $3 \leq N_{\mathrm{j}} \leq 5$, and $N_b \geq 3$. The first uncertainty on each prediction is statistical and the second is the full systematic uncertainty. The expected signal yields and their statistical uncertainty are shown for two T1tttt SMS points labeled by $(m_{\tilde{g}}, m_{\mathrm{LSP}})$ in GeV.

$\not{E}_{\mathrm{T}}$:	[150,250)	[250,350)	[350,450)	$\geq$ 450 GeV
Total Prediction	26.0±1.6±1.6	9.5±1.0±1.0	1.9±0.4±0.4	0.6±0.3±0.2
Data, **total** (μ, e)	**32** (13, 19)	**9** (6, 3)	**2** (1, 1)	**0** (0, 0)
T1tttt $(1150, 500)$	0.1±0.0	0.2±0.0	0.2±0.0	0.2±0.0
T1tttt $(1100, 100)$	0.3±0.1	0.5±0.1	0.5±0.1	0.8±0.1

Table 7.6: Observed and predicted yields in the $\not{E}_{\mathrm{T}}$ signal bins for H_T >1000 GeV, $3 \leq N_{\mathrm{j}} \leq 5$, and $N_b \geq 3$. The first uncertainty on each prediction is statistical and the second is the full systematic uncertainty. The expected signal yields and their statistical uncertainty are shown for two T1tttt SMS points labeled by $(m_{\tilde{g}}, m_{\mathrm{LSP}})$ in GeV.

$\not{E}_{\mathrm{T}}$:	[150,250)	[250,350)	[350,450)	$\geq$ 450 GeV
Total Prediction	4.5±0.6±0.4	2.4±0.5±0.4	1.0±0.4±0.3	0.3±0.2±0.1
Data, **total** (μ, e)	**3** (2, 1)	**0** (0, 0)	**0** (0, 0)	**0** (0, 0)
T1tttt $(1150, 500)$	< 0.1	< 0.1	< 0.1	< 0.1
T1tttt $(1100, 100)$	0.2±0.0	0.3±0.1	0.2±0.0	0.4±0.1

Table 7.7: Observed and predicted yields in the $\not{E}_{\mathrm{T}}$ signal bins for H_T >500 GeV, $N_{\mathrm{j}} \geq 6$, and $N_b = 2$. The first uncertainty on each prediction is statistical and the second is the full systematic uncertainty. The background component estimates are shown separately. The expected signal yields and their statistical uncertainty are shown for two T1tttt SMS points labeled by $(m_{\tilde{g}}, m_{\mathrm{LSP}})$ in GeV.

$\not{E}_{\mathrm{T}}$:	[150,250)	[250,350)	[350,450)	$\geq$ 450 GeV
1 ℓ	230±15±12	40.8±7.0±4.9	11.6±4.3±2.9	$0.2^{+1.4+0.6}_{-0.2-0.2}$
Dilepton	42.3±3.6±6.0	8.3±1.5±1.5	$2.0^{+1.5+1.5}_{-0.7-0.8}$	$0.2^{+1.8+1.9}_{-0.1-0.1}$
Single Tau	47.2±1.8±5.4	8.9±0.7±1.4	1.8±0.3±0.6	0.3±0.1±0.3
Z + jets	0.4±0.1±0.4	< 0.1	< 0.1	< 0.1
QCD multijet	$1.6 \pm 3.1 \pm 3.1$		$0.0 \pm 1.2 \pm 1.2$	
Total Prediction	320±16±14	58.1±7.2±5.3	$15.4^{+4.6+3.3}_{-4.3-3.1}$	$0.7^{+2.3+2.0}_{-0.3-0.3}$
Data, **total** (μ, e)	**350** (189, 161)	**55** (30, 25)	**10** (6, 4)	**1** (0, 1)
T1tttt $(1150, 500)$	2.3±0.1	2.6±0.2	1.8±0.1	1.5±0.1
T1tttt $(1100, 100)$	2.5±0.2	3.4±0.2	3.2±0.2	4.4±0.2

Table 7.8: Observed and predicted yields in the $\not\!\!E_{\mathrm{T}}$ signal bins for H_T >750 GeV, $N_{\mathrm{j}} \geq 6$, and $N_b = 2$. The first uncertainty on each prediction is statistical and the second is the full systematic uncertainty. The background component estimates are shown separately. The expected signal yields and their statistical uncertainty are shown for two T1tttt SMS points labeled by $(m_{\tilde{g}}, m_{\mathrm{LSP}})$ in GeV.

$\not\!\!E_{\mathrm{T}}$:	[150,250)	[250,350)	[350,450)	$\geq$ 450 GeV
1 ℓ	81.0±9.1±5.5	18.6±4.8±2.6	7.9±3.6±2.1	$0.2^{+1.4+0.6}_{-0.2-0.1}$
Dilepton	14.9±2.0±2.6	4.1±1.0±1.0	$1.0^{+0.8+0.9}_{-0.4-0.4}$	$0.1^{+1.7+1.8}_{-0.1-0.1}$
Single Tau	18.7±1.2±3.3	3.5±0.4±0.7	1.6±0.3±0.7	0.3±0.1±0.2
Z + jets	0.2±0.1±0.2	< 0.1	< 0.1	< 0.1
QCD multijet	< 1	< 0.1	< 0.1	< 0.1
Total Prediction	114.8±9.4±6.9	26.3±4.9±2.9	$10.6^{+3.7+2.4}_{-3.6-2.3}$	$0.6^{+2.2+1.9}_{-0.2-0.2}$
Data, **total** (μ, e)	**141** (76, 65)	**26** (13, 13)	**9** (6, 3)	**1** (0, 1)
T1tttt $(1150, 500)$	1.4±0.1	1.6±0.1	1.3±0.1	1.3±0.1
T1tttt $(1100, 100)$	2.2±0.2	3.1±0.2	3.0±0.2	4.2±0.2

Table 7.9: Observed and predicted yields in the $\not{E}_{\mathrm{T}}$ signal bins for H_T >1000 GeV, $N_{\mathrm{j}} \geq 6$, and $N_b = 2$. The first uncertainty on each prediction is statistical and the second is the full systematic uncertainty. The background component estimates are shown separately. The expected signal yields and their statistical uncertainty are shown for two T1tttt SMS points labeled by $(m_{\tilde{g}}, m_{\mathrm{LSP}})$ in GeV.

$\not{E}_{\mathrm{T}}$:	[150,250)	[250,350)	[350,450)	$\geq$ 450 GeV
1 ℓ	32.5±6.0±3.1	6.7±3.0±1.3	1.6±1.5±0.6	$0.0^{+1.1+0.6}_{-0.0-0.0}$
Dilepton	4.0±1.1±1.4	$2.3\pm0.8^{+1.4}_{-1.0}$	$0.2^{+1.8+2.1}_{-0.2-0.2}$	$0.0^{+1.9+2.0}_{-0.0-0.0}$
Single Tau	6.6±0.7±1.4	1.0±0.2±0.6	0.4±0.1±0.3	< 0.1
Z + jets	< 0.1	< 0.1	< 0.1	< 0.1
QCD multijet	< 0.1	< 0.1	< 0.1	< 0.1
Total Prediction	43.2±6.1±3.7	$9.9\pm3.1^{+2.0}_{-1.7}$	$2.2^{+2.3+2.2}_{-1.6-0.7}$	$0.1^{+2.2+2.1}_{-0.1-0.1}$
Data, **total** (μ, e)	**46** (24, 22)	**11** (5, 6)	**4** (3, 1)	**1** (0, 1)
T1tttt (1150, 500)	0.6±0.1	0.6±0.1	0.5±0.1	0.7±0.1
T1tttt (1100, 100)	1.6±0.1	2.0±0.1	2.2±0.2	3.2±0.2

Table 7.10: Observed and predicted yields in the $\not{E}_{\mathrm{T}}$ signal bins for H_T >500 GeV, $N_{\mathrm{j}} \geq 6$, and $N_b \geq 3$. The first uncertainty on each prediction is statistical and the second is the full systematic uncertainty. The expected signal yields and their statistical uncertainty are shown for two T1tttt SMS points labeled by $(m_{\tilde{g}}, m_{\mathrm{LSP}})$ in GeV.

$\not{E}_{\mathrm{T}}$:	[150,250)	[250,350)	[350,450)	$\geq$ 450 GeV
Total Prediction	71.1±3.5±8.3	12.4±1.6±1.8	3.1±0.9±0.7	$0.1^{+0.5+0.4}_{-0.0-0.0}$
Data, **total** (μ, e)	**84** (47, 37)	**16** (7, 9)	**2** (1, 1)	**0** (0, 0)
T1tttt (1150, 500)	2.8±0.1	3.0±0.2	1.9±0.1	1.5±0.1
T1tttt (1100, 100)	3.9±0.2	4.1±0.2	4.0±0.2	4.7±0.2

Table 7.11: Observed and predicted yields in the $\not\!\!E_{\mathrm{T}}$ signal bins for H_T >750 GeV, $N_{\mathrm{j}} \geq 6$, and $N_b \geq 3$. The first uncertainty on each prediction is statistical and the second is the full systematic uncertainty. The expected signal yields and their statistical uncertainty are shown for two T1tttt SMS points labeled by $(m_{\tilde{g}}, m_{\mathrm{LSP}})$ in GeV.

$\not\!\!E_{\mathrm{T}}$:	[150,250)	[250,350)	[350,450)	$\geq$ 450 GeV
Total Prediction	25.9±2.1±3.1	5.9±1.1±1.0	2.1±0.7±0.5	$0.1^{+0.5+0.4}_{-0.0-0.0}$
Data, **total** (μ, e)	**37** (18, 19)	**12** (5, 7)	**2** (1, 1)	**0** (0, 0)
T1tttt $(1150, 500)$	1.9±0.1	2.1±0.1	1.4±0.1	1.4±0.1
T1tttt $(1100, 100)$	3.5±0.2	3.8±0.2	3.6±0.2	4.5±0.2

Table 7.12: Observed and predicted yields in the $\not\!\!E_{\mathrm{T}}$ signal bins for H_T >1000 GeV, $N_{\mathrm{j}} \geq 6$, and $N_b \geq 3$. The first uncertainty on each prediction is statistical and the second is the full systematic uncertainty. The expected signal yields and their statistical uncertainty are shown for two T1tttt SMS points labeled by $(m_{\tilde{g}}, m_{\mathrm{LSP}})$ in GeV.

$\not\!\!E_{\mathrm{T}}$:	[150,250)	[250,350)	[350,450)	$\geq$ 450 GeV
Total Prediction	10.4±1.5±1.5	2.4±0.7±0.5	$0.4^{+0.5+0.4}_{-0.3-0.2}$	$0.0^{+0.5+0.5}_{-0.0-0.0}$
Data, **total** (μ, e)	**14** (5, 9)	**4** (1, 3)	**1** (0, 1)	**0** (0, 0)
T1tttt $(1150, 500)$	0.7±0.1	0.8±0.1	0.6±0.1	0.8±0.1
T1tttt $(1100, 100)$	2.5±0.2	2.6±0.2	2.5±0.2	3.4±0.2

Chapter 8

Interpretation

To understand the sensitivity of this analysis to natural SUSY, it is useful to interpret its results in the context of relevant SUSY scenarios. This is done using the T1tttt, T1t1t, and T5tttt simplified models introduced in Sec. 2.3.5, which consist of gluino pair production decaying through top squarks to a final state of 4 top quarks and 2 LSPs. To interpret the results in terms of a given SUSY scenario, its signal yield and corresponding systematic uncertainty are required. The signal acceptance times efficiency and derivation of the corresponding systematic uncertainties are described in Sec. 8.1 and 8.2, respectively. The result of the interpretation in a SUSY scenario is an upper limit on the cross section and a decision on whether that scenario can be excluded by comparing to the predicted theoretical cross section, as described in Sec. 8.3.

8.1 Acceptance times Efficiency

Figures 8.1 and 8.2 show the signal acceptance times efficiency in the T1tttt $m(\tilde{\chi}_1^0)$ vs $m(\tilde{g})$ plane for $N_b = 2$ and $N_b \geq 3$, respectively, with $H_T > 500$ GeV and $N_\mathrm{j} \geq 6$. Each of the three $\not{E}_\mathrm{T}$ signal bins is shown separately. These plots illustrate that the greater the $m(\tilde{g}) - m(\tilde{\chi}_1^0)$ mass splitting, the more energy is available to contribute to the H_T and $\not{E}_\mathrm{T}$ of the event. Figures 8.3 and 8.4 show the signal acceptance times efficiency in the T1t1t $m(\tilde{\chi}_1^0)$ vs $m(\tilde{t})$ plane for $N_b = 2$ and $N_b \geq 3$, respectively, with $H_T > 500$ GeV and $N_\mathrm{j} \geq 6$. Again, lower $m(\tilde{\chi}_1^0)$ is correlated with greater $\not{E}_\mathrm{T}$ and H_T and hence higher efficiency. The stop mass is also somewhat correlated with the event kinematics, as a higher $m(\tilde{t})$ increases the momentum of the $\tilde{\chi}_1^0$ and hence the $\not{E}_\mathrm{T}$. Figures 8.5 and 8.6 show the signal acceptance times efficiency in the T5tttt $m(\tilde{t})$ vs $m(\tilde{g})$ plane for $N_b = 2$ and $N_b \geq 3$, respectively, with $H_T > 500$ GeV and $N_\mathrm{j} \geq 6$. These plots illustrate the same effects of varying the gluino and stop masses as the above two models. The acceptance times efficiency maps for the higher H_T thresholds can be found in Ref. [123] and behave similarly to those for $H_T > 500$ GeV in all three SMSs but with a smaller normalization.

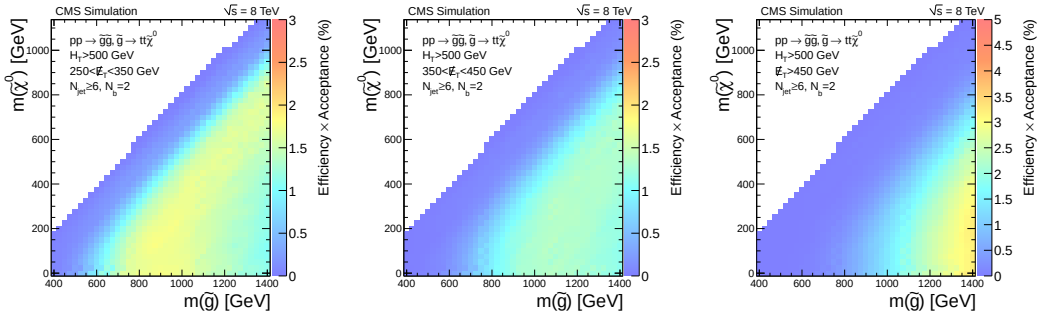

(a) (b) (c)

Figure 8.1: Signal acceptance times efficiency for the three $\not{E}_{\mathrm{T}}$ signal regions for $H_T > 500$ GeV, $N_{\mathrm{j}} \geq 6$, and $N_b = 2$ across the T1tttt $m(\tilde{\chi}_1^0)$ vs $m(\tilde{g})$ plane.

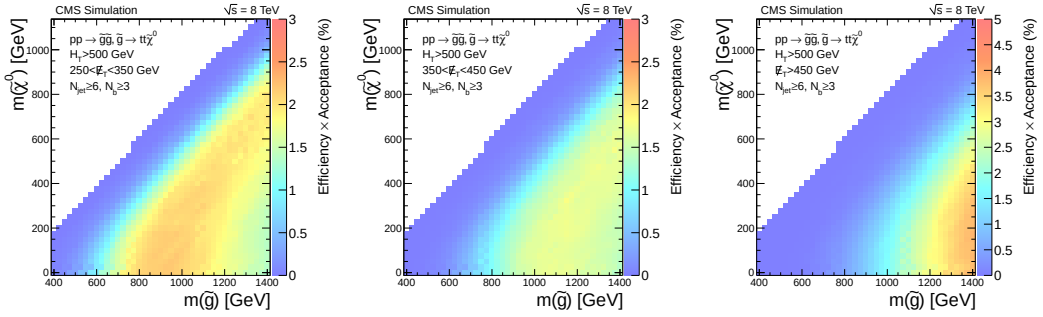

(a) (b) (c)

Figure 8.2: Signal acceptance times efficiency for the three $\not{E}_{\mathrm{T}}$ signal regions for $H_T > 500$ GeV, $N_{\mathrm{j}} \geq 6$, and $N_b \geq 3$ across the T1tttt $m(\tilde{\chi}_1^0)$ vs $m(\tilde{g})$ plane.

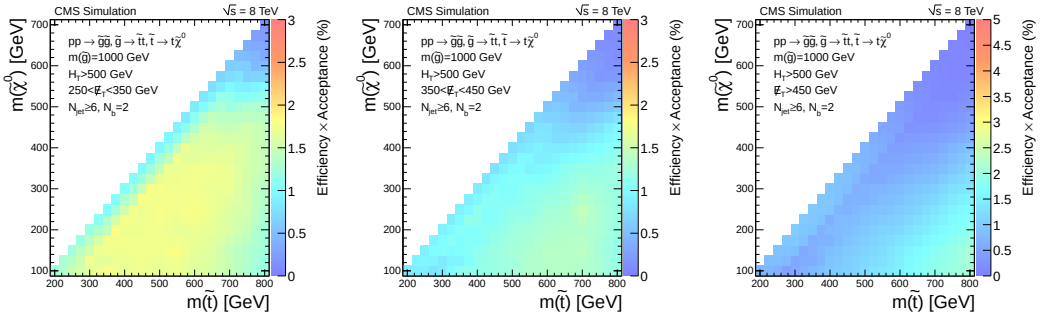

(a) (b) (c)

Figure 8.3: Signal acceptance times efficiency for the three $\not{E}_{\mathrm{T}}$ signal regions for $H_T > 500$ GeV, $N_{\mathrm{j}} \geq 6$, and $N_b = 2$ across the T1t1t $m(\tilde{\chi}_1^0)$ vs $m(\tilde{t})$ plane.

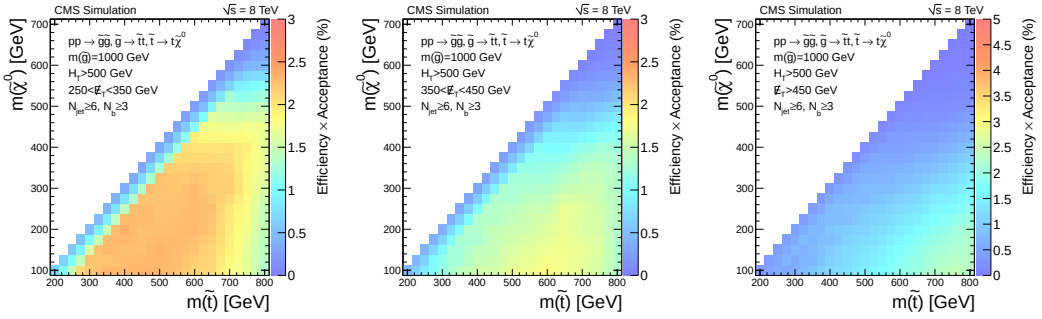

(a) (b) (c)

Figure 8.4: Signal acceptance times efficiency for the three $\not{E}_{\mathrm{T}}$ signal regions for $H_T > 500$ GeV, $N_{\mathrm{j}} \geq 6$, and $N_b \geq 3$ across the T1t1t $m(\tilde{\chi}_1^0)$ vs $m(\tilde{t})$ plane.

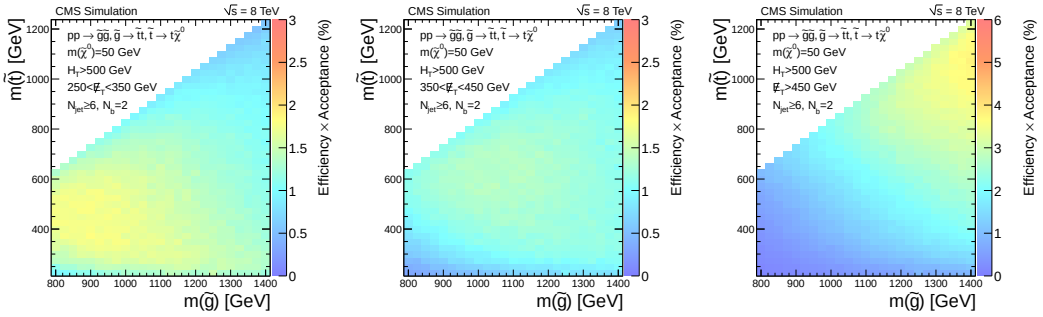

(a) (b) (c)

Figure 8.5: Signal acceptance times efficiency for the three $\not{E}_{\mathrm{T}}$ signal regions for $H_T > 500$ GeV, $N_{\mathrm{j}} \geq 6$, and $N_b = 2$ across the T5tttt $m(\tilde{t})$ vs $m(\tilde{g})$ plane.

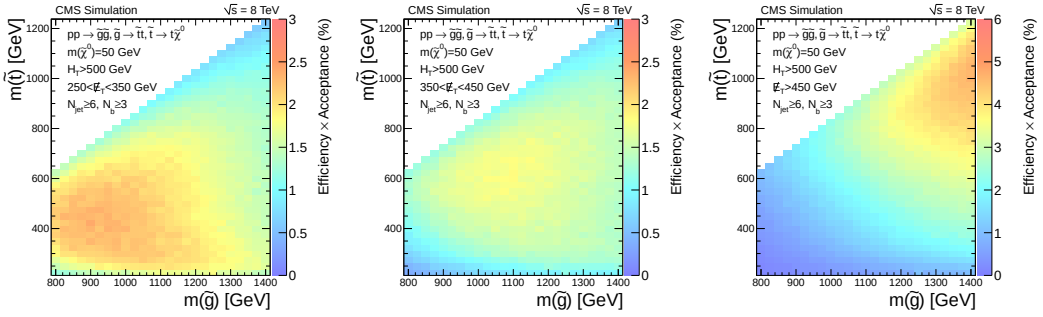

(a) (b) (c)

Figure 8.6: Signal acceptance times efficiency for the three $\not{E}_{\mathrm{T}}$ signal regions for $H_T > 500$ GeV, $N_{\mathrm{j}} \geq 6$, and $N_b \geq 3$ across the T5tttt $m(\tilde{t})$ vs $m(\tilde{g})$ plane.

8.2 Signal Systematic Uncertainties

This section describes the systematic uncertainties on the signal yield that are used in the calculation of the signal cross section limits. For brevity, this thesis does not show every systematic uncertainty in every signal region, but instead uses a set of example plots to illustrate the important behavior of the uncertainties across parameter space. The systematic uncertainties on the signal yield are due to:

- **Jet and $\not\!\!E_{\mathbf{T}}$ energy scale:** The uncertainty due to the $\not\!\!E_{\mathrm{T}}$ and jet energy scale is evaluated as described in Sec. 6.1.3. Figures 8.7, 8.8, and 8.9 plot this uncertainty in the T1tttt, T1t1t, and T5tttt SMS, respectively, for $N_b = 2$ and $H_T > 500$ GeV. The uncertainties for the $N_b \geq 3$ selection have the same qualitative behavior. In all of these models, this uncertainty is highest for the case of small $m(\tilde{g}) - m(\tilde{\chi}_1^0)$ mass splitting, in which the N_{j}, H_T, and $\not\!\!E_{\mathrm{T}}$ distributions are most steeply falling.

- **PU re-weighting:** The systematic uncertainty due to the modeling of the PU distribution in simulation is evaluated in the same way as Sec. 6.2.1. This is a subdominant systematic and is typically on the order of 5% or less.

- **b-tagging scale factors:** The systematic uncertainty due to the b-tagging efficiency and mistag scale factors is evaluated in the same way as described

in Sec. 6.4, with one alteration. Namely, the uncertainty on the scale factors is inflated to account for potential differences between the full simulation and the fast simulation used to produce the signal samples. This systematic is small for the $N_b = 2$ selection because of the presence of four b quarks in the signal, but can be significant for the $N_b \geq 3$ selection. Figures 8.10, 8.11, and 8.12 plot this uncertainty in the T1tttt, T1t1t, and T5tttt SMS, respectively, for $N_b \geq 3$ and $H_T > 500$ GeV. This uncertainty is largest in T1tttt at very small $m(\tilde{g}) - m(\tilde{\chi}_1^0)$ due to the lower average b-jet p_T with correspondingly larger scale factor uncertainty.

- **Luminosity:** The uncertainty on the integrated luminosity is 2.6% [124].

- **Lepton efficiency:** The electron identification and reconstruction efficiency in the signal sample is scaled to match that in the data by $98 \pm 3\%$ for barrel electrons and $86 \pm 7\%$ for endcap electrons. The muon identification and reconstruction efficiency in the signal sample is scaled to match that in the data by $95 \pm 3\%$. The uncertainty on the muon and electron efficiency scale factors is taken to be fully correlated. These scale factors were determined for fast simulation in the studies presented in Ref. [120]. The uncertainty on the signal yield in all T1tttt, T1t1t, and T5tttt scan points from this effect is consistently close to 3.5%, which is taken to be the systematic uncertainty.

- **Trigger efficiency:** The triggers used to select signal events have both a muon or electron component and a H_T ($+\not{E}_{\mathrm{T}}$) hadronic component, both of which cause some inefficiency in selecting signal events. The signal selection efficiency is scaled by $98 \pm 0.3\%$ to account for the hadronic component of the triggers. To account for the efficiency of the electron component of the triggers, the yield of simulated signal events with an electron is scaled by a factor of $96 \pm 5\%$. Similarly, signal events with a muon are scaled by a factor of $98 \pm 4\%$ for $|\eta^{\mu}| < 0.9$ and $84 \pm 4\%$ for $|\eta^{\mu}| > 0.9$. The uncertainties on the muon and electron trigger legs are taken to be correlated. These trigger efficiencies were determined in the studies presented in Ref. [120]. The uncertainty on the signal yield in all T1tttt, T1t1t, and T5tttt scan points due to the trigger efficiency is consistently between 4-5%. Therefore 5% is taken to be the systematic uncertainty for all models. Together, the trigger efficiency and lepton efficiency scale factors account for a roughly 10% decrease in the signal yields of all of the SMS scan points.

- **PDFs:** The uncertainty on the parton distribution functions leads to an uncertainty on the event kinematics, and hence efficiency times acceptance, of signal events. This uncertainty is evaluated using the procedure described in Ref. [125]. Figures 8.13 and 8.14 plot the uncertainty on the signal efficiency times acceptance due to the PDFs in the T1tttt and T1t1t SMS, respectively,

for $H_T > 500$ GeV. For simplicity, in each $\not{E}_{\mathrm{T}}$ signal bin, the plane is divided into three regions in which a flat uncertainty of 50, 30, or 15% is assigned. This helps to smooth the significant point-to-point fluctuations in the PDF uncertainty. Larger uncertainties arise at smaller $m(\tilde{g}) - m(\tilde{\chi}_1^0)$ due to the increased reliance on the kinematic tails for acceptance. Additionally, the uncertainty is sufficiently similar between the $N_b = 2$ and $N_b \geq 3$ bins such that the same PDF uncertainty is used for each. In T5tttt the uncertainty due to the PDFs is relatively flat across all model points, and a 20% systematic uncertainty due to this effect has been assigned to every signal region for every model point. A more detailed description of the procedure used to determine the PDF uncertainties is given below in Sec. 8.2.1.

- **ISR:** Because this search has signal regions with stringent requirements on $\not{E}_{\mathrm{T}}$ and H_T, events with significant ISR can make an important contribution to the signal acceptance, particularly for models with small mass splitting between the gluino and LSP. Therefore, it is important to assess a systematic uncertainty on the signal yield to account for how well the signal MC models ISR effects. To account for the differences in ISR in data and MC, this analysis follows the official CMS SUSY group recommended ISR reweighting procedure for the signal MC. The procedure reweights each event as a function of gluino pair p_T by amounts decreasing from 1.0 ± 0.0 for

$p_T < 120$ GeV down to 0.8 ± 0.2 for $p_T > 250$ GeV. Because some weights are non-unity, the reweighting also leads to a change in the central value of the signal efficiency, which is commensurate with the value of the uncertainty. Figures 8.15, 8.16, and 8.17 plot this uncertainty in the T1tttt, T1t1t, and T5tttt SMS, respectively, for $N_b = 2$ and $H_T > 500$ GeV. The uncertainties for the $N_b \geq 3$ selection are extremely similar. The uncertainty becomes large for small $m(\tilde{g}) - m(\tilde{\chi}_1^0)$, where ISR is necessary to sufficiently boost the system to generate enough $\not{E}_{\mathrm{T}}$ to pass the selection. In T5tttt, where this mass splitting is large because the LSP mass is fixed at 50 GeV, the uncertainty due to ISR is small across the entire model space.

Only the uncertainties for the $H_T > 500$ GeV selection are shown because those for the higher H_T thresholds show similar qualitative behavior and larger statistical fluctuations due to lower efficiency.

8.2.1 PDF Uncertainty Calculation

The uncertainty on the signal efficiency times acceptance due to the PDFs is evaluated using the PDF4LHC Working Group Interim Recommendations described in Ref. [125]. Three PDF sets are used in this calculation, namely CTEQ6.6, MSTW2008 [126], and NNPDF2.0 [127]. An envelope defined by the central values and eigenvector variations of the three PDF sets is used to determine the uncer-

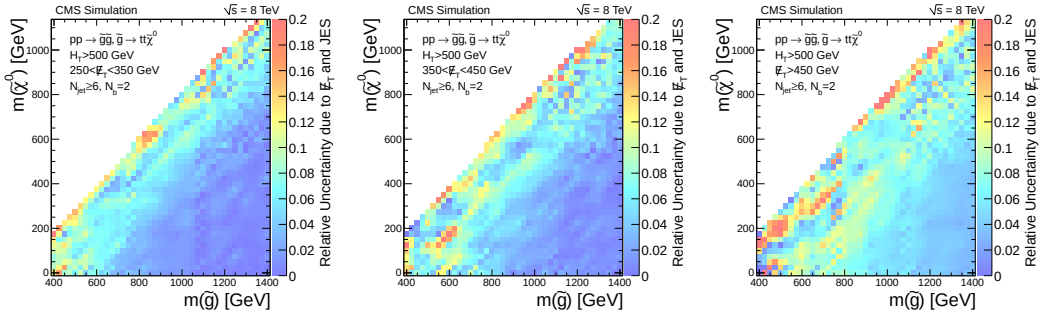

(a) (b) (c)

Figure 8.7: $\not{E}_{\mathrm{T}}$ and jet energy scale signal uncertainties for the three $\not{E}_{\mathrm{T}}$ signal regions for $H_T > 500$ GeV, $N_{\mathrm{j}} \geq 6$, and $N_b = 2$ across the T1tttt $m(\tilde{\chi}_1^0)$ vs $m(\tilde{g})$ plane.

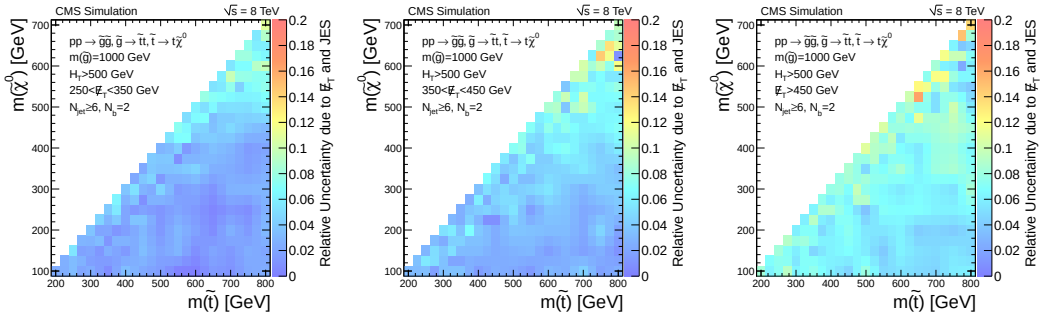

(a) (b) (c)

Figure 8.8: $\not{E}_{\mathrm{T}}$ and jet energy scale signal uncertainties for the three $\not{E}_{\mathrm{T}}$ signal regions for $H_T > 500$ GeV, $N_{\mathrm{j}} \geq 6$, and $N_b = 2$ across the T1t1t $m(\tilde{\chi}_1^0)$ vs $m(\tilde{t})$ plane.

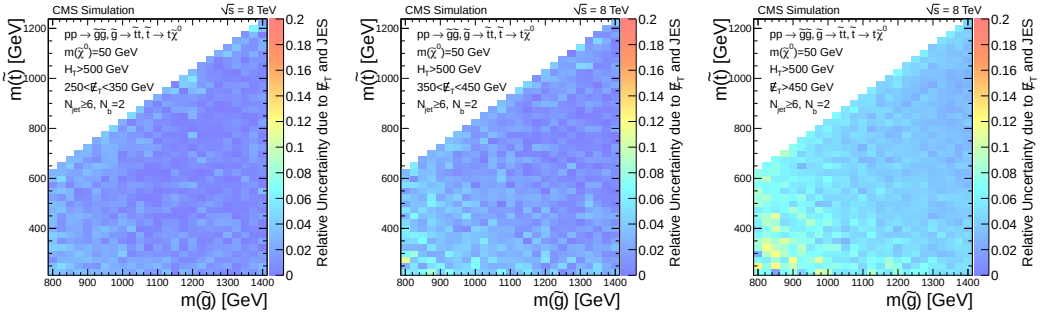

(a) (b) (c)

Figure 8.9: $\not{E}_{\mathrm{T}}$ and jet energy scale signal uncertainties for the three $\not{E}_{\mathrm{T}}$ signal regions for $H_T > 500$ GeV, $N_{\mathrm{j}} \geq 6$, and $N_b = 2$ across the T5tttt $m(\tilde{t})$ vs $m(\tilde{g})$ plane.

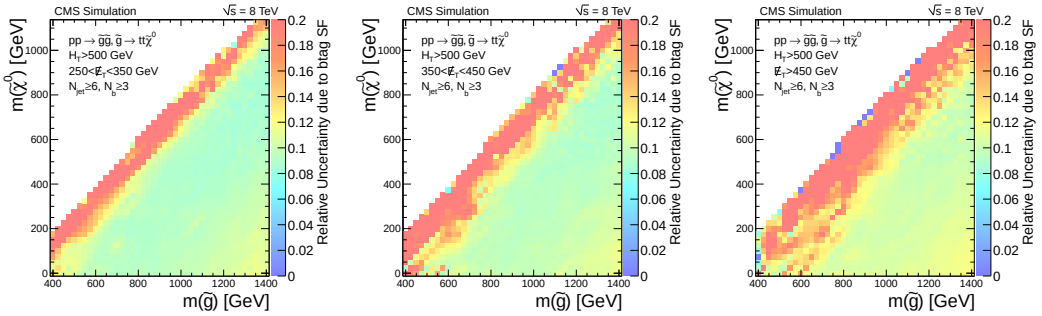

(a) (b) (c)

Figure 8.10: Uncertainty on the signal yield due to the b-tagging scale factors for the three $\not{E}_{\mathrm{T}}$ signal regions for $H_T > 500$ GeV, $N_{\mathrm{j}} \geq 6$, and $N_b \geq 3$ across the T1tttt $m(\tilde{\chi}_1^0)$ vs $m(\tilde{g})$ plane.

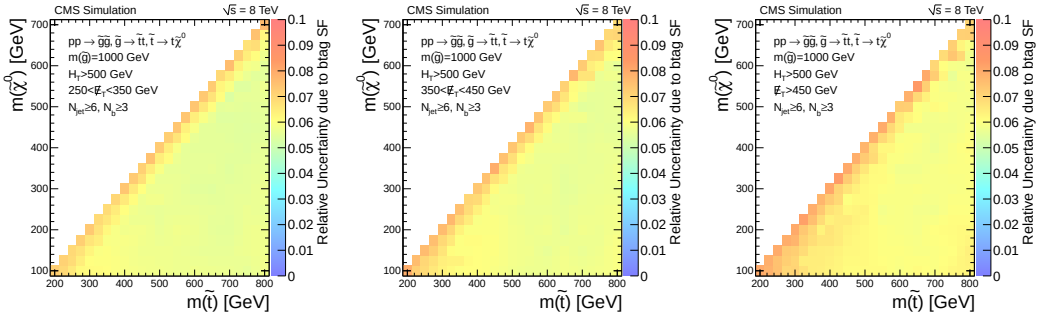

(a) (b) (c)

Figure 8.11: Uncertainty on the signal yield due to the b-tagging scale factors for the three $\not\!\!E_{\mathrm{T}}$ signal regions for $H_T > 500$ GeV, $N_{\mathrm{j}} \geq 6$, and $N_b \geq 3$ across the T1t1t $m(\tilde{\chi}_1^0)$ vs $m(\tilde{t})$ plane.

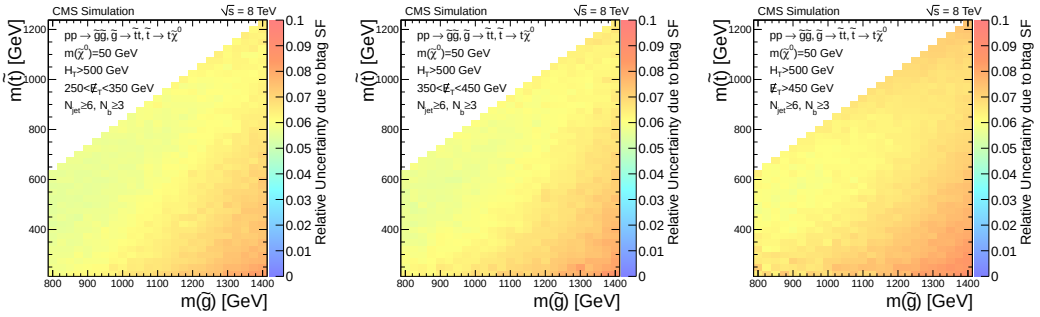

(a) (b) (c)

Figure 8.12: Uncertainty on the signal yield due to the b-tagging scale factors for the three $\not\!\!E_{\mathrm{T}}$ signal regions for $H_T > 500$ GeV, $N_{\mathrm{j}} \geq 6$, and $N_b \geq 3$ across the T5tttt $m(\tilde{t})$ vs $m(\tilde{g})$ plane.

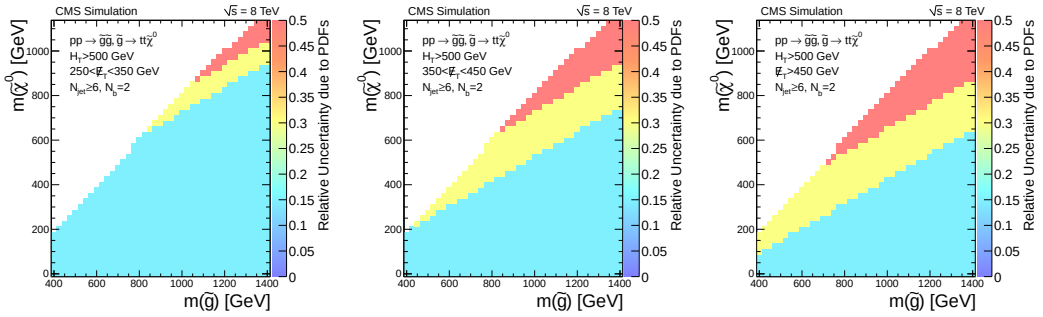

(a) (b) (c)

Figure 8.13: Uncertainty on the signal acceptance time efficiency due to PDFs for the three $\not\!\!E_{\mathrm{T}}$ signal regions for $H_T > 500$ GeV and $N_{\mathrm{j}} \geq 6$ across the T1tttt $m(\tilde{\chi}_1^0)$ vs $m(\tilde{g})$ plane. These uncertainties apply to the $N_b = 2$ and $N_b \geq 3$ selections.

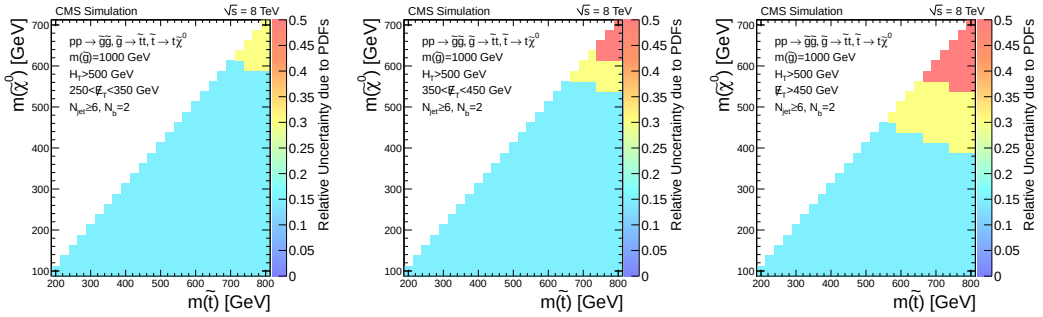

(a) (b) (c)

Figure 8.14: Uncertainty on the signal acceptance time efficiency due to PDFs for the three $\not\!\!E_{\mathrm{T}}$ signal regions for $H_T > 500$ GeV and $N_{\mathrm{j}} \geq 6$ across the T1t1t $m(\tilde{\chi}_1^0)$ vs $m(\tilde{t})$ plane. These uncertainties apply to the $N_b = 2$ and $N_b \geq 3$ selections.

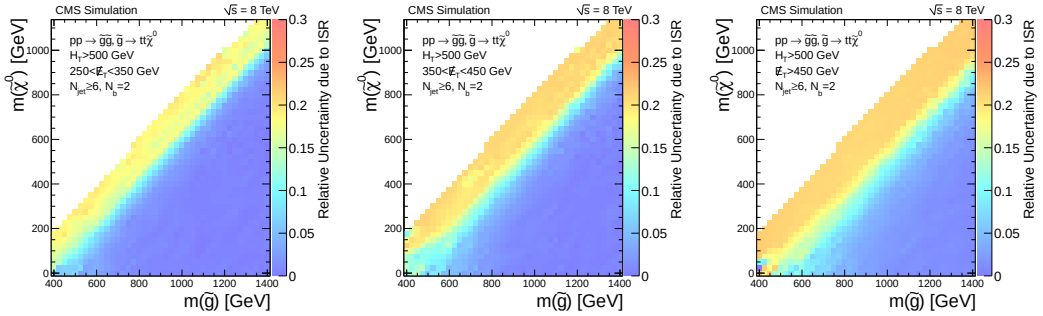

(a) (b) (c)

Figure 8.15: Uncertainty on the signal yield due to ISR modeling for the three $\not\!\!E_{\mathrm{T}}$ signal regions for $H_T > 500$ GeV, $N_{\mathrm{j}} \geq 6$, and $N_b = 2$ across the T1tttt $m(\tilde{\chi}_1^0)$ vs $m(\tilde{g})$ plane.

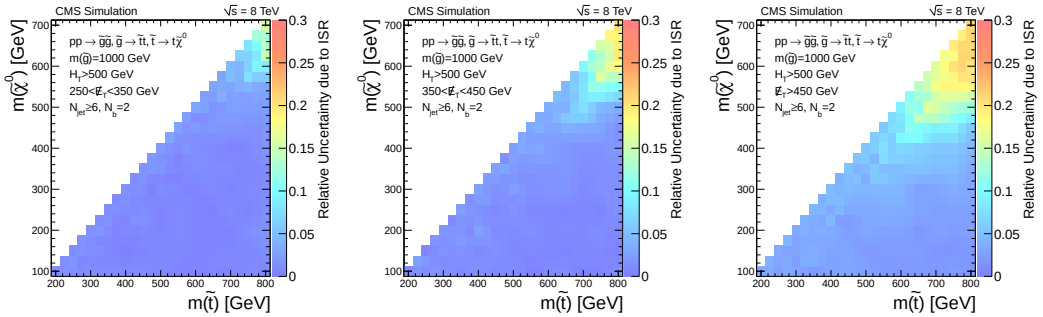

(a) (b) (c)

Figure 8.16: Uncertainty on the signal yield due to ISR modeling for the three $\not\!\!E_{\mathrm{T}}$ signal regions for $H_T > 500$ GeV, $N_{\mathrm{j}} \geq 6$, and $N_b = 2$ across the T1t1t $m(\tilde{\chi}_1^0)$ vs $m(\tilde{t})$ plane.

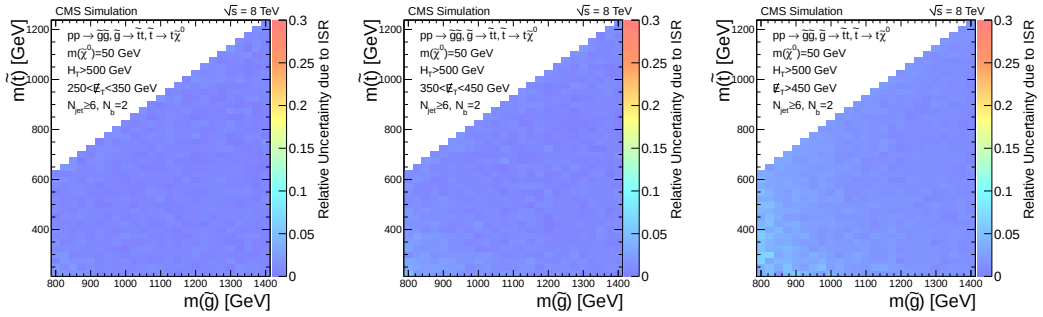

(a) (b) (c)

Figure 8.17: Uncertainty on the signal yield due to ISR modeling for the three $\not{E}_{\mathrm{T}}$ signal regions for $H_T > 500$ GeV, $N_{\mathrm{j}} \geq 6$, and $N_b = 2$ across the T5tttt $m(\tilde{t})$ vs $m(\tilde{g})$ plane.

tainty. This is done because the differences in signal yield between the different PDF sets are as large as the differences arising from their eigenvector variations. The recommended procedure for each PDF set for evaluating the uncertainty due to the variation of its eigenvectors is used.

For both CTEQ and MSTW, the uncertainty from the eigenvector variation is determined from the following equations, taken from [128]:

$$\Delta X^{+}_{\mathrm{max}} = \sqrt{\sum_{i=1}^{N} \left[max(X_i^{+} - X_0, X_i^{-} - X_0, 0) \right]^2} \tag{8.1}$$

$$\Delta X^{-}_{\mathrm{max}} = \sqrt{\sum_{i=1}^{N} \left[max(X_0 - X_i^{+}, X_0 - X_i^{-}, 0) \right]^2} \tag{8.2}$$

Here $X_i^{+(-)}$ represents the signal efficiency times acceptance after the positive (negative) variation of the ith of N eigenvectors. The nominal efficiency times

acceptance is denoted by X_0. The larger of $\Delta X^{+}_{\text{max}}$ and $\Delta X^{-}_{\text{max}}$ is taken to be a symmetric uncertainty due to the eigenvector variations. Because the uncertainty variations provided by the CTEQ set are at the 90% Confidence Level, they must be reduced by a factor of 1.645 to convert to standard 68% Confidence Level uncertainties. For NNPDF, the central value and uncertainty come from the mean and standard deviation of the distribution of the efficiency times acceptance over all of the eigenvector variations.

Using the central value and uncertainty from each of the PDF sets, the total uncertainty is determined from the envelope constructed to have a central value of

$$\begin{aligned} X_{\text{CV}} =& 0.5 \times [max(X_{\text{CTEQ}} + \sigma_{X_{\text{CTEQ}}}, X_{\text{MSTW}} + \sigma_{X_{\text{MSTW}}}, X_{\text{NNPDF}} + \sigma_{X_{\text{NNPDF}}}) \\ & + min(X_{\text{CTEQ}} - \sigma_{X_{\text{CTEQ}}}, X_{\text{MSTW}} - \sigma_{X_{\text{MSTW}}}, X_{\text{NNPDF}} - \sigma_{X_{\text{NNPDF}}})] \end{aligned} \tag{8.3}$$

and symmetric uncertainty given by

$$\begin{aligned} \sigma(X_{\text{CV}}) =& 0.5 \times [max(X_{\text{CTEQ}} + \sigma_{X_{\text{CTEQ}}}, X_{\text{MSTW}} + \sigma_{X_{\text{MSTW}}}, X_{\text{NNPDF}} + \sigma_{X_{\text{NNPDF}}}) \\ & - min(X_{\text{CTEQ}} - \sigma_{X_{\text{CTEQ}}}, X_{\text{MSTW}} - \sigma_{X_{\text{MSTW}}}, X_{\text{NNPDF}} - \sigma_{X_{\text{NNPDF}}})]. \end{aligned} \tag{8.4}$$

To avoid unphysical uncertainties, the bottom edge of the envelope is not allowed to extend below 0. The final total relative uncertainty is taken to be $X_{\text{CV}}/\sigma(X_{\text{CV}})$.

In regions of SMS parameter space which have low signal efficiency, this procedure can result in large variations in the uncertainty for neighboring model points, due to the small number of events over which the PDF variations are averaged. These fluctuations become particularly problematic when the number of selected events is less than the number of eigenvector variations. To mitigate these fluctuations, the uncertainty for a given model point is computed by including its neighboring model points, which should have roughly the same uncertainty due to PDFs. That is to say, the events in the neighboring model points are treated as though they belong to the model point in question when calculating its uncertainty. The increase in event yields and effective averaging between nearby model points reduces the variations to a reasonable level. This averaging, however, is only needed in the T1tttt SMS, which has small efficiencies near its diagonal.

8.3 Exclusion Limits

Limits are set using a modified-frequentist CL_s method [129, 130, 131] with a one-sided profile likelihood ratio test statistic. The inputs to the limit setting are the background predictions, observations in data, and yields from the signal model in question. The limit setting takes the 3 $\not{E}_T$ signal regions for both $N_b = 2$ and $N_b \geq 3$, for a total of 6 signal regions, into account simultaneously in a global

fit to determine a 95% Confidence Level (C.L.) upper limit on the signal cross section separately for each H_T threshold. The final limit in a given signal model is taken from the H_T threshold with the best expected limit.

As mentioned in Sec. 2.3.4, the gluino pair-production cross sections used for setting mass limits are determined using NLO plus NLL calculations. At $m(\tilde{g}) = 1.2$ TeV, near the edge of sensitivity for this analysis, the cross section of 4.4 fb means that only roughly 85 gluino pairs would have been produced in the entire dataset. The theoretical uncertainty on the cross sections is due to renormalization and factorization scale variations and the parton distribution functions [132]. Because massive gluino pair-production probes the poorly constrained tails of the PDFs, the uncertainty on the cross section is quite large at above 20-30% for nearly all of the interesting parameter space. This is illustrated in Fig. 8.18, which shows the pair-production cross section and its theoretical uncertainty as a function of $m(\tilde{g})$.

An important aspect of the limit setting procedure is the treatment of uncertainties. Below is a list describing the handling of uncertainties and their correlations in each of the background predictions as well as the signal yield. Due to the multiple signal bins, it is necessary to take correlations of uncertainties across the different bins into account. Statistical uncertainties are modeled as Poisson

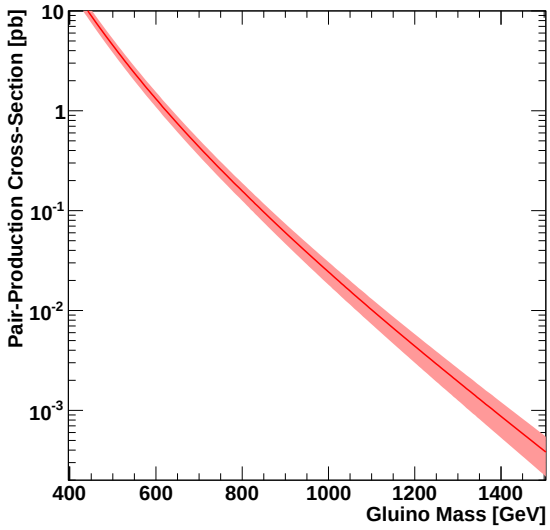

Figure 8.18: Gluino pair-production cross section and its theoretical uncertainty as a function of $m(\tilde{g})$. The solid line represents the central value and the shaded band denotes the uncertainty.

and systematic uncertainties are modeled as multiplicative and lognormal. All correlations listed below are conservatively treated as 100% correlated.

- Signal Yields: Each source of uncertainty on the signal yield is taken to be correlated between all $\not\!\!E_{\mathrm{T}}$ bins. The JES component of the systematic uncertainty is also correlated with the JES systematic uncertainty on the single lepton background prediction. Note that the theoretical uncertainty on the production cross section is not included in the limit calculation, but rather its effect is shown via variations in the observed limit curves.

- Single Lepton: The systematic uncertainty on the prediction is correlated across all bins.

- single τ_ℓ, $\ell + \tau_\ell$, $\ell + \tau_\mathrm{h}$, and lost and ignored dilepton backgrounds: These predictions are each treated separately in the limit code. The systematic uncertainty for each is correlated across all $\not\!\!E_\mathrm{T}$ bins.

- QCD: The QCD contribution is not considered in the limit determination as it is negligible.

- Z+jets prediction: The systematic uncertainty is taken as correlated across all signal bins.

- Background prediction uncertainty between b-tag bins: The uncertainty on the background prediction is treated as 100% correlated between the $N_b = 2$ and $N_b \geq 3$ signal regions for a given $\not\!\!E_\mathrm{T}$ bin. The one exception to this is the uncertainty on the $N_b \geq 3$ predictions due to the uncertainty on R32, which is not correlated with the $N_b = 2$ predictions.

- R32 uncertainty: The systematic uncertainty on the R32 factors used to make the $N_b \geq 3$ predictions has two components: (1) An uncorrelated uncertainty between $\not\!\!E_\mathrm{T}$ bins due to limited simulated event yields. (2) All other sources of uncertainty, which are correlated between $\not\!\!E_\mathrm{T}$ bins.

The effect of signal contamination of the background estimation was quantified as follows. For each of the data driven background estimates, the expected contribution due to signal contamination is subtracted from the prediction and the limits are calculated. The resulting change in the limit contours after accounting for signal contamination is much less than the difference between the median and 1σ expected limit curves. Therefore, signal contamination is neglected in the limits shown here.

The limit curves for each of the three H_T selections in the T1tttt, T1t1t, and T5tttt mass planes are shown in Figs. 8.19, 8.20, and 8.21, respectively. For the final limit on each model point, the H_T selection giving the best expected limit is used. The H_T selection giving the best expected limit at each point in T1tttt, T1t1t, and T5tttt is shown in Figs. 8.22, 8.23, and 8.24, respectively, along with the resulting exclusion contours.

For the vast majority of parameter space, the lowest H_T threshold gives the best expected limit. In T5tttt, however, there is a clear trend of higher H_T selections giving better expected limits at lower stop masses. This is because reducing the stop mass reduces the momentum of the LSPs and increases the momentum of the top quarks produced in the $\tilde{g} \to \tilde{t}t$ decays, which results in lower $\not{E}_{\mathrm{T}}$ and higher H_T on average. This trend is also seen at low stop mass in T1t1t, although with the further complication that for $m(\tilde{t}) - m(\tilde{\chi}_1^0) < 175$ the top

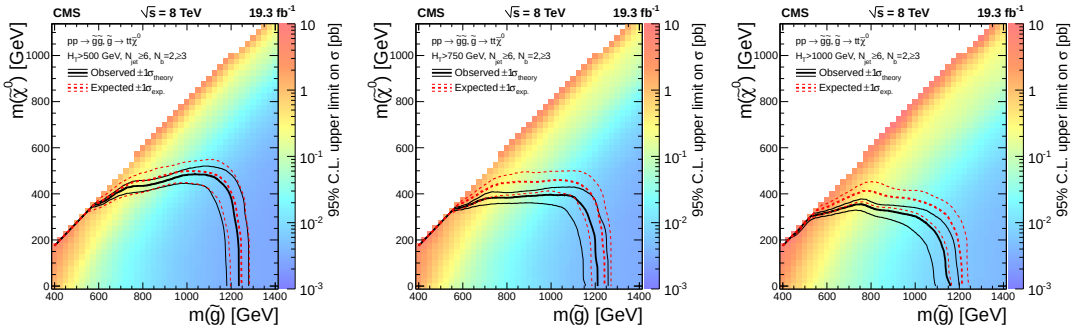

(a) (b) (c)

Figure 8.19: 95% C.L. upper limits on the production cross section in T1tttt for $N_{\mathrm{j}} \geq 6$, N_b bins of 2 and ≥ 3, and (a) $H_T > 500$ GeV, (b) $H_T > 750$ GeV, (c) $H_T > 1000$ GeV. The z axis corresponds to the observed limit. The observed ($\pm 1\sigma$ theory) and expected ($\pm 1\sigma$ experimental) limit contours are also shown.

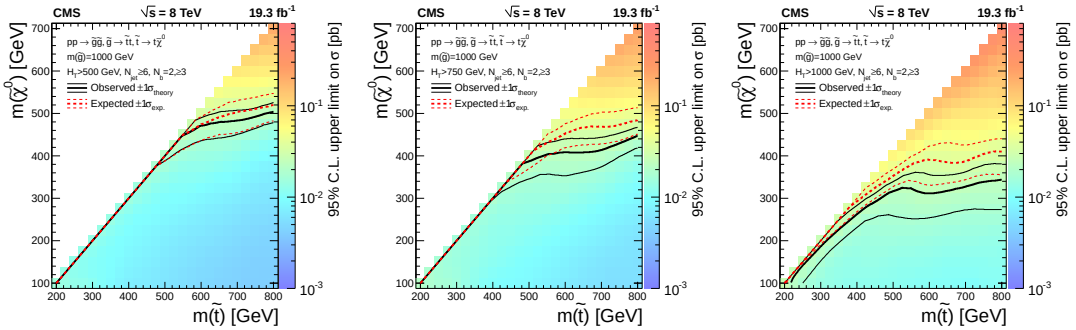

(a) (b) (c)

Figure 8.20: 95% C.L. upper limits on the production cross section in T1t1t for $N_{\mathrm{j}} \geq 6$, N_b bins of 2 and ≥ 3, and (a) $H_T > 500$ GeV, (b) $H_T > 750$ GeV, (c) $H_T > 1000$ GeV. The z axis corresponds to the observed limit. The observed ($\pm 1\sigma$ theory) and expected ($\pm 1\sigma$ experimental) limit contours are also shown.

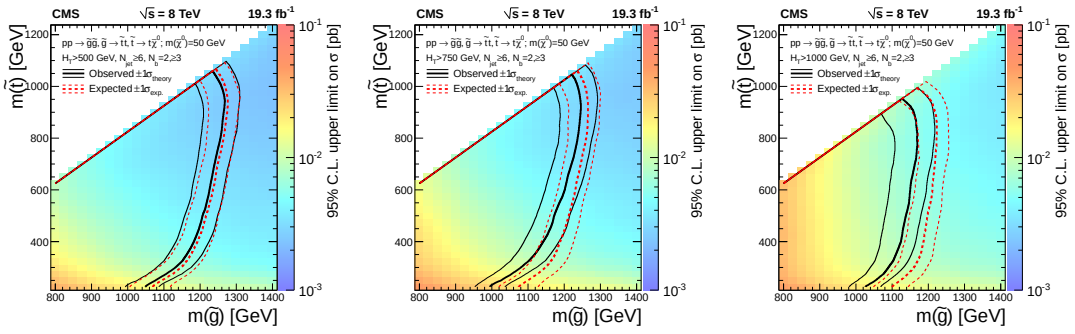

(a) (b) (c)

Figure 8.21: 95% C.L. upper limits on the production cross section in T5tttt for $N_{\mathrm{j}} \geq 6$, N_b bins of 2 and ≥ 3, and (a) $H_T > 500$ GeV, (b) $H_T > 750$ GeV, (c) $H_T > 1000$ GeV. The z axis corresponds to the observed limit. The observed ($\pm 1\sigma$ theory) and expected ($\pm 1\sigma$ experimental) limit contours are also shown.

quark from the stop decay is off mass shell. For small $m(\tilde{g})$ and $m(\tilde{g}) - m(\tilde{\chi}_1^0)$ in T1tttt, where events only pass the $\not\!\!E_{\mathrm{T}}$ requirement due to hard ISR, the resulting extreme correlation between $\not\!\!E_{\mathrm{T}}$ and H_T means the $H_T > 750$ GeV selection gives competitive expected limits to $H_T > 500$ GeV.

The final limit plots indicate the following mass limits, which are conservatively quoted in terms of the $-1\sigma_{\mathrm{theory}}$ exclusion contour on the observed limit. In T1tttt, gluinos of up to 1180 GeV are excluded for low $\tilde{\chi}_1^0$ masses and $\tilde{\chi}_1^0$ masses of up 440 GeV are excluded for 1 TeV gluinos. For the case of on-shell stops in T1t1t, $\tilde{\chi}_1^0$ masses below 380 to 480 GeV are excluded for 1 TeV gluinos, depending on the stop mass. For on-shell stops and $\tilde{\chi}_1^0$ mass of 50 GeV in T5tttt, gluino masses below 1 to 1.2 TeV are excluded, depending on the stop mass. The T1t1t and

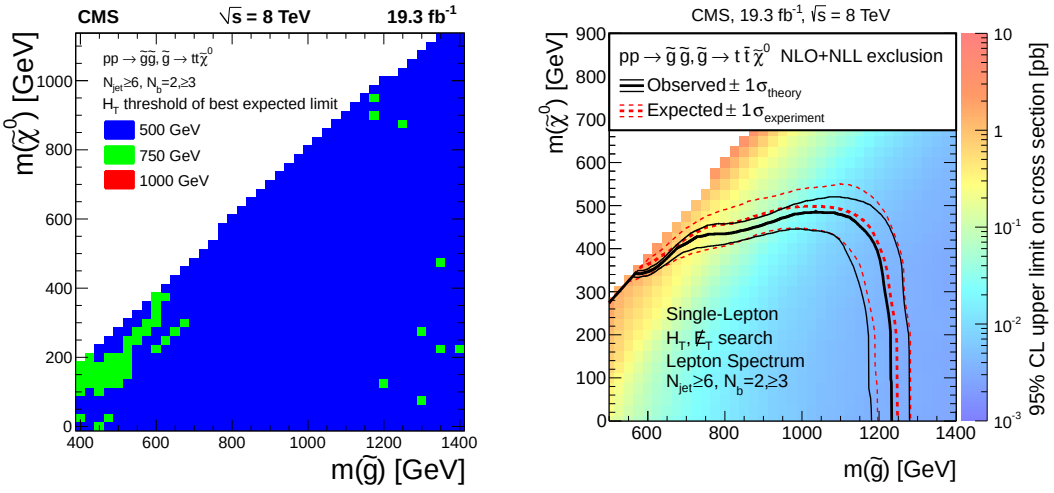

(a) (b)

Figure 8.22: The H_T selection with the best expected 95% C.L. cross section upper limit for $N_\mathrm{j} \geq 6$ and N_b bins of 2 and ≥ 3 is shown in (a) for each point in the T1tttt plane. (b) shows the resulting observed ($\pm 1\sigma$ theory) and expected ($\pm 1\sigma$ experimental) exclusion contours obtained from using the limits from the H_T selections shown in (a) with the observed limit plotted on the z axis.

T5tttt limits are compatible with those in T1tttt for off-shell stops, and illustrate that the gluino and $\tilde{\chi}_1^0$ mass exclusions do not depend strongly on the stop mass. A final noteworthy point is that these results are complementary to direct stop searches [4, 133, 134, 135], which are similarly motivated by naturalness. For the 1 TeV gluino mass in T1t1t, this analysis excludes a larger range of $(m(\tilde{t}), m(\tilde{\chi}_1^0))$ parameter space than current direct stop searches.

In addition to this search, there are two other recent searches at CMS for gluino production and decay through stops in the single lepton channel [1]. One of these

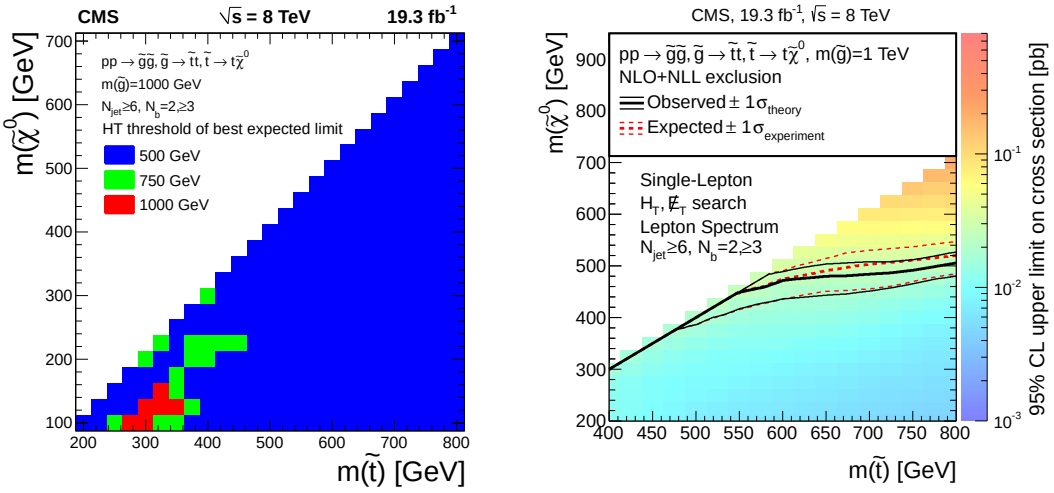

(a) (b)

Figure 8.23: The H_T selection with the best expected 95% C.L. cross section upper limit for $N_\mathrm{j} \geq 6$ and N_b bins of 2 and ≥ 3 is shown in (a) for each point in the T1t1t plane. (b) shows the resulting observed ($\pm 1\sigma$ theory) and expected ($\pm 1\sigma$ experimental) exclusion contours obtained from using the limits from the H_T selections shown in (a) with the observed limit plotted on the z axis.

uses nearly identical signal regions to this search but predicts the backgrounds using a fit to the $\not\!\!E_\mathrm{T}$ distribution in various control samples. Consequently, its exclusion sensitivity is very similar to that shown here. The other search places a stringent requirement on the ϕ angle between the reconstructed W and ℓ, which rejects the vast majority of the single lepton background. The smaller, dilepton dominated background leads to an enhanced exclusion sensitivity of approximately 100 GeV in gluino mass for low LSP masses. Despite this increased exclusion sen-

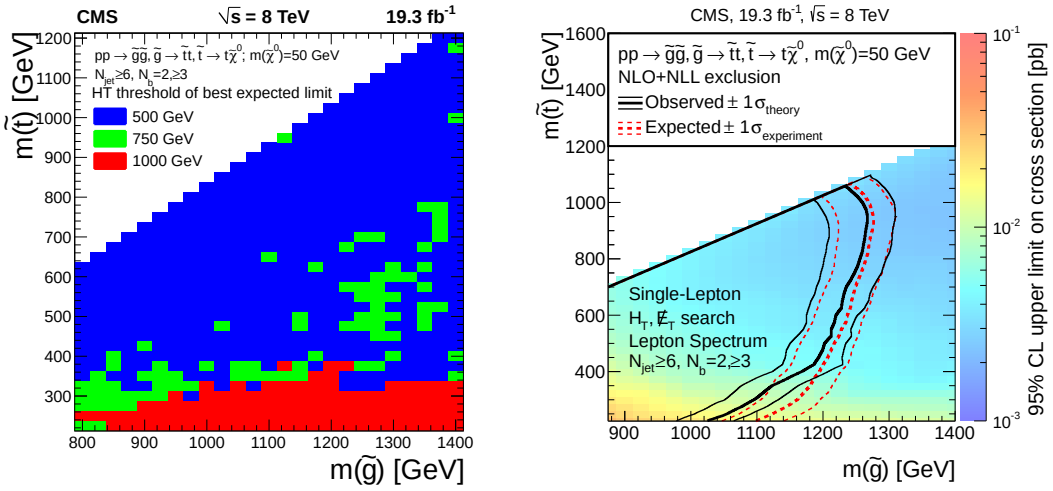

(a) (b)

Figure 8.24: The H_T selection with the best expected 95% C.L. cross section upper limit for $N_j \geq 6$ and N_b bins of 2 and ≥ 3 is shown in (a) for each point in the T5tttt plane. (b) shows the resulting observed ($\pm 1\sigma$ theory) and expected ($\pm 1\sigma$ experimental) exclusion contours obtained from using the limits from the H_T selections shown in (a) with the observed limit plotted on the z axis.

sitivity, having two versions of the search with significantly different background composition is crucial to prepare for the event that an excess is observed in either.

Chapter 9

Conclusion

This thesis describes a search for Supersymmetry in events with a single lepton, large jet multiplicity, and multiple b jets in 19.3 fb^{-1} of pp collisions at $\sqrt{s} = 8$ TeV collected with the CMS experiment. The search targets gluino pair production and decay through top squarks in R-parity conserving SUSY models, as is motivated by naturalness arguments and the $\tilde{\chi}_1^0$ providing a dark matter candidate. Since these types of events would have large H_T and $\not{E}_{\text{T}}$ due to the heavy gluino mass and presence of two $\tilde{\chi}_1^0$, significant requirements are placed on these variables to reduce the Standard Model backgrounds. With the above selection, the dominant background comes from $t\bar{t}$ production.

The major background components to this search are predicted using data-driven methods. The dominant background, consisting of events with exactly one prompt lepton, is predicted by the charged lepton p_T spectrum, after suitable corrections to account for minor differences between charged and neutral leptons

from W-boson decays. The backgrounds coming from events with one or more tau leptons are predicted by emulating tau decays in data control samples using response functions derived in simulation. Another significant background contribution comes from lost and ignored dilepton events, which are predicted by their simulated $\not\!\!E_{\mathrm{T}}$ distribution normalized by the relative data/simulation yields in a suitable control sample. Finally, the QCD multijet background is shown to be negligibly small by extrapolating from a high relative lepton isolation control sample.

The background prediction in each signal region is in good agreement with the observation in data and no evidence for new physics is found. Limits at 95% C.L. are set in the context of three Simplified Model Spectra, each consisting of gluino pair production and decay through top squarks to a four top and two LSP final state. The SMSs are differentiated by their assumptions about the masses of the top squarks, gluinos, and LSPs. In these models, gluino masses below 1150 GeV are excluded for low $\tilde{\chi}_1^0$ masses and $\tilde{\chi}_1^0$ masses below 440 GeV are excluded for a gluino mass of 1 TeV, with fairly weak dependence on the stop mass. This small stop mass dependence makes this search a powerful counterpart to natural SUSY searches targeting direct stop production.

Bibliography

[1] CMS Collaboration, "Search for supersymmetry in pp collisions at $\sqrt{s} = 8$ TeV in events with a single lepton, large jet multiplicity, and multiple b jets", Phys. Lett. B **733** (2014) 328–353, doi:10.1016/j.physletb.2014.04.023, arXiv:1311.4937.

[2] CMS Collaboration, "Search for supersymmetry in pp collisions at $\sqrt{s} = 7$ TeV in events with a single lepton, jets, and missing transverse momentum", J. High Energy Phys. **08** (2011) 156, doi:10.1007/JHEP08(2011)156, arXiv:1107.1870.

[3] CMS Collaboration, "Search for supersymmetry in pp collisions at $\sqrt{s} = 7$ TeV in events with a single lepton, jets, and missing transverse momentum", Eur. Phys. J. C **73** (2013) 2404, doi:10.1140/epjc/s10052-013-2404-z, arXiv:1212.6428.

[4] CMS Collaboration, "Search for top-squark pair production in the single-lepton final state in pp collisions at $\sqrt{s} = 8$ TeV", Eur. Phys. J. C **73** (2013) 2677, doi:10.1140/epjc/s10052-013-2677-2, arXiv:1308.1586.

[5] CMS Collaboration, "Search for supersymmetry in final states with a single lepton, b-quark jets, and missing transverse energy in proton-proton collisions at $\sqrt{s} = 7$ TeV", Phys. Rev. D **87** (2013) 052006, doi:10.1103/PhysRevD.87.052006, arXiv:1211.3143.

[6] ATLAS Collaboration, "Multi-channel search for squarks and gluinos in $\sqrt{s} = 7$ TeV pp collisions with the ATLAS detector", Eur. Phys. J. C **73** (2013) 2362, doi:10.1140/epjc/s10052-013-2362-5, arXiv:1212.6149.

[7] ATLAS Collaboration, "Search for light top squark pair production in final states with leptons and b-jets with the ATLAS detector in $\sqrt{s} = 7$ TeV proton-proton collisions", Phys. Lett. B **720** (2013) 13, doi:10.1016/j.physletb.2013.01.049, arXiv:1209.2102.

[8] ATLAS Collaboration, "Further search for supersymmetry at $\sqrt{s} = 7$ TeV in final states with jets, missing transverse momentum and isolated leptons with the ATLAS detector", Phys. Rev. D **86** (2012) 092002, doi:10.1103/PhysRevD.86.092002, arXiv:1208.4688.

[9] ATLAS Collaboration, "Search for direct top squark pair production in final states with one isolated lepton, jets, and missing transverse momentum in $\sqrt{s} = 7$ TeV pp collisions using 4.7 fb^{-1} of ATLAS data", Phys. Rev. Lett. **109** (2012) 211803, doi:10.1103/PhysRevLett.109.211803, arXiv:1208.2590.

[10] V. Pavlunin, "Modeling missing transverse energy in V+jets at CERN LHC", Phys. Rev. D **81** (2010) 035005, doi:10.1103/PhysRevD.81.035005, arXiv:0906.5016.

[11] M. Y. Han and Y. Nambu, "Three-Triplet Model with Double SU(3) Symmetry", Phys. Rev. **139** (1965) B1006–B1010, doi:10.1103/PhysRev.139.B1006.

[12] D. J. Gross and F. Wilczek, "Ultraviolet Behavior of Non-Abelian Gauge Theories", Phys. Rev. Lett. **30** (1973) 1343–1346, doi:10.1103/PhysRevLett.30.1343.

[13] H. D. Politzer, "Reliable Perturbative Results for Strong Interactions?", Phys. Rev. Lett. **30** (1973) 1346–1349, doi:10.1103/PhysRevLett.30.1346.

[14] S. L. Glashow, "Partial-symmetries of weak interactions", Nucl. Phys. **22** (1961) 579 – 588, doi:10.1016/0029-5582(61)90469-2.

[15] S. Weinberg, "A Model of Leptons", Phys. Rev. Lett. **19** (1967) 1264–1266, doi:10.1103/PhysRevLett.19.1264.

[16] A. Salam, "Weak and electromagnetic interactions", in *Elementary Particle Theory: Relativistic Groups and Analyticity, Proceedings of the Eighth Nobel Symposium*, N. Svartholm, ed., pp. 367–377. Almqvist & Wiskell, 1968.

[17] S. Weinberg, *The Quantum Theory of Fields: Foundations*, volume 1. Cambridge University Press, Cambridge, 1995.

[18] S. Weinberg, *The Quantum Theory of Fields: Modern Applications*, volume 2. Cambridge University Press, Cambridge, 1996.

[19] G. Altarelli and M. W. Grunewald, "Precision electroweak tests of the standard model", Phys. Rept. **403-404** (2004) 189–201, doi:10.1016/j.physrep.2004.08.013, arXiv:hep-ph/0404165.

[20] O. Biebel, "Experimental tests of the strong interaction and its energy dependence in electron-positron annihilation", Phys. Rept. **340** (2001) 165–289, doi:10.1016/S0370-1573(00)00072-7.

[21] R. S. Van Dyck, P. B. Schwinberg, and H. G. Dehmelt, "New high-precision comparison of electron and positron g factors", Phys. Rev. Lett. **59** (1987) 26–29, doi:10.1103/PhysRevLett.59.26.

[22] UA1 Collaboration, "Experimental observation of lepton pairs of invariant mass around 95 GeV/c^2 at the CERN SPS collider", Phys. Lett. B **126** (1983) 398 – 410, doi:10.1016/0370-2693(83)90188-0.

[23] CDF Collaboration, "Observation of Top Quark Production in $\overline{p}p$ Collisions with the Collider Detector at Fermilab", Phys. Rev. Lett. **74** (1995) 2626–2631, doi:10.1103/PhysRevLett.74.2626.

[24] CMS Collaboration, "Observation of a new boson at a mass of 125 GeV with the CMS experiment at the LHC", Phys. Lett. B **716** (2012) 30 – 61, doi:10.1016/j.physletb.2012.08.021.

[25] ATLAS Collaboration, "Observation of a new particle in the search for the Standard Model Higgs boson with the ATLAS detector at the LHC", Phys. Lett. B **716** (2012) 1 – 29, doi:10.1016/j.physletb.2012.08.020.

[26] http://en.wikipedia.org/wiki/Standard_Model.

[27] F. Englert and R. Brout, "Broken Symmetry and the Mass of Gauge Vector Mesons", Phys. Rev. Lett. **13** (1964) 321–323, doi:10.1103/PhysRevLett.13.321.

[28] P. W. Higgs, "Broken symmetries, massless particles and gauge fields", Phys. Lett. **12** (1964) 132 – 133, doi:10.1016/0031-9163(64)91136-9.

[29] P. W. Higgs, "Broken Symmetries and the Masses of Gauge Bosons", Phys. Rev. Lett. **13** (1964) 508–509, doi:10.1103/PhysRevLett.13.508.

[30] G. S. Guralnik, C. R. Hagen, and T. W. B. Kibble, "Global Conservation Laws and Massless Particles", Phys. Rev. Lett. **13** (1964) 585–587, doi:10.1103/PhysRevLett.13.585.

[31] P. W. Higgs, "Spontaneous Symmetry Breakdown without Massless Bosons", Phys. Rev. **145** (1966) 1156–1163, doi:10.1103/PhysRev.145.1156.

[32] T. W. B. Kibble, "Symmetry Breaking in Non-Abelian Gauge Theories", Phys. Rev. **155** (1967) 1554–1561, doi:10.1103/PhysRev.155.1554.

[33] D. I. Kazakov, "Beyond the standard model: In search of supersymmetry", (2000), arXiv:hep-ph/0012288. Lectures given at the European School for High Energy Physics, Caramulo, Portugal, Aug.-Sept. 2000.

[34] F. Zwicky, "Die Rotverschiebung von extragalaktischen Nebeln", Helv. Phys. Acta **6** (1933) 110–127.

[35] V. C. Rubin and W. K. Ford, Jr., "Rotation of the Andromeda Nebula from a Spectroscopic Survey of Emission Regions", Astrophys. J. **159** (1970) 379–403.

[36] http://en.wikipedia.org/wiki/Galaxy_rotation_curve.

[37] D. Clowe, A. Gonzalez, and M. Markevitch, "Weak-Lensing Mass Reconstruction of the Interacting Cluster 1E 0657558: Direct Evidence for the Existence of Dark Matter", Astrophys. J. **604** (2004) 596.

[38] Planck Collaboration, "Planck 2013 results. XVI. Cosmological parameters", (2014), arXiv:1303.5076. Accepted by Astron. Astrophys.

[39] S. P. Martin, "A Supersymmetry Primer", (1997), arXiv:hep-ph/9709356.

[40] J. Wess and B. Zumino, "Supergauge Transformations in Four-Dimensions", Nucl. Phys. B **70** (1974) 39, doi:10.1016/0550-3213(74)90355-1.

[41] S. Dimopoulos and H. Georgi, "Softly Broken Supersymmetry and SU(5)", Nucl. Phys. B **193** (1981) 150, doi:10.1016/0550-3213(81)90522-8.

[42] H. P. Nilles, "Supersymmetry, Supergravity and Particle Physics", Phys. Rept. **110** (1984) 1, doi:10.1016/0370-1573(84)90008-5.

[43] H. E. Haber and G. L. Kane, "The Search for Supersymmetry: Probing Physics Beyond the Standard Model", Phys. Rept. **117** (1985) 75, doi:10.1016/0370-1573(85)90051-1.

[44] R. Barbieri, S. Ferrara, and C. A. Savoy, "Gauge Models with Spontaneously Broken Local Supersymmetry", Phys. Lett. B **119** (1982) 343, doi:10.1016/0370-2693(82)90685-2.

[45] S. Dawson, E. Eichten, and C. Quigg, "Search for Supersymmetric Particles in Hadron - Hadron Collisions", Phys. Rev. D **31** (1985) 1581, doi:10.1103/PhysRevD.31.1581.

[46] F. Gabbiani et al., "A complete analysis of FCNC and CP constraints in general SUSY extensions of the standard model", Nucl. Phys. B **477** (1996) 321 – 352, doi:10.1016/0550-3213(96)00390-2.

[47] Particle Data Group Collaboration, "Review of Particle Physics", Phys. Rev. D **86** (2012) 010001, doi:10.1103/PhysRevD.86.010001.

[48] M. Chemtob, "Phenomenological constraints on broken R-parity symmetry in supersymmetry models", Prog. Part. Nucl. Phys. **54** (2005) 71–191, doi:10.1016/j.ppnp.2004.06.001, arXiv:hep-ph/0406029.

[49] G. Jungman, M. Kamionkowski, and K. Griest, "Supersymmetric Dark Matter", Phys. Rept. **267** (1996) 195–373, doi:10.1016/0370-1573(95)00058-5, arXiv:hep-ph/9506380.

[50] C. Csaki, Y. Grossman, and B. Heidenreich, "MFV SUSY: A Natural Theory for R-Parity Violation", Phys. Rev. D **85** (2012) 095009, doi:10.1103/PhysRevD.85.095009, arXiv:1111.1239.

[51] N. Sakai, "Naturalness in Supersymmetric GUTS", Z. Phys. C **11** (1981) 153, doi:10.1007/BF01573998.

[52] S. Dimopoulos and G. F. Giudice, "Naturalness constraints in supersymmetric theories with nonuniversal soft terms", Phys. Lett. B **357** (1995) 573–578, doi:10.1016/0370-2693(95)00961-J, arXiv:hep-ph/9507282.

[53] M. Papucci, J. T. Ruderman, and A. Weiler, "Natural SUSY Endures", J. High Energy Phys. **09** (2012) 035, doi:10.1007/JHEP09(2012)035, arXiv:1110.6926.

[54] C. Brust et al., "SUSY, the Third Generation and the LHC", J. High Energy Phys. **03** (2012) 103, doi:10.1007/JHEP03(2012)103, arXiv:1110.6670.

[55] W. Beenakker et al., "Squark and gluino production at hadron colliders", Nucl. Phys. B **492** (1997) 51, doi:10.1016/S0550-3213(97)80027-2, arXiv:hep-ph/9610490.

[56] A. Kulesza and L. Motyka, "Threshold Resummation for Squark-Antisquark and Gluino-Pair Production at the LHC", Phys. Rev. Lett. **102** (2009) 111802, doi:10.1103/PhysRevLett.102.111802, arXiv:0807.2405.

[57] A. Kulesza and L. Motyka, "Soft gluon resummation for the production of gluino-gluino and squark-antisquark pairs at the LHC", Phys. Rev. D **80** (2009) 095004, doi:10.1103/PhysRevD.80.095004, arXiv:0905.4749.

[58] W. Beenakker et al., "Soft-gluon resummation for squark and gluino hadroproduction", J. High Energy Phys. **12** (2009) 041, doi:10.1088/1126-6708/2009/12/041, arXiv:0909.4418.

[59] W. Beenakker et al., "Squark and gluino hadroproduction", Int. J. Mod. Phys. A **26** (2011) 2637, doi:10.1142/S0217751X11053560, arXiv:1105.1110.

[60] N. Arkani-Hamed et al., "MARMOSET: The Path from LHC Data to the New Standard Model via On-Shell Effective Theories", (2007), arXiv:hep-ph/0703088.

[61] J. Alwall, P. C. Schuster, and N. Toro, "Simplified models for a first characterization of new physics at the LHC", Phys. Rev. D **79** (2009) 075020, doi:10.1103/PhysRevD.79.075020.

[62] LHC New Physics Working Group, "Simplified models for LHC new physics searches", J. Phys. G **39** (2012) 105005, doi:10.1088/0954-3899/39/10/105005.

[63] CMS Collaboration, "Interpretation of Searches for Supersymmetry with Simplified Models", Phys. Rev. D **88** (2013) 052017, doi:10.1103/PhysRevD.88.052017, arXiv:1301.2175.

[64] L. Evans and P. Bryant, "LHC Machine", JINST **3** (2008) S08001, doi:10.1088/1748-0221/3/08/S08001.

[65] http://ps-div.web.cern.ch/ps-div/PSComplex/accelerators.pdf.

[66] CMS Collaboration, "The CMS experiment at the CERN LHC", JINST **3** (2008) S08004, doi:10.1088/1748-0221/3/08/S08004.

[67] https://cms-docdb.cern.ch/cgi-bin/PublicDocDB/ShowDocument?docid=5581.

[68] J. Anderson et al., "Upgrade of the CMS Hadron Outer Calorimeter with SIPMs", Physics Procedia **37** (2012) 72–78, doi:10.1016/j.phpro.2012.02.358. Proceedings of the 2nd International Conference on Technology and Instrumentation in Particle Physics (TIPP 2011).

[69] Benjamin Lutz (for the CMS collaboration), "Upgrade of the CMS Hadron Outer Calorimeter with SiPM sensors", J. Phys. Conf. Ser. **404** (2012) 012018, doi:10.1088/1742-6596/404/1/012018.

[70] CMS Collaboration, "CMS reconstruction improvement for the muon tracking by the RPC chambers", JINST **8** (2013) T03001, doi:10.1088/1748-0221/8/03/T03001, arXiv:1209.2646.

[71] CMS Collaboration, "Photon Reconstruction and Identification at $\sqrt{s} =$ 7 TeV", CMS Physics Analysis Summary CMS-PAS-EGM-10-005, (2010).

[72] CMS Collaboration, "Performance of τ-lepton reconstruction and identification in CMS", JINST **7** (2012) P01001, doi:10.1088/1748-0221/7/01/P01001.

[73] CMS Collaboration, "CMS Tracking Performance Results from early LHC Operation", Eur. Phys. J. C **70** (2010) 1165–1192, doi:10.1140/epjc/s10052-010-1491-3, arXiv:1007.1988.

[74] CMS Collaboration, "Track reconstruction, primary vertex finding and seed generation with the Pixel Detector", CMS Note CMS-NOTE-2006-026, (2006).

[75] CMS Collaboration, "Track Reconstruction in the CMS Tracker", CMS Note CMS-NOTE-2006-041, (2006).

[76] CMS Collaboration, "Adaptive Vertex Fitting", CMS Note CMS-NOTE-2007-008, (2007).

[77] M. Cacciari, G. P. Salam, and G. Soyez, "The anti-k_t jet clustering algorithm", J. High Energy Phys. **04** (2008) 063, doi:10.1088/1126-6708/2008/04/063.

[78] CMS Collaboration, "Particle-Flow Event Reconstruction in CMS and Performance for Jets, Taus, and $\not\!\!E_{\mathrm{T}}$", CMS Physics Analysis Summary CMS-PAS-PFT-09-001, (2009).

[79] CMS Collaboration, "Commissioning of the Particle-Flow Reconstruction in Minimum-Bias and Jet Events from *pp* Collisions at 7 TeV", CMS Physics Analysis Summary CMS-PAS-PFT-10-002, (2010).

[80] CMS Collaboration, "Determination of jet energy calibration and transverse momentum resolution in CMS", JINST **6** (2011) P11002, doi:10.1088/1748-0221/6/11/P11002, arXiv:1107.4277.

[81] M. Cacciari and G. P. Salam, "Pileup subtraction using jet areas", Phys. Lett. B **659** (2008) 119 – 126, doi:10.1016/j.physletb.2007.09.077.

[82] https://twiki.cern.ch/twiki/bin/view/CMSPublic/PhysicsResultsJME2012JEC.

[83] CMS Collaboration, "Identification of b-quark jets with the CMS experiment", JINST **8** (2013) P04013, doi:10.1088/1748-0221/8/04/P04013, arXiv:1211.4462.

[84] CMS Collaboration, "Missing transverse energy performance of the CMS detector", JINST **6** (2011) P09001, doi:10.1088/1748-0221/6/09/P09001.

[85] CMS Collaboration, "Performance of Missing Transverse Momentum Reconstruction Algorithms in Proton-Proton Collisions at $\sqrt{s} = 8$ TeV with the CMS Detector", CMS Physics Analysis Summary CMS-PAS-JME-12-002, (2013).

[86] S. Baffioni et al., "Electron reconstruction in CMS", Eur. Phys. J. C **49** (2007) 1099–1116, doi:10.1140/epjc/s10052-006-0175-5.

[87] W. Adam et al., "Reconstruction of electrons with the Gaussian-sum filter in the CMS tracker at the LHC", J. Phys. G **31** (2005) N9–N20, doi:10.1088/0954-3899/31/9/N01, arXiv:physics/0306087.

[88] CMS Collaboration, "Commissioning of the Particle-Flow Event Reconstruction with the first LHC collisions recorded in the CMS detector", CMS Physics Analysis Summary CMS-PAS-PFT-10-001, (2010).

[89] CMS Collaboration, "Isolated Photon Reconstruction and Identification at $\sqrt{s} = 7$ TeV", CMS Physics Analysis Summary CMS-PAS-EGM-10-006, (2010).

[90] CMS Collaboration, "Measurement of the Inclusive W and Z Production Cross Sections in *pp* Collisions at $\sqrt{s} = 7$ TeV", J. High Energy Phys. **10** (2011) 132, doi:10.1007/JHEP10(2011)132, arXiv:1107.4789.

[91] CMS Collaboration, "Performance of CMS muon reconstruction in pp collision events at $\sqrt{s} = 7$ TeV", JINST **7** (2012) P10002, doi:10.1088/1748-0221/7/10/P10002, arXiv:1206.4071.

[92] CMS Collaboration, "Particle-flow commissioning with muons and electrons from J/ψ and W events at 7 TeV", CMS Physics Analysis Summary CMS-PAS-PFT-10-003, (2010).

[93] J. Alwall et al., "MadGraph 5: going beyond", J. High Energy Phys. **06** (2011) 128, doi:10.1007/JHEP06(2011)128, arXiv:1106.0522.

[94] S. Frixione, P. Nason, and C. Oleari, "Matching NLO QCD computations with parton shower simulations: the POWHEG method", J. High Energy Phys. **11** (2007) 070, doi:10.1088/1126-6708/2007/11/070, arXiv:0709.2092.

[95] Z. Was, "TAUOLA the library for tau lepton decay", Nucl. Phys. Proc. Suppl. **98** (2001) 96, doi:10.1016/S0920-5632(01)01200-2, arXiv:hep-ph/0011305.

[96] T. Sjöstrand, S. Mrenna, and P. Z. Skands, "PYTHIA 6.4 physics and manual", J. High Energy Phys. **05** (2006) 026, doi:10.1088/1126-6708/2006/05/026, arXiv:hep-ph/0603175.

[97] J. Pumplin et al., "New generation of parton distributions with uncertainties from global QCD analysis", J. High Energy Phys. **07** (2002) 012, doi:10.1088/1126-6708/2002/07/012, arXiv:hep-ph/0201195.

[98] P. M. Nadolsky et al., "Implications of CTEQ global analysis for collider observables", Phys. Rev. D **78** (2008) 013004, doi:10.1103/PhysRevD.78.013004, arXiv:0802.0007.

[99] H.-L. Lai et al., "New parton distributions for collider physics", Phys. Rev. D **82** (2010) 074024, doi:10.1103/PhysRevD.82.074024, arXiv:1007.2241.

[100] GEANT4 Collaboration, "GEANT4—a simulation toolkit", Nucl. Instrum. Methods A **506** (2003) 250, doi:10.1016/S0168-9002(03)01368-8.

[101] CMS Collaboration, "Measurement of the Underlying Event Activity at the LHC with $\sqrt{s} = 7$ TeV and Comparison with $\sqrt{s} = 0.9$ TeV", J. High Energy Phys. **09** (2011) 109, doi:10.1007/JHEP09(2011)109, arXiv:1107.0330.

[102] J. M. Campbell and R. K. Ellis, "MCFM for the Tevatron and the LHC", Nucl. Phys. Proc. Suppl. **205-206** (2010) 10–15, doi:10.1016/j.nuclphysbps.2010.08.011, arXiv:1007.3492.

[103] R. Gavin et al., "FEWZ 2.0: A code for hadronic Z production at next-to-next-to-leading order", Comput. Phys. Commun. **182** (2011) 2388–2403, doi:10.1016/j.cpc.2011.06.008, arXiv:1011.3540.

[104] N. Kidonakis, "Differential and total cross sections for top pair and single top production", (2012), doi:10.3204/DESY-PROC-2012-02/251, arXiv:1205.3453.

[105] CMS Collaboration, "The fast simulation of the CMS detector at LHC", J. Phys. Conf. Ser. **331** (2011) 032049, doi:10.1088/1742-6596/331/3/032049.

[106] R. K. Ellis, W. J. Stirling, and B. R. Webber, *QCD and Collider Physics*. Cambridge University Press, Cambridge, 1996.

[107] A. Czarnecki, J. Korner, and J. Piclum, "Helicity fractions of W bosons from top quark decays at NNLO in QCD", Phys. Rev. D **81** (2010) 111503(R), doi:10.1103/PhysRevD.81.111503, arXiv:1005.2625.

[108] CMS Collaboration, "Measurements of $t\bar{t}$ spin correlations and top-quark polarization using dilepton final states in pp collisions at $\sqrt{s} = 7$ TeV", Phys. Rev. Lett. **112** (2014) 182001, doi:10.1103/PhysRevLett.112.182001, arXiv:1311.3924.

[109] ATLAS Collaboration, "Measurement of top quark polarization in top-antitop events from proton-proton collisions at $\sqrt{s} = 7$ TeV using the ATLAS detector", Phys. Rev. Lett. **111** (2013) 232002, doi:10.1103/PhysRevLett.111.232002, arXiv:1307.6511.

[110] W. Bernreuther, M. Fücker, and Z.-G. Si, "Weak interaction corrections to hadronic top quark pair production", Phys. Rev. D **74** (2006) 113005, doi:10.1103/PhysRevD.74.113005.

[111] D0 Collaboration, "Measurement of the W boson helicity in top quark decays using 5.4 fb^{-1} of $p\bar{p}$ collision data", Phys. Rev. D **83** (2011) 032009, doi:10.1103/PhysRevD.83.032009, arXiv:1011.6549.

[112] CDF Collaboration, "Measurement of W Boson Polarization in Top-quark Decay using the Full CDF Run II Data Set", Phys. Rev. D **87** (2013) 031104, doi:10.1103/PhysRevD.87.031104, arXiv:1211.4523.

[113] ATLAS Collaboration, "Measurement of the W boson polarization in top quark decays with the ATLAS detector", J. High Energy Phys. **06** (2012) 088, doi:10.1007/JHEP06(2012)088, arXiv:1205.2484.

[114] CMS Collaboration, "Measurement of the W boson helicity in top-quark decays from $t\bar{t}$ production in lepton+jets events in pp collisions at $\sqrt{s} =$ 7 TeV", J. High Energy Phys. **10** (2013) 167, doi:10.1007/JHEP10(2013)167, arXiv:1308.3879.

[115] CMS Collaboration, "Measurement of the W boson helicity in top decays from $t\bar{t}$ production in lepton+jets events at the LHC at $\sqrt{s} = 8$ TeV", CMS Physics Analysis Summary CMS-PAS-TOP-13-008, (2013).

[116] Z. Bern et al., "Left-Handed W Bosons at the LHC", Phys. Rev. D **84** (2011) 034008, doi:10.1103/PhysRevD.84.034008, arXiv:1103.5445.

[117] CMS Collaboration, "Measurement of the Polarization of W Bosons with Large Transverse Momenta in W + jets Events at the LHC", Phys. Rev. Lett. **107** (2011) 021802, doi:10.1103/PhysRevLett.107.021802.

[118] ATLAS Collaboration, "Measurement of the polarisation of W bosons produced with large transverse momentum in pp collisions at $\sqrt{s} = 7$ TeV with the ATLAS experiment", Eur. Phys. J. C **72** (2012) 2001, doi:10.1140/epjc/s10052-012-2001-6, arXiv:1203.2165.

[119] CMS Collaboration, "Measurement of the lepton charge asymmetry in inclusive W production in pp collisions at $\sqrt{s} = 7$ TeV", J. High Energy Phys. **04** (2011) 050, doi:10.1007/JHEP04(2011)050, arXiv:1103.3470.

[120] T. Danielson et al., "Reconstruction, identification, and trigger efficiencies for SUSY searches in the single lepton channel in 2012", CMS Analysis Note CMS-AN-13-035, (2013).

[121] T. N. Kypreos and I. K. Furic, "Measurement of the High p_T Momentum Scale with the Endpoint Method", CMS AN 11-479 (2011).

[122] B. Efron, *The Jackknife, the Bootstrap and Other Resampling Plans*. Society for Industrial and Applied Mathematics, 1982.

[123] https://twiki.cern.ch/twiki/bin/view/CMSPublic/PhysicsResultsSUS13007.

[124] CMS Collaboration, "CMS Luminosity Based on Pixel Cluster Counting - Summer 2013 Update", CMS Physics Analysis Summary CMS-PAS-LUM-13-001, (2013).

[125] M. Botje et al., "The PDF4LHC Working Group Interim Recommendations", (2011), arXiv:1101.0538.

[126] A. D. Martin et al., "Parton distributions for the LHC", Eur. Phys. J. C **63** (2009) 189–285, doi:10.1140/epjc/s10052-009-1072-5, arXiv:0901.0002.

[127] R. D. Ball et al., "A first unbiased global NLO determination of parton distributions and their uncertainties", Nucl. Phys. B **838** (2010) 136–206, doi:10.1016/j.nuclphysb.2010.05.008, arXiv:1002.4407.

[128] D. Bourilkov, R. C. Group, and M. R. Whalley, "LHAPDF: PDF use from the Tevatron to the LHC", (2006), arXiv:hep-ph/0605240.

[129] T. Junk, "Confidence level computation for combining searches with small statistics", Nucl. Instrum. Methods A **434** (1999) 435, doi:10.1016/S0168-9002(99)00498-2, arXiv:hep-ex/9902006.

[130] A. L. Read, "Presentation of search results: the CL_S technique", J. Phys. G **28** (2002) 2693, doi:10.1088/0954-3899/28/10/313.

[131] ATLAS and CMS Collaborations, LHC Higgs Combination Group, "Procedure for the LHC Higgs boson search combination in Summer 2011", Technical Report ATL-PHYS-PUB/2011-11, CMS NOTE 2011/005, (2011).

[132] M. Krämer et al., "Supersymmetry production cross sections in pp collisions at $\sqrt{s} = 7$ TeV", (2012), arXiv:1206.2892.

[133] CMS Collaboration, "Search for supersymmetry using razor variables in events with b-jets in pp collisions at 8 TeV", CMS Physics Analysis Summary CMS-PAS-SUS-13-004, (2013).

[134] ATLAS Collaboration, "Search for direct top squark pair production in final states with one isolated lepton, jets, and missing transverse momentum in $\sqrt{s} = 8$ TeV pp collisions using 21 fb^{-1} of ATLAS data", ATLAS Conference Note ATLAS-CONF-2013-037, (2013).

[135] ATLAS Collaboration, "Search for direct production of the top squark in the all-hadronic $t\bar{t} + \not{E}_{\mathrm{T}}$ final state in 21 fb^{-1} of pp collisions at $\sqrt{s} = 8$ TeV

with the ATLAS detector", ATLAS Conference Note ATLAS-CONF-2013-024, (2013).